NATIONAL TECHNICAL UNIVERSITY OF ATHENS
SCHOOL OF NAVAL ARCHITECTURE & MARINE ENGINEERING
DIVISION OF MARINE ENGINEERING

DIPLOMA THESIS

Michail Chalkiopoulos

Computational and Experimental Evaluation of Performance of Thrust Bearings operating under TEHD regime

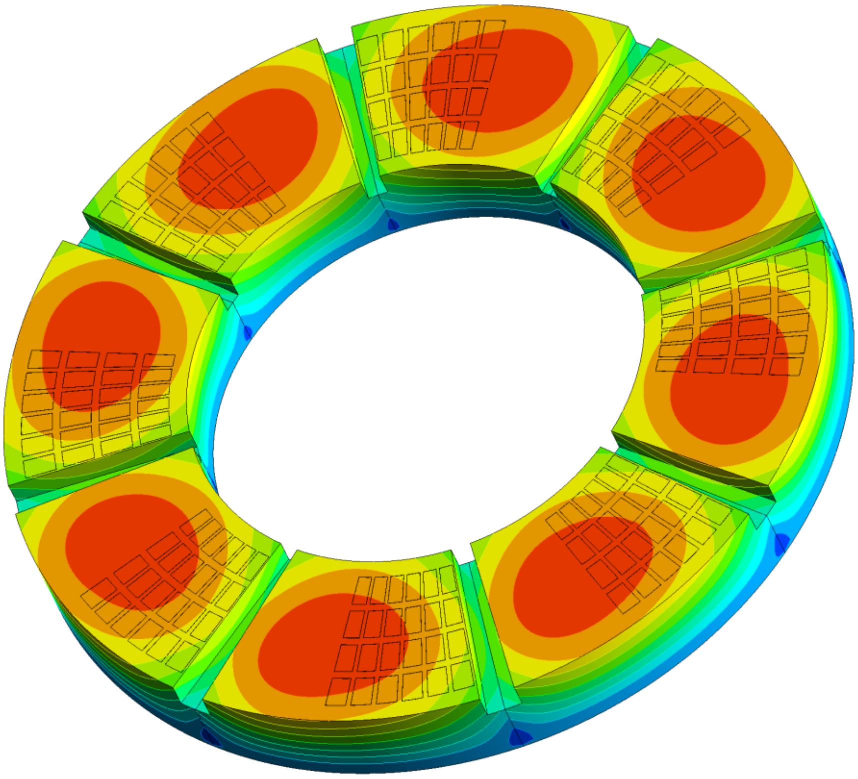

Examination Committee

SUPERVISOR:	C.I. Papadopoulos, Associate Professor NTUA
MEMBERS:	L. Kaiktsis, Professor NTUA
	G. Papalambrou, Assistant Professor NTUA

Acknowledgments

To begin with I would like to thank my supervisor Associate Professor Christos Papadopoulos both for his support and cooperation throughout my years in NTUA and for trusting me with the operation and maintenance of the Tribology Unit of the Marine Engineering Lab. I would also like to thank Professor Lambros Kaiktsis for his advices and suggestions on our research. Special thanks to Anastassios Charitopoulos and George Rossopoulos for their help and guidance through the preparation of the current thesis. I would also like to thank the division of marine engineering of NTUA and professor Michel Fillon for giving me the opportunity to present a part of this study to the 46th Leeds-Lyon Symposium on Tribology.

Last but not least, I would like to thank my family for supporting me throughout my years in university. The present thesis is dedicated to my beloved grandfathers and my physics teacher Nikitas Hadjiconstantinou.

“[To] mechanical progress there is apparently no end: for as in the past so in the future, each step in any direction will remove limits and bring in past barriers which have till then blocked the way in other directions; and so what for the time may appear to be a visible practical limit will turn out to be but a bend in the road”

-Osborne Reynolds-

Table of Contents

List of Figures

List of Tables

Abstract

In the present thesis, a computation fluid dynamics study on hydrodynamic lubricated thrust bearings is presented. Two performance optimisation problems have been set up and solved, aiming at evaluating the optimal texture geometry parameters of a sector pad thrust bearing with surface texturing, one with circumferential grooves and one with rectangular dimples, in order to maximise the load carrying capacity and minimise the friction torque. The optimisation problems have been setup and solved using a multi-objective optimisation procedure based on genetic algorithms (GA). Bearing response calculations have been performed with a thermo-hydrodynamic (THD) modelling approach. The resulting optimal geometrical configuration of the rectangular dimples has been evaluated with the utilisation of a thermo-elasto-hydrodynamic (TEHD) model, in order to quantify the effects of thermal and mechanical deformations on the tribological characteristics of the textured bearing. After the TEHD evaluation, an optimal design has been selected, and a sensitivity analysis has been performed, varying the independent geometric parameters around the optimal values, in order to identify their proximity to the global optimum. Furthermore, a tapered land and a textured open pocket bearing were evaluated with the more advanced TEHD modelling method, highlighting the importance of modelling the thermal and mechanical deformation during the design of thrust bearings, operating from medium to high temperatures. Finally, an experimental set up for the calculation of the tribological properties of thrust bearings is demonstrated, along with the manufacturing process of a parallel and an open pocket bearing.

Περίληψη

Η παρούσα διπλωματική εργασία πραγματεύεται την μελέτη συμπεριφοράς ωστικών εδράνων ολίσθησης με τη μέθοδο της υπολογιστικής ρευστομηχανικής. Δύο προβλήματα βελτιστοποίησης τέθηκαν και επιλύθηκαν, με στόχο την βελτιστοποίηση των γεωμετρικών παραμέτρων τεχνητής τραχύτητας στην επιφάνεια του εδράνου, ένα με περιφερειακές αυλακώσεις και ένα με τετράγωνες κοιλότητες, με στόχο την μεγιστοποίηση ικανότητας παραλαβής φορτίου και την ελαχιστοποίηση της ροπής τριβής. Τα παραπάνω προβλήματα επιλύθηκαν με χρήση πολύ-κριτηριακής βελτιστοποίησης βασισμένη στους γενετικούς αλγόριθμους. Οι υπολογισμοί απόκρισης του εδράνου πραγματοποιήθηκαν με χρήση θερμό-υδροδυναμικού μοντέλου. Η τελική βέλτιστη γεωμετρία με τετράγωνες κοιλότητες, αξιολογήθηκε με χρήση θέρμο-έλαστο-υδροδυναμικού μοντέλου, με στόχο την ποσοτικοποίηση της επίδρασης των θερμικών και μηχανικών παραμορφώσεων στα τριβολογικά χαρακτηρίστηκα του εδράνου με τεχνητή τραχύτητα. Μετά την αξιολόγηση του θέρμο-έλαστο-υδροδυναμικού μοντέλου, μία βέλτιστή γεωμετρία επιλέχθηκε, για ανάλυση ευαισθησίας των γεωμετρικών παραμέτρων κοντά στις βέλτιστες, προκειμένου να επιβεβαιωθεί η εγγύτητά τους προς το ολικό βέλτιστο. Επιπρόσθετα, ένα έδρανο με επιφάνεια κεκλιμένη στην περιοχή της αναρρόφησης του λιπαντικού ελαίου, και παράλληλη στην περιοχή της κατάθλιψης του λιπαντικού ελαίου (επικλινή έδρανο) και ένα έδρανο με ανοικτή κοιλότητα στην επιφάνεια αξιολογήθηκαν με το πιο σύνθετο θέρμο-έλαστο-υδροδυναμικό μοντέλο, υποδεικνύοντας την σημαντικότητα της μοντελοποίησης των θερμικών και μηχανικών παραμορφώσεων, κατά τη διάρκεια σχεδίασης ωστικών εδράνων, που λειτουργούν από μεσαίες έως υψηλές θερμοκρασίες. Τέλος, παρουσιάζεται μία πειραματική διάταξη, που στοχεύει στον υπολογισμό των τριβολογικών ιδιοτήτων ωστικών εδράνων ολίσθησης, καθώς και η διαδικασία κατασκευής ενός παράλληλου εδράνου και ενός με ανοικτή επιφανειακή κοιλότητα.

1 Introduction

1.1 Literature Review

Hydrodynamic lubrication theory goes back at the end of the 19th century, when Beauchamp Tower performed certain experiments on journal bearings in order to measure the pressure of the oil inside the bearing. During the operation of the bearing, Tower observed a leakage of oil from a hole at the bottom, that was originally designed to supply oil in the bearing, for lubrication. He then placed a wooden bung inside the hole, to restrict the oil leakage. However, the bung was pushed out, due to the oil pressure. Tower then realised that the fluid inside the journal bearing was pressurised and had the ability to separate the two sliding surfaces. At the same time Osborne Reynolds and other scientists, were developing the theory of lubrication. Tower's experiments provided experimental data to Reynolds and enabled him to validate his theory. In 1886, the Theory of Lubrication was published, in the proceedings of the Royal Society [1].

Since then many studies and experiments have been performed, aiming to explain and assess the tribological characteristics and performance of hydrodynamic lubricated thrust bearing. In 1946, Fogg performed certain experiments on parallel surface bearings, and proved that although in theory they cannot develop hydrodynamic pressure, in practice they were able to sustain sufficient amounts of thrust load, compared to tilting pads [2]. Fogg suggested that this occurs due to thermal expansion of the fluid film, which leads to a distortion of the velocity distribution curves, similar to those produced by converging surfaces. In 1958, Cameron and Wood presented a general form of the theory for parallel bearings [3]. In 1965, Currie demonstrated the effects of thermal wedge lubrication of parallel surface thrust bearings, while developing a computational method of solving the governing equations [4].

In 1967, Tzeng and Saibel studied the effect of roughness of surfaces of slider bearings on load carrying capacity and friction force. They concluded that load carrying capacity and friction force are increased when surface roughness is considered [5]. In 1987, Tonder concluded that surface texturing, in the surface machining or finishing process, with an orientation suitable for the general geometry of the bearing could be beneficial for the performance of the bearing [6]. Over the past recent years, extensive research has been performed, aiming to evaluate the beneficial effects of surface texturing, on the performance of hydrodynamic lubricated bearings. Reynolds equation can be solved for simple geometries with isothermal fluid flow conditions [7]. In studies [8]-[13], artificial surface texturing has been addressed in the form of rectangular patterns in order to optimise the performance of sector pad bearings. Computational Fluid Dynamics with Thermohydrodynamic models are able to solve the governing equations of hydrodynamic lubrication by taking into consideration heat exchange effects on complex geometries, viscous dissipation of the fluid, and temperature dependent viscosity and density.

In [14] different surface geometries of a sector pad are analyzed based on the numerical solution of Navier-Stokes and energy equations for incompressible flow. The results concluded to the superiority of an open pocket design. Zouzoulas and Papadopoulos, studied the effects of hydrophobicity on the performance of bearings in [15], and concluded that hydrophobicity can significantly enhance their tribological performance. In [16] the effects on mechanical deformation of the bearing mechanical parts are calculated, by Charitopoulos et al. A one-way FSI model is introduced where an FE solver receives data from a THD analysis and calculates the thermal and mechanical deformations of the bearing components. For thrust bearings that operate with high specific loads, [17] has shown that 20% of the oil heat generated from friction is transferred through the solids, while 80% is removed by the oil, thus the effects of solid deformation might be significant on the performance of the bearing. Such effects were investigated in [18] by Ahmed et al. with a TEHD study, which takes into consideration the mechanical and thermal deformation during the operation of the runner and pad. The latter is crucial for evaluating the performance of the bearing. In [19], another TEHD analysis indicates, that the performance of the bearing is affected mainly by the thermal deformation of the pad compared to the mechanical.

1.2 Hydrodynamic Lubrication

Friction plays a vital role in all aspects of the everyday life. Most of the manufactured mechanisms involve solids that move relatively to one another. In these cases, friction is the main cause of wear, which leads to not only material wastage and mechanical loss of performance, but also to extreme dissipation of energy. The main source of friction are the imperfections of the surfaces. Lubrication is the most common way in order to reduce friction. Hydrodynamic lubrication involves the generation of a thick film of liquid between two surfaces that move relatively to each other with a sufficient velocity, by hydrodynamic pressure. The pressure build-up mechanism can withstand a certain load, improve friction and prevent damage. In general, the thickness of these films varies from 1 to 100 μm, thus they are very difficult to be observed [28]. The performance of the lubricant depends on many parameters, such as its chemical characteristics and composition. Some of these parameters will be discussed below.

1.2.1 Oil Viscosity

The oil viscosity plays a fundamental role in the performance of the lubricant. Viscosity differs among the different oils, and is highly depended on temperature, shear rate and pressure. The generated film is often proportional to it. However thicker oils require more energy to be sheared, thus they generate more heat and lead to higher working temperatures on the surfaces and may damage the components. In every application the proper oil should be chosen in order to give optimum performance at certain working temperatures.

1.2.2 Dynamic Viscosity

Consider two flat surfaces sliding relatively to one another. The upper surface moves with velocity **u**$\left[\frac{m}{s}\right]$ and the lower surface is stationary. The film thickness is **h[m]**. The force **F [N]** required to move the surface is proportional to the wetted area **A** $[m^2]$ and the velocity gradient **u/h** as shown in **Figure 1**.

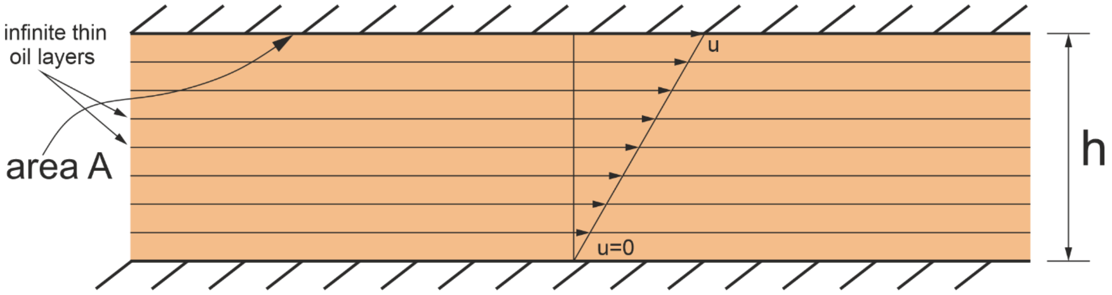

Figure 1 - Velocity gradient

In this case F can be written as:

$$F = \eta \times A \times \frac{u}{h} \tag{1}$$

Where ***η [Pas]*** is the dynamic viscosity. Different fluids exhibit different values of dynamic viscosity. Rearranging:

$$\eta = \frac{F}{A} \times \frac{h}{u} \tag{2}$$

Or

$$\eta = \tau \times \frac{h}{u} \qquad [3]$$

Where, **τ [Pa]** is the shear stress acting on the fluid.

Another major characteristic is the kinematic viscosity of the fluid. It is defined as the ratio of dynamic viscosity to the fluid density.

$$v = \frac{\eta}{\rho} \qquad [4]$$

Where $\boldsymbol{v}$ $[\frac{\boldsymbol{m^2}}{\boldsymbol{s}}]$ is the kinematic viscosity, **η** $[\boldsymbol{Pas}]$ is the dynamic viscosity and **ρ**$[\frac{\boldsymbol{kg}}{\boldsymbol{m^3}}]$ is the fluid density.

1.2.3 Pressure Build-up Mechanism

Hydrodynamic Lubrication can be expressed mathematically with the use of the Navier-Stokes momentum and continuity equations. For an oil film to be generated between two surfaces and therefore for hydrodynamic lubrication to occur there are two main conditions that should be applied [28].

- There must be a relative motion between the two surfaces with a sufficient velocity for a load-carrying film to be generated.
- The two surfaces must be inclined at some angle to each other. Parallel surfaces according to theory cannot form a lubricating film that supports load.

In the upper allegation there are some exceptions. In the recent literature it has been proposed that parallel surfaces with surface texturing can generate hydrodynamic pressure and withstand a sufficient load capacity. Moreover, experimental results show that parallel surfaces can actually generate hydrodynamic pressure. The mechanism that allows a parallel bearing to generate a lubricating film will be discussed below.

In **Figure 2** the principle of the pressure build-up mechanism between two non parallel surfaces is presented. The upper surface often referred as 'stator' is inclined to a certain angle. The bottom solid often referred as 'runner' or 'rotor' moves with a certain velocity **U**, dragging lubricant along into the converging wedge. According to the momentum and continuity equations equal volume of fluid should enter and leave the surfaces. This leads to a generation of pressure field between the two surfaces. At the leading edge the pressure is increased in order to restrict the entry flow, while on the trailing edge the pressure is decreased in order to boost the exit flow. The pressure gradient bends the fluid velocity inwards at the entrance to the wedge and outwards at the exit. The generated pressure separates the two surfaces and is capable of supporting a certain load.

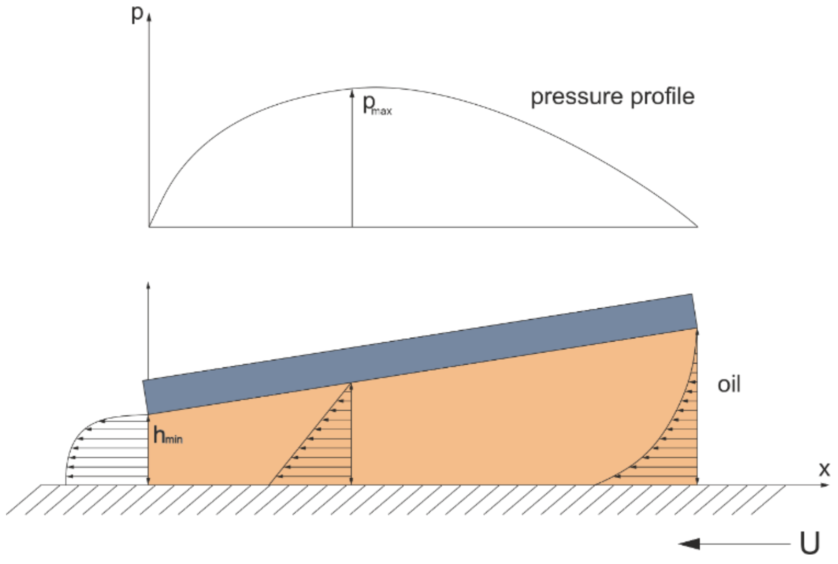

Figure 2 - Pressure build-up mechanism between two inclined surfaces

1.3 Mathematical Approach

1.3.1 Momentum Equations

The general form of the Navier-Stokes equation can be obtained by applying the Newton's Second law, the conservation of momentum, on a arbitrary portion of the fluid.

$$\frac{\partial \rho \boldsymbol{V}}{\partial t} + \nabla \cdot (\rho \boldsymbol{V} \times \boldsymbol{V}) = -\nabla p + \nabla \tau + S \qquad [5]$$

Where:

$\boldsymbol{V} = velocity\ vector\ [\frac{m}{s}]$

$\rho = fluid\ Density\ [\frac{kg}{m^3}]$

$p = pressure\ [Pa]$

$\tau = total\ stress\ tensor\ [Pa]$

$S = represented\ body\ forces\ acting\ on\ fluid\ \ [\frac{N}{m^3}]$

The represented body forces (S) usually consist only of gravity. Gravity is always present but in many cases, it can be neglected. This is assumption is applied on hydrodynamic lubrication, and therefore fluid motion is the result of shear and pressure fields arising from the motion imposed.

For incompressible Newtonian fluid flows, the Eq. 5 can be re-arranged in the following.

$$\rho(\frac{\partial \boldsymbol{V}}{\partial t} + \boldsymbol{V} \cdot \nabla \boldsymbol{V}) = -\nabla p + \nabla \tau \qquad [6]$$

Three spatial equations can be obtained by splitting Eq. 6.

Velocity Vector $\boldsymbol{V} = (u, v, w)$

X direction:

$$\rho\left(\frac{\partial u}{\partial t} + u\frac{\partial u}{\partial x} + v\frac{\partial u}{\partial y} + z\frac{\partial u}{\partial z}\right) = -\frac{\partial p}{\partial x} + 2\frac{\partial}{\partial x}\left(\mu\frac{\partial u}{\partial x}\right) + \frac{\partial}{\partial y}\left[\mu\left(\frac{\partial u}{\partial y} + \frac{\partial v}{\partial x}\right)\right] + \frac{\partial}{\partial z}\left[\mu\left(\frac{\partial u}{\partial z} + \frac{\partial w}{\partial x}\right)\right] - \frac{2}{3}\frac{\partial}{\partial x}(\mu\nabla\boldsymbol{V}) \qquad [7]$$

Y direction:

$$\rho\left(\frac{\partial v}{\partial t} + u\frac{\partial v}{\partial x} + v\frac{\partial v}{\partial y} + z\frac{\partial v}{\partial z}\right) = -\frac{\partial p}{\partial y} + \frac{\partial}{\partial x}\left[\mu\left(\frac{\partial u}{\partial y} + \frac{\partial v}{\partial x}\right)\right] + 2\frac{\partial}{\partial y}\left(\mu\frac{\partial v}{\partial y}\right) + \frac{\partial}{\partial z}\left[\mu\left(\frac{\partial v}{\partial z} + \frac{\partial w}{\partial y}\right)\right] - \frac{2}{3}\frac{\partial}{\partial y}(\mu\nabla\boldsymbol{V}) \qquad [8]$$

Z direction:

$$\rho\left(\frac{\partial w}{\partial t} + u\frac{\partial w}{\partial x} + v\frac{\partial w}{\partial y} + z\frac{\partial w}{\partial z}\right) = -\frac{\partial p}{\partial z} + \frac{\partial}{\partial x}\left[\mu\left(\frac{\partial u}{\partial z} + \frac{\partial w}{\partial x}\right)\right] + \frac{\partial}{\partial y}\left[\mu\left(\frac{\partial v}{\partial z} + \frac{\partial w}{\partial y}\right)\right] + 2\frac{\partial}{\partial z}\left(\mu\frac{\partial w}{\partial z}\right) - \frac{2}{3}\frac{\partial}{\partial z}(\mu\nabla\boldsymbol{V}) \qquad [9]$$

Continuity Equation

Regardless of the flow assumptions, a statement of the conservation of mass is also necessary. For fluid domains, this is achieved through the continuity equation, given in its most general form as:

$$\frac{\partial\rho}{\partial t}+\nabla(\rho\boldsymbol{V})\equiv\frac{\partial\rho}{\partial t}+\frac{\partial(\rho u)}{\partial x}+\frac{\partial(\rho v)}{\partial y}+\frac{\partial(\rho w)}{\partial z}=0 \qquad \textit{[10]}$$

In the case of incompressible flow, density can be considered constant, and the mass continuity equation can be simplified to the following, often referred as the volume continuity equation:

$$\frac{\partial u}{\partial x}+\frac{\partial v}{\partial y}+\frac{\partial w}{\partial z}=0 \qquad \textit{[11]}$$

1.3.2 Energy Equation

Conservation of energy applied to a differential control volume in a moving fluid under steady conditions, means that the net rate at which energy enters a control volume, plus the rate at which heat is added, minus the rate at which work is done by the fluid, is equal to zero. After manipulation, the result can be rewritten as a thermal energy equation.

$$\rho c_{pf}\left(u\frac{\partial T}{\partial x}+v\frac{\partial T}{\partial y}+w\frac{\partial T}{\partial z}\right)=\lambda_f\left(\frac{\partial^2 T}{\partial x^2}+\frac{\partial^2 T}{\partial y^2}+\frac{\partial^2 T}{\partial z^2}\right)-\mu\Phi+q \qquad \textit{[12]}$$

Where,

$\lambda_f = thermal\ conductivity\ of\ the\ fluid$

$c_{pf} = specific\ heat\ cpacity\ of\ the\ fluid.$

$q = 0\ heat\ generation$

$\Phi = viscous\ dissipation$

The terms on the left side of the equation account for the net rate at which thermal energy leaves the control volume due to bulk fluid motion, while the terms on the right-side account for net inflow of energy due to, viscous dissipation, conduction, and heat generation.

$$\Phi=2\left[\left(\frac{\partial u}{\partial x}\right)^2+\left(\frac{\partial u}{\partial y}\right)^2+\left(\frac{\partial u}{\partial z}\right)^2\right]+\left(\frac{\partial u}{\partial y}+\frac{\partial v}{\partial x}\right)^2+\left(\frac{\partial v}{\partial z}+\frac{\partial w}{\partial y}\right)^2+\left(\frac{\partial w}{\partial x}+\frac{\partial u}{\partial z}\right)^2 \qquad \textit{[13]}$$

Viscous dissipation represents the rate at which mechanical energy is converted to thermal energy due to the shear stresses into the fluid domain. The heat generation term, q, calculates conversion from other forms of energy (chemical, electrical, electromagnetic etc.) to thermal energy.

1.3.3 Heat Transfer Equations

Heat is transferred by means of conduction or convection. Heat conduction occurs on all structural components of the thrust bearing, while in the fluid-pad and fluid-rotor interfaces, intensive flow results in convection.

Heat conduction can be calculated according to Fourier's law, where the three-dimensional field of heat can be expressed as:

$$q'' = -\lambda_s \nabla \boldsymbol{T} \equiv -\lambda_s \left(\frac{\partial T}{\partial x} + \frac{\partial T}{\partial y} + \frac{\partial T}{\partial z} \right) \qquad [14]$$

Where:

$\boldsymbol{q}'' = heat\ flux$

$\lambda_s = solid\ thermal\ conductivity$

Convectional heat transfer can be calculated according to the following equation:

$$q'' = a(T_{wall} - T_{bulk}) \qquad [15]$$

Where:

$a = convection\ coefficient\ \left(\frac{W}{m^2 K} \right)$

Convection coefficient depends on the relation between thickness of the velocity and temperature boundary layers (Prandtl number) and the type of flow (laminar or turbulent) as calculated by the Reynolds number.

$$Pr = \frac{v}{a} = \frac{c_p \mu}{\lambda} \sim \frac{viscous\ dissipation\ rate}{thermal\ diffusion\ rate} \qquad [16]$$

$$Re = \frac{\rho U h}{v} \sim \frac{inertial\ forces}{viscous\ forces} \qquad [17]$$

1.3.4 Viscosity Temperature Relation

As it has already been proposed the oil viscosity is highly dependent on temperature. Increase of temperature rates lead to a decrease of fluid viscosity and has serious impacts on the performance of the oil. Many equations describing the relation between viscosity and temperature have been proposed over the years. In the following computational methods, the equation of McCoull and Walther is used.

$$\log(\log(v + a)) = b - n log(T) \qquad [18]$$

Where **a, b** and **n** are constants, $\boldsymbol{v}$ is the kinematic viscosity and **T** is the temperature.

1.4 Thrust Pad Bearings

Thrust bearings are designed to transfer high axial loads from rotating shafts. They are widely used in the market for many applications such as to support the thrust load of a ship’s or airplane’s propeller. They are also used in hydroelectric power stations and in the automotive industry inside engines and turbines. Several designs of the pads have been proposed over the years. In the marine industry large carrier ships often use tilting pads as shown in **Figure 3**.

Figure 3- Waukesha Tilt Pad Thrust Bearing

1.4.1 Infinite Step Bearing

A simple design that generates hydrodynamic pressure is the Infinite Rayleigh Step geometry. The manufacturing of such geometry is simpler compared to a tilting pad. The step shown in **Figure 4** divides the lubricant film into two levels of film thickness. The geometry parameters h_1 and h_0 control the inlet and outlet conditions.

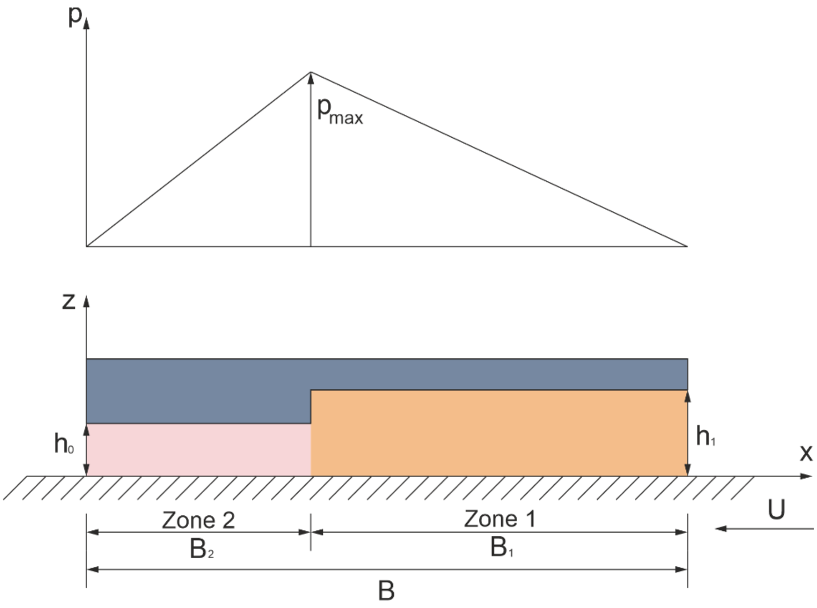

Figure 4 - Rayleigh Step Design

The pressure gradients generated in the two zones are constant. The maximum pressure and thus the maximum load carrying capacity depends on the four geometry parameters h_1, h_0, B_1 and B_2. It has been found that the maximum load carrying capacity occurs for the following ratios:

$$\frac{h_1}{h_0} = 1.87 \; and \; \frac{B_1}{B_2} = 2.588$$

1.4.2 Tapered Land Bearing

Another interesting geometry used widely in practice is the tapered land geometry. In the leading edge a tapered geometry is manufactured and at the end of the pad a flat, often referred as land, is machined, as shown in **Figure 5**. The performance of the bearing depends on the geometry parameters. Many computational results have shown that tapered land bearings are capable of withstanding high axial loads with low friction torque.

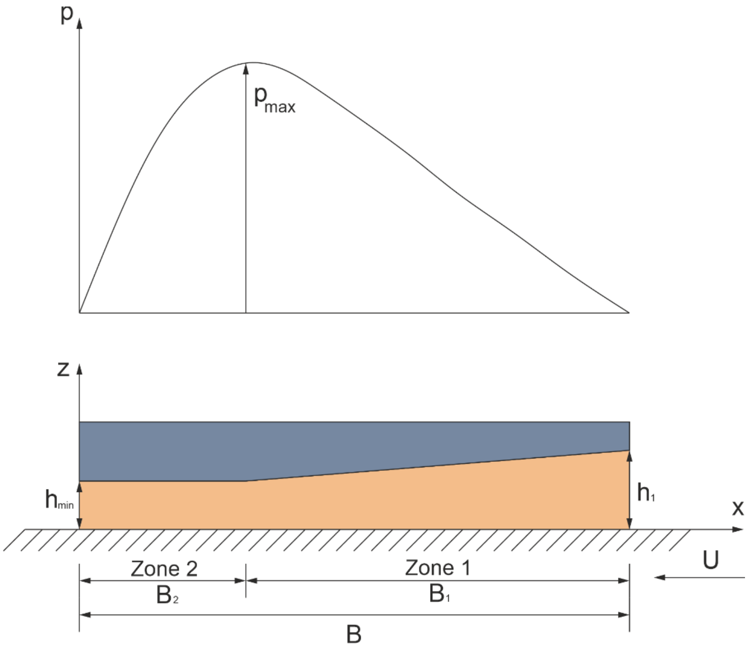

Figure 5 - Tapered Land Design

1.4.3 Parallel Surface Bearing

Experimental results have proved that parallel surface bearings can generate hydrodynamic pressure, which in fact contradicts to the theoretical equations. In theory, two parallel sliding surfaces cannot support load, without severe wear and friction. However, because of the heat produced from the shear of the lubricant, the pad is thermally deformed leading to the formation of a converging geometry on the inlet and a diverging geometry on the outlet. Many materials have significant thermal expansion coefficients and thus considerable thermal distortion occurs. The thermally induced wedge enables hydrodynamic pressure generation. The thermal deformation of the pad is shown in **Figure 6**.

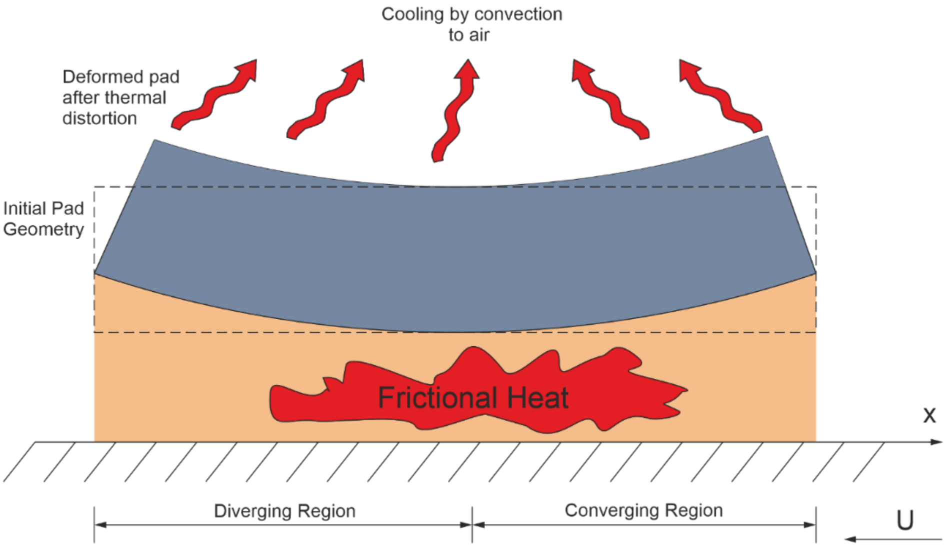

Figure 6 - Thermal deformation of a parallel pad

1.4.4 Parallel Textured Bearing

Recent studies, both experimental and theoretical, have proposed that surface texturing on parallel thrust bearings can significantly improve their tribological performance in terms of load carrying capacity, friction torque and coefficient of friction. Many designs such as rectangular dimples, pockets and circumferential grooves enable the generation of hydrodynamic pressure on the bearing. In textured hydrodynamic bearings, the main problem is defining the optimal parameters of the geometry. Such parameters are the shape of the textures, the depth and the extend. The optimal values differ for every application, thus individual studies must be performed on a per case basis. These parameters strongly depend on the rotational velocity, the specific load, the temperature field and the lubricant properties. Textures can be produced by different techniques such as milling, shot blasting or by laser. A parallel textured bearing with rectangular dimples is shown in **Figure 7**. In **Figure 8** the pressure build-up mechanism of a textured surface is presented.

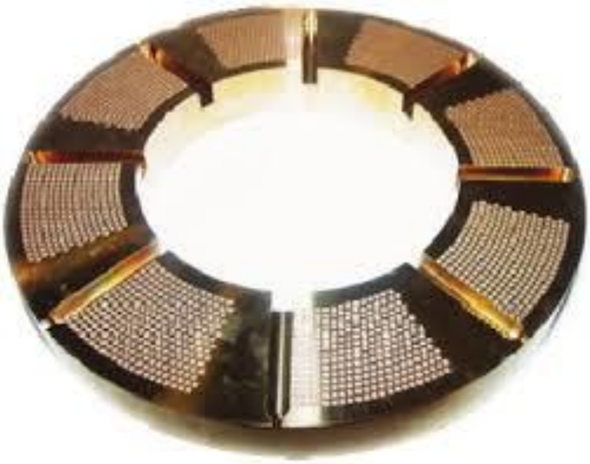

Figure 7 - Parallel textured bearing with rectangular dimples

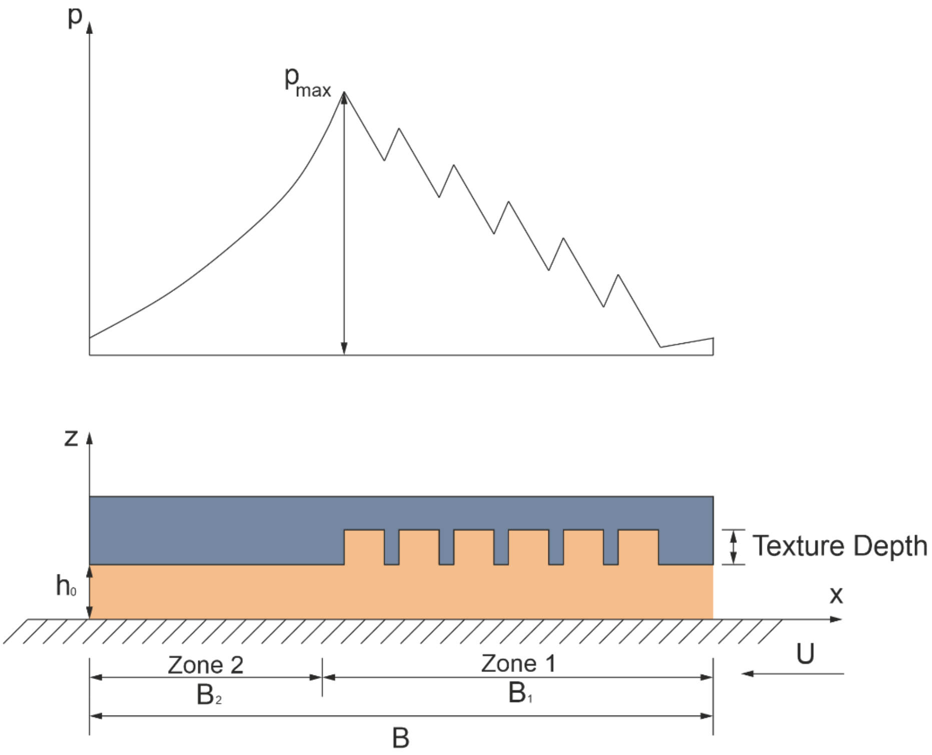

Figure 8 - Pressure build-up on textured surface

2 Computational Study

The Navier-Stokes differential equations exceed the capacity of analytical solutions. The evolution of computer technology has enabled the computation of numerical models in order to solve these equations. The current computational approaches have the potential to take into consideration significant features of the bearing operation, such as heat transfer from the fluid to the rotor and stator, viscous dissipation, alterations of the viscosity and density, thermal and mechanical deformation of the solids. CFD approaches enable on the one hand the quantification of the performance of the bearings and on the other hand the optimisation of geometry parameters depending on the design. Moreover, computational studies can save time and money by aiming to the right direction for manufacturing and experiments. In the case of analyzing thrust bearing performance and optimising geometry parameters the most common approaches in the current literature are Isothermal and ThermoHydroDynamic (THD) models. THD method take into account the heat transfer of the fluid but consider the solids undeformed.

2.1 CFD on Textured Thrust Bearings

Many studies have been conducted aiming at optimising texture design and evaluating the effects of texturing on the tribological characteristics of thrust bearings [20-22]. In most of the studies, the conclusion drawn was that, for each application, the optimal texture parameters differ (in terms of texture region, shape, depth), thus individual studies need to be performed on a per-case basis [23]. Moreover, the optimised textured parameters have shown to improve the performance characteristics of the bearings in a narrow range of operating conditions, but both computational [8] and experimental studies [24] have pointed out that, for high values of specific pressure, the positive effect of textures decreases dramatically, whereas, in some conditions, even a plain parallel thrust bearing exhibits better tribological characteristics than a partially textured thrust bearing optimised for different operating conditions [24]. At high values of specific pressure, mechanical and/or thermal deformations of the bearing geometry become significant, therefore more advanced modelling procedures are required, in order to evaluate the optimal texture geometry of the bearings [25].

The present study consists of two logical parts. The first part is to identify several optimal textured parallel thrust bearing geometries, utilising the state-of-the-art approach from the current literature [8]. Thus, a 3D CFD approach has been selected. A thermo-hydrodynamic (THD) model has been generated, considering viscous dissipation, solution of the energy equation in the fluid domain, and conjugate heat transfer through the solid domains. An optimisation problem has been defined, with two objective functions, namely the load carrying capacity (LLC) and the friction torque. A genetic algorithm optimisation technique has been utilised according to Papadopoulos et al. [10]. After the optimisation has been concluded, a parametric analysis has been performed in a small range of the optimised parameters in order to identify if the optimised geometry is indeed the global optimum.

In the second part of the present study, a thermo-elasto-hydrodynamic (TEHD) model has been generated, taking into consideration the mechanical and thermal deformation of the pad domain. The THD optimised geometries have been re-evaluated with the TEHD modelling approach. Moreover, a second parametric analysis has been performed, in order to identify, with the more advanced TEHD modelling approach, whether the previous identified optima are in fact the optima for the specific operating conditions.

2.2 Genetic Algorithm Optimisation

The development of computational technology has enabled the use of complex methods for optimisation. Genetic algorithms have been introduced, in order to save computational cost and overcome certain difficulties, encountered in classical optimisation algorithms. The genetic algorithm is a method for solving both constrained and unconstrained optimisation problems that is based on natural selection, the process that drives biological evolution. [29] The genetic algorithm repeatedly modifies a population of individual solutions. At each step, the genetic algorithm selects individuals at random from the current population to be parents and uses them to produce the children for the next generation. Over successive generations, the population "evolves" toward an optimal solution. For problems that include several objective functions that are high nonlinear, discontinuous or stochastic genetic algorithms can be applied. Such problems are the optimisation of hydrodynamic bearing geometry parameters. The algorithm initialises by creating a random initial population. The algorithm then creates a sequence of new populations. At each step, the algorithm uses the individuals in the current generation to create the next population, according to three main type of rules [15]:

- **Selection Rules** which select the individuals, often referred as ‘parents’, that contribute to the population of the next generation
- **Crossover Rules** which combine two parents to form children for the next generation
- **Mutation Rules** which apply random changes to individuals to form new children.

The algorithms stop when one of the stopping in criteria is met. In each generation, the collection of all non-dominated solutions is the Pareto front, identified by utilising the concept of Pareto Ranking [10] outlined on **Figure 9**.

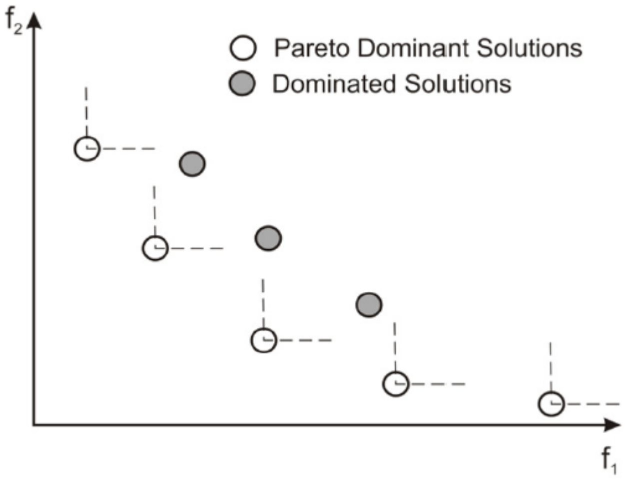

Figure 9 - Pareto Front

In the present study, optimisation parameters of the textured surface geometry is performed by coupling the CFD solver with an optimisation tool which utilises the ParadisEO genetic algorithm library [26]. The latter adopts the Non-dominated Sorting Genetic Algorithm NSGA-II for pareto ranking [27]. An outline of the procedure is presented on **Figure 10**.

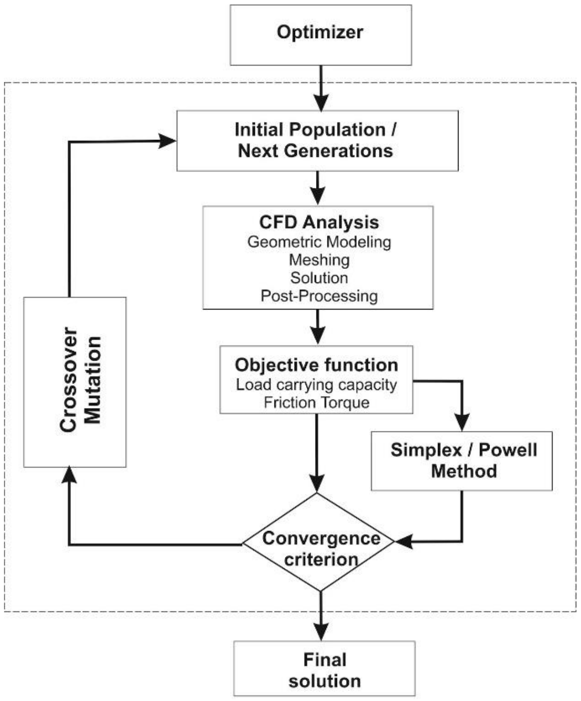

Figure 10 - Optimisation Procedure

In the present models, the conservation equations are solved with the CFD code ANSYS CFX, for steady, incompressible flow, with no gravitational forces and cavitation modeling. The equations are presented below:

Mass conservation equation: $\nabla \cdot V = 0$ [18]
Momentum equations: $\rho(V\Delta)V = -\nabla p + \nabla \cdot (\mu \cdot \nabla V)$ [19]
Energy equation, fluid domain: $\rho \cdot c_{pf} \cdot v \cdot \nabla T = \nabla(\lambda_f \cdot \nabla T) + \mu\Phi$ [20]
Energy equation, solid domains: $\nabla(\lambda_s \cdot \nabla T) = 0$ [21]

Where V is the velocity vector (m/s), p the static pressure (Pa), T the temperature (K), τ the viscous stress tensor, ρ the oil density (kg/m3), μ the oil dynamic viscosity (kg/m.s), cpf the oil specific heat capacity (J/kg.K), λf the oil thermal conductivity (W/m.K), λs the rotor thermal conductivity (W/m.K). The dissipation term Φ describes the heat generated by internal fluid friction.

The load LCC of the sector pad is calculated as the integral of pressure over the fluid/pad interface:

$$LCC = \iint_{FSI} p(x, y)\,\mathrm{d}x\,\mathrm{d}y \qquad [22]$$

The friction force is calculated as the integral of the shear force component over the fluid/pad interface.

$$Fr = \iint_{FSI} F_y(x, y)\,\mathrm{d}x\,\mathrm{d}y \qquad [23]$$

The friction coefficient is calculated by dividing the Friction Torque with the LCC and the mid-radius.

$$COF = \frac{Fr}{LCC \times Rmid} \qquad [24]$$

2.3 Circumferential Grooves Optimisation

2.3.1 Basic Geometry

The present computational model consists of three domains: the pad, the fluid, and the rotor. The geometrical dimensions and operating conditions have been selected as close as possible to those of the thrust bearing of the experiment of Henry et al. [24]. The fluid domain is defined by the space between the rotor and pad, which contains the thin film region and half groove fore and half groove aft. This configuration has been selected in order to account for the oil mixing and the hot oil carry-over phenomena. The rotational Velocity has been set at 4000 RPM.

Table 1– Dimensions of the thrust bearing model of the present study

Dimension	Value	Units
Pad Length (L)	45	deg
Pad Width (B)	20	mm
Pad Thickness	10	mm
Rotor Thickness	10	mm
Groove Length	3	mm
Groove Depth	4	mm

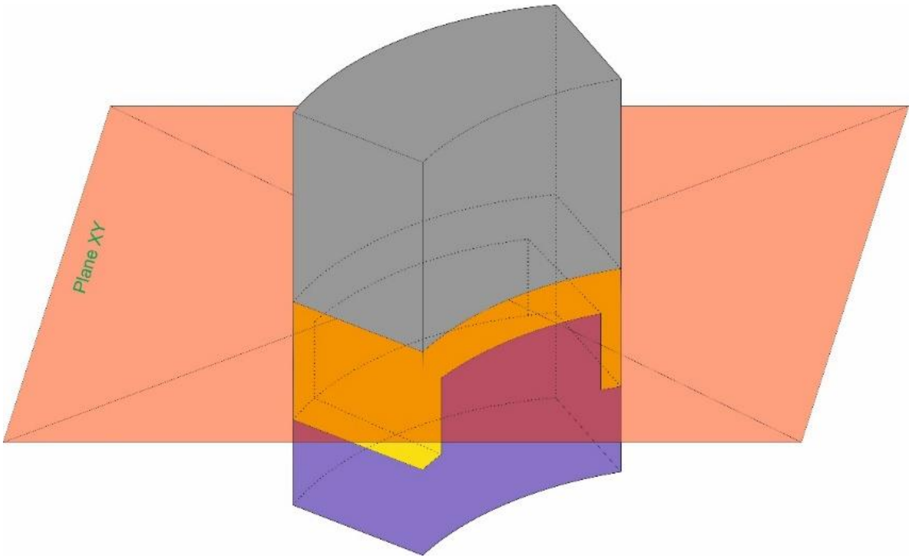

Figure 11 – Calculation domains of the sector pad thrust bearing

2.3.2 Texture Geometry Parameters

The designed texture geometry consists of 9 circumferential grooves with a constant density of 90% The overall textured width is constant at 90% of the total pad width. The length of the circumferential grooves is calculated for each one with 3 main parameters. The textured depth is constant for all grooves in the study varied between 10 μm to 80 μm. A schematic of the texture geometry is presented on **Figure 12**.

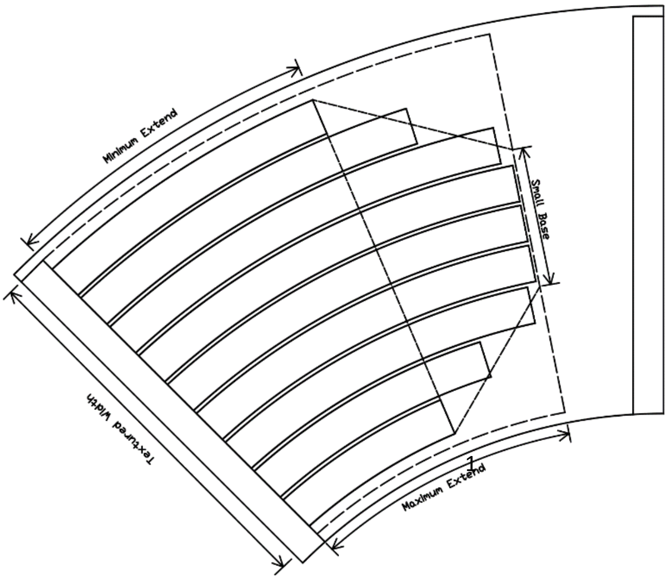

Figure 12 – Surface Texture Geometry

The maximum extend is calculated as a percentage of the total pad length without the grooves. The minimum extend is calculated as a percentage of the maximum extend. The length of the mid grooves is calculated depending on the small base of the trapezoid, which is taken as a percentage of the total textured width.

2.3.3 Meshing procedure

The final mesh parameters have been selected following a detailed mesh study. Regarding the pad domain a dense hexahedral mesh has been utilised, composed of 1.6 million elements. The fluid domain is discretised with hexahedral elements, utilising 15 layers of elements in the crossflow (film thickness) direction, whereas in the longitudinal and transverse directions, 190 and 110 elements have been used, respectively. The total number of elements in the fluid domain is 726,000, and in the rotor domain is 300,000. The rotor domain is assumed rigid, therefore, only the heat transfer equations are solved. Mesh details about the computational domain are presented in **Figure 13-15**.

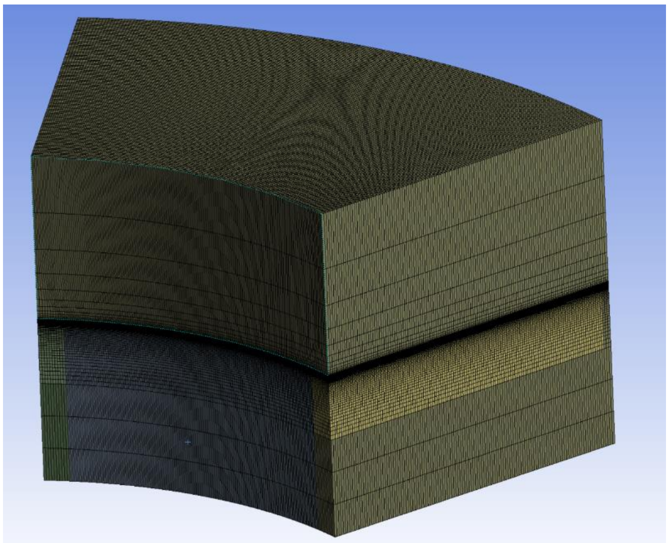

Figure 13 - All Mesh components

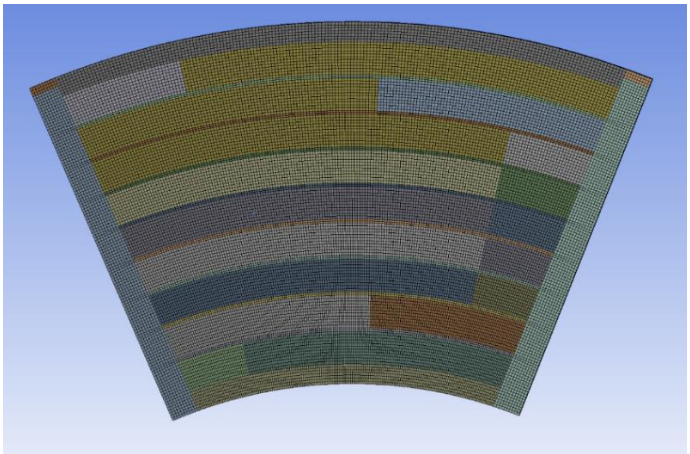

Figure 14 – Top view of Fluid Mesh

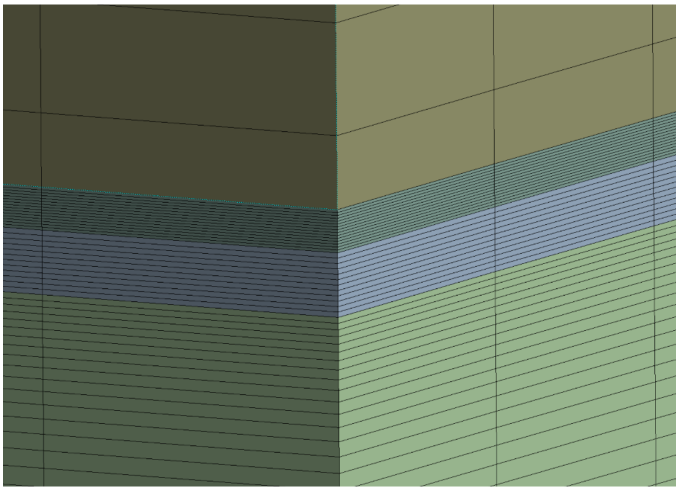

Figure 15 - Fluid crossflow mesh details

2.3.4 Boundary Conditions

The pad is consider fully flooded, with feeding pressure at the fluid inner surface, as denoted in **Figure 16**. The thermal boundary conditions of the thrust bearing system have been considered following the work in [23], see **Figure 16** and **Table 4**. The rotor is considered rigid. The pad is considered fixed on the bottom surface (no displacements or rotations allowed). The thermophysical properties of the pad and rotor materials are presented in Table 2. The thermophysical properties of the oil are presented in Table 3. The density of the lubrication oil utilised (ISO VG 46) is 870 kg/m3, while a temperature dependent viscosity is considered, modeled according to the McCoull and Walther relation [24]:

$$log(log(v+a)\,) = b - nlog(T)$$

where, v is the kinematic viscosity (cSt), T is the temperature and a = 0.6, b = 9.02865 and
n = 3.52681.

Table 2 - Thermophysical properties of rotor/pad materials

Property	Rotor/Pad (Steel)	Units
Specific Heat Capacity	434	J/(kg.K)
Thermal Conductivity	60.5	W/(m.K)
Molar Mass	55.85	kg/kmol
Density	7854	kg/m^3
Thermal Expansion Coef.	$1.2x10^{-5}$	C^{-1}
Young's Modulus	215	GPa

Table 3 - Thermophysical oil properties

Iso VG46 Oil Parameters			
Symbol	Value	Units	Comments
ρ	870	kg m^3	Oil density
c	2.1	kJ (kg.K)	Specific heat capacity
k	0.13	W/(m.K)	Thermal conductivity

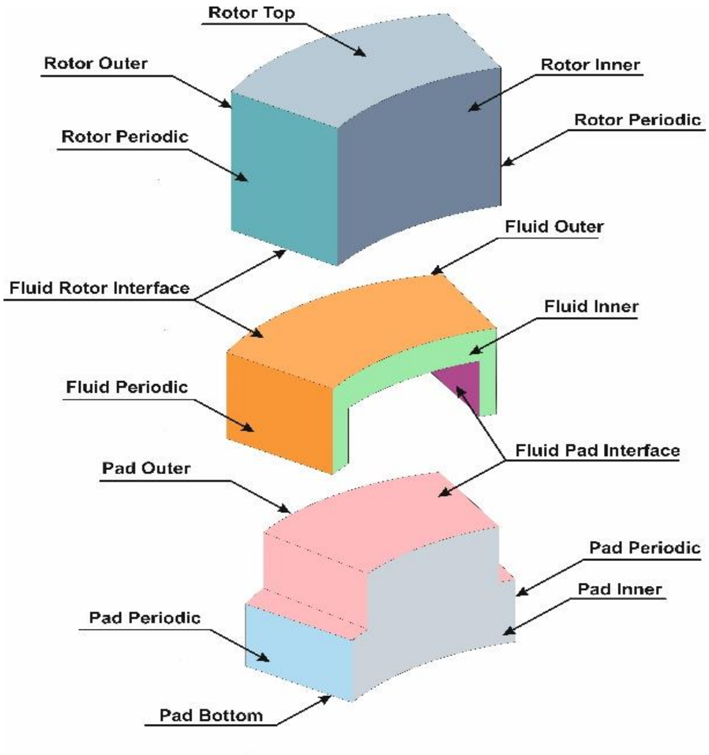

Figure 16 - Computational model: designation of domains surfaces

Table 4 - Boundary conditions of the models

Pad		
Top surface	Fluid-Solid interface: Continuity of heat flux and temperature	Free displacement in all directions
Bottom surface	Heat transfer coefficient: 25 W/(m^2.K), T=20 °C	Fixed
Inner surface	Heat transfer coefficient: 350 W/(m^2.K), T=50 °C	Free displacement in all directions
Outer surface	Heat transfer coefficient: 25 W/(m^2.K), T=20 °C	Free displacement in all directions
Sides	Periodic conditions	Free displacement in z and x directions
Rotor		
Top surface	Heat transfer coefficient: 25 W/(m^2.K), T=20 °C	Fixed
Bottom surface	Fluid-Solid interface: Continuity of heat flux and temperature	Fixed
Inner surface	Heat transfer coefficient: 1000 W/(m^2.K), T=20 °C	Fixed
Outer surface	Heat transfer coefficient: 25 W/(m^2.), T=20 °C	Fixed
Sides	Periodic conditions	Fixed
Fluid		
Fluid/Rotor interface	Fluid-Solid interface: Continuity of heat flux and temperature	Fixed
Fluid/Pad interface	Fluid-Solid interface: Continuity of heat flux and temperature	Free displacement in all directions
Fluid Sides	Periodic conditions	Free displacement in z and x directions
Fluid Inner surface	Opening with temperature 50 °C and static relative pressure 1.2 bar	Free displacement in z and x directions
Fluid Outer surface	Opening with temperature 20 °C and static relative pressure 0 bar	Free displacement in z and x directions

2.3.5 Results

The THD model optimisation results are depicted in **Figure 17**. The red points are the pareto optimal designs, and the blue ones all the calculated intestines of the parametric model. As it can be observed from **Figure 17**, no specific congestion points have been identified. The optimal design parameters that have been selected for the current study are of the pareto point with the largest value of LLC. In Table 5 the selected parameter set is presented.

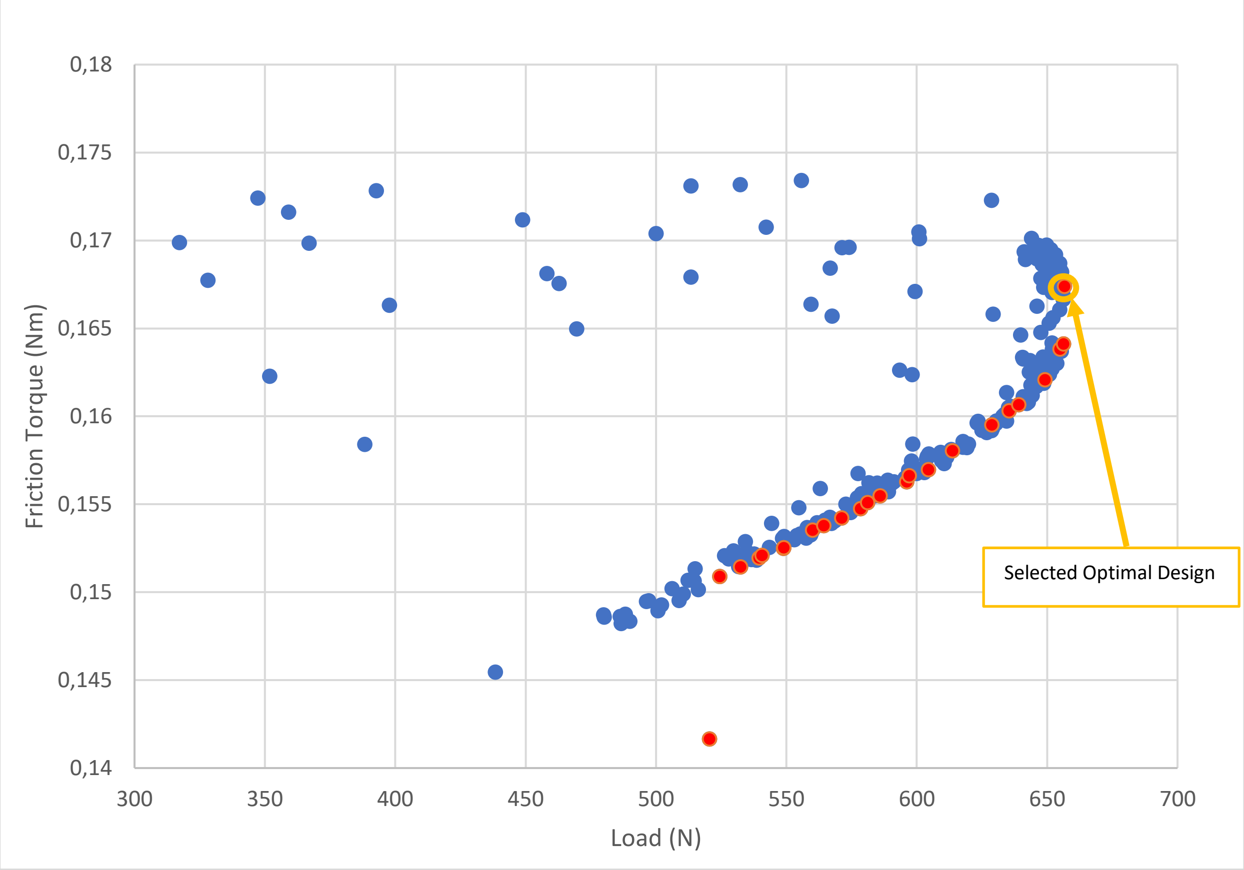

Figure 17 - Optimisation Pareto front

Table 5 – Selected Optimal Parameters

Selected Optimal Parameter Set	
Textured Dpeth	39.92 μm
Textured Minimum Length	78.82%
Textured Maximum Length	79.64%
Textured Small Base	57.76%
Objective Function Values	
Load Carrying Capacity	656.66 N
Friction Torque	0.167 Nm
COF	0.00730

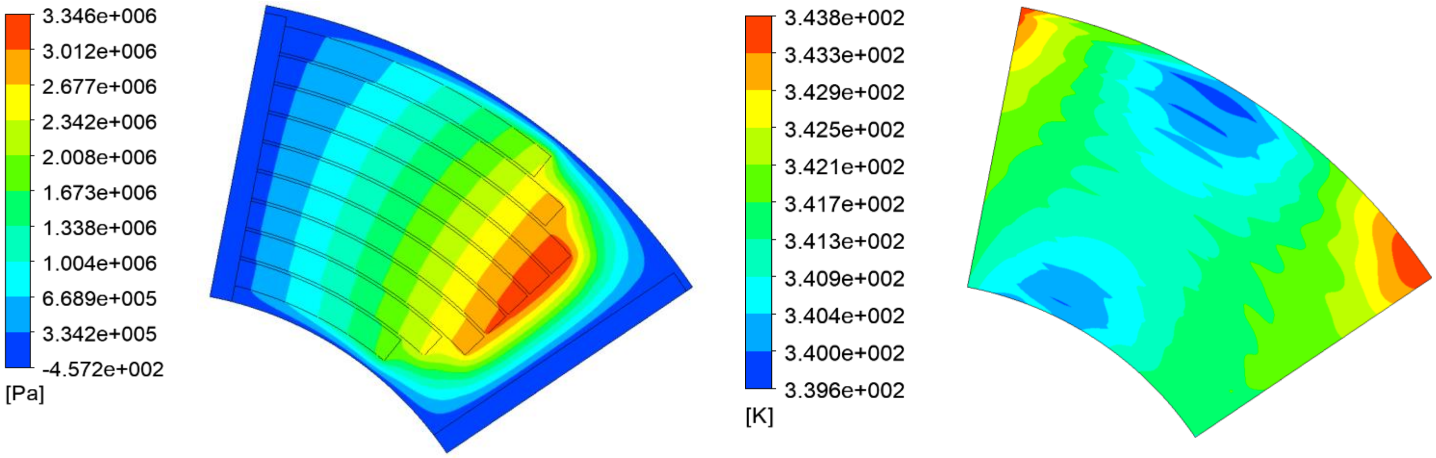

(a) **(b)**

Figure 18 – a) Pressure Field at Fluid-Pad Interface, b) Temperature Field at Fluid-Rotor Interface

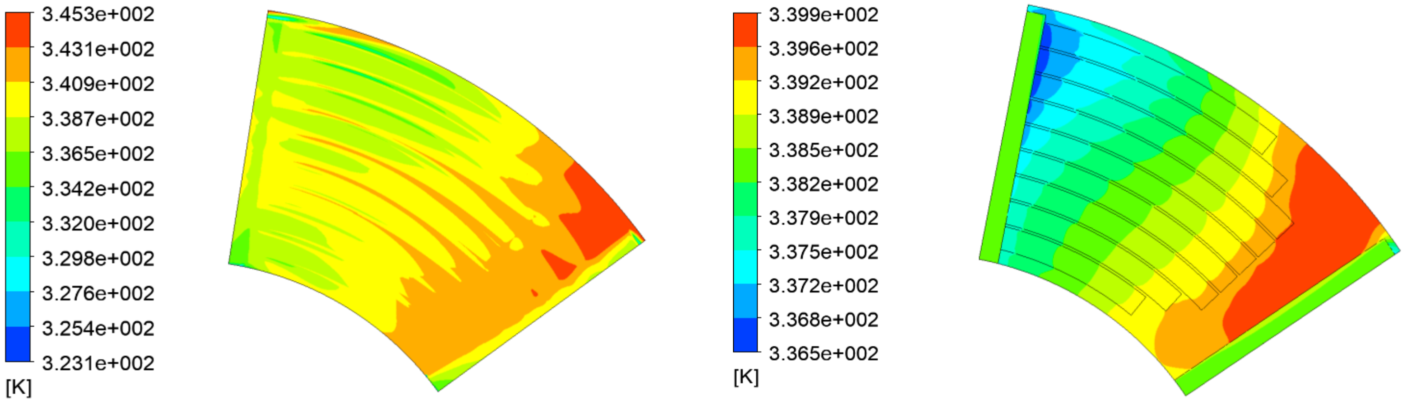

(a) **(b)**

Figure 19 –Temperature Field at a) Midline of film Thickness b) Fluid-Pad Interface

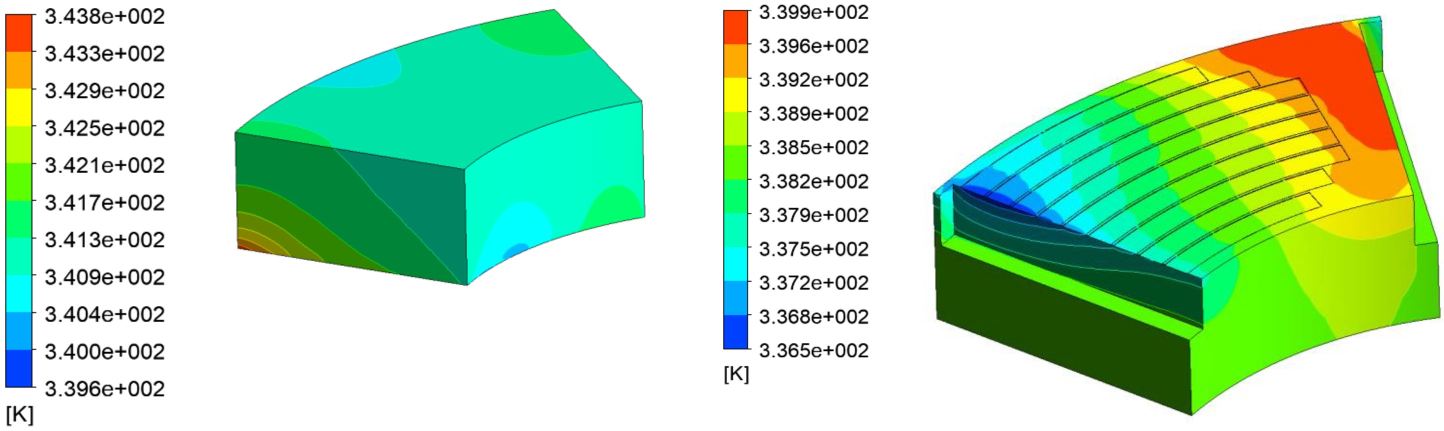

(a) **(b)**

Figure 20 – Temperature Field at a) Rotor Domain b) Pad Domain

The maximum oil Pressure was calculated at 3.35 MPa, resulting in an overall Load Carrying Capacity of 656.6N, a friction torque of 0.167 Nm and a Coefficient of Friction of 0.0073. The maximum oil temperature was calculated at 72.6 ℃ at a reference minimum film thickness of 20μm. The pressure field at the Fluid-Pad interface is shown on **Figure 18**. The maximum pressure occurs at the end of the textured surface area. The maximum temperature occurs on the midline of the minimum film thickness, on **Figure 19a**. Due to the contact with the stator on the bottom and the rotor on top, the oil is cooled through convection, thus the temperature fields are lower on these interfaces, as seen on **Figure 18b** and **Figure 19b.** The hot oil is concentrated on the outer radius of the trailing edge, thus the temperatures are higher in this region, as observed on **Figure 20b.** The fluid is heated due to shear stress as it enters the pad domain, and the hot oil is forced on the outer region due to centrifugal forces.

Table 6 – Optimal Design Results

Min. Film Thickness	20 μm
Max Oil Pressure	3.35 MPa
Load Carrying Capacity	656.6 N
Friction Torque	0.167 Nm
Coefficient of Friction	0.0073
Max Oil Temperature	72.6 ℃

The hydrodynamic pressure generation occurs according to the infinite Rayleigh step geometry as seen on **Figure 4**. In this case multiple circumferential steps have been designed and a multidimensional pressure profile is generated. The pressure profile on the circumferential direction at a the midline of the pas is shown on **Figure 21** along with the temperature on **Figure 22**. Moreover, the pressure and temperature profiles on the radial direction at 27° are shown on **Figure 23** and **Figure 24** respectively. Pressure profiles for various radii and angles were calculated in order to generate a 3D-represantation of the pressure distribution on the pad, as presented on **Figure 25** and **Figure 26**.

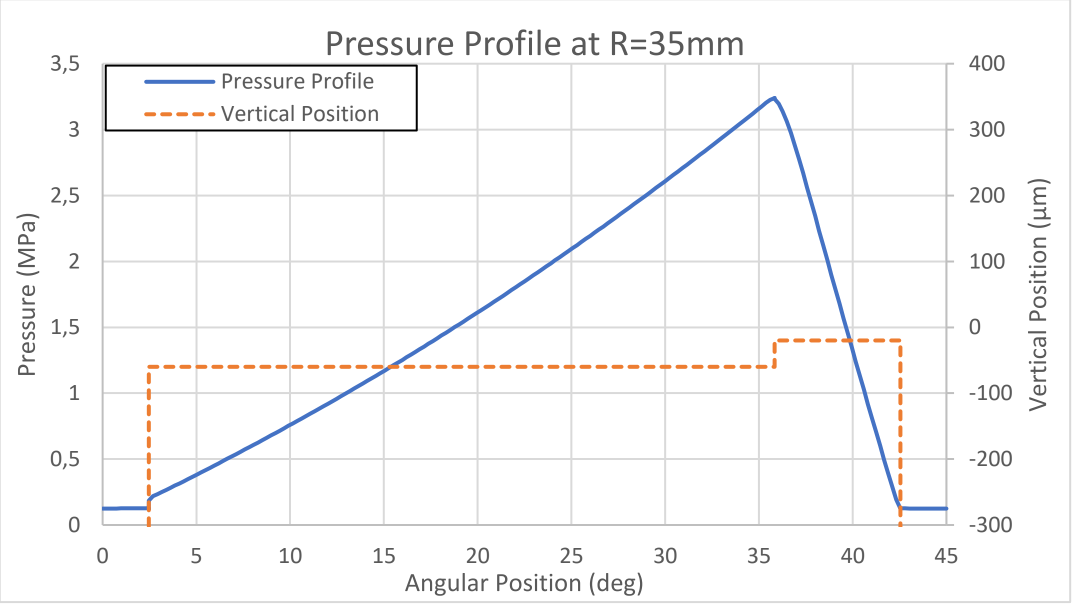

Figure 21 – Pressure Profile at 35mm Radius

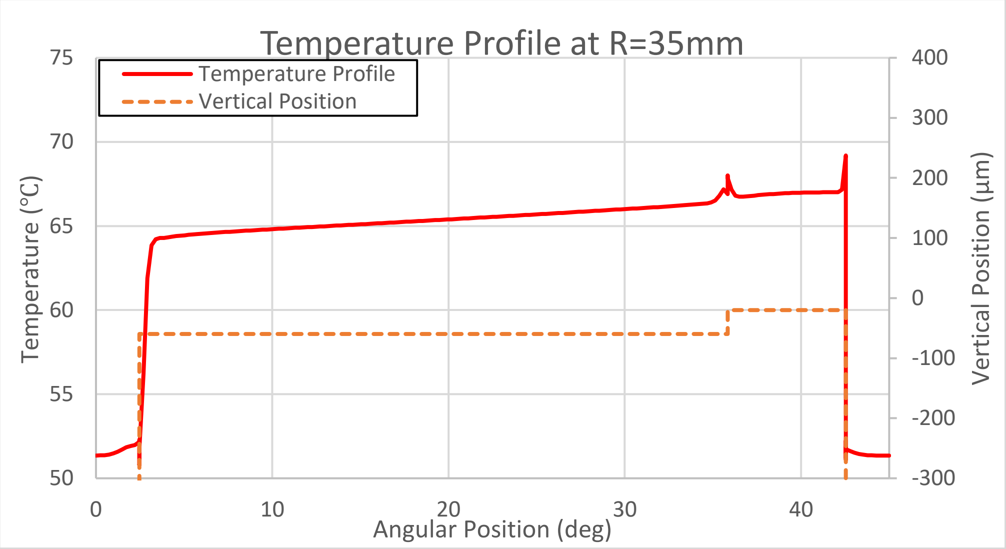

Figure 22 – Temperature Profile at 35mm Radius

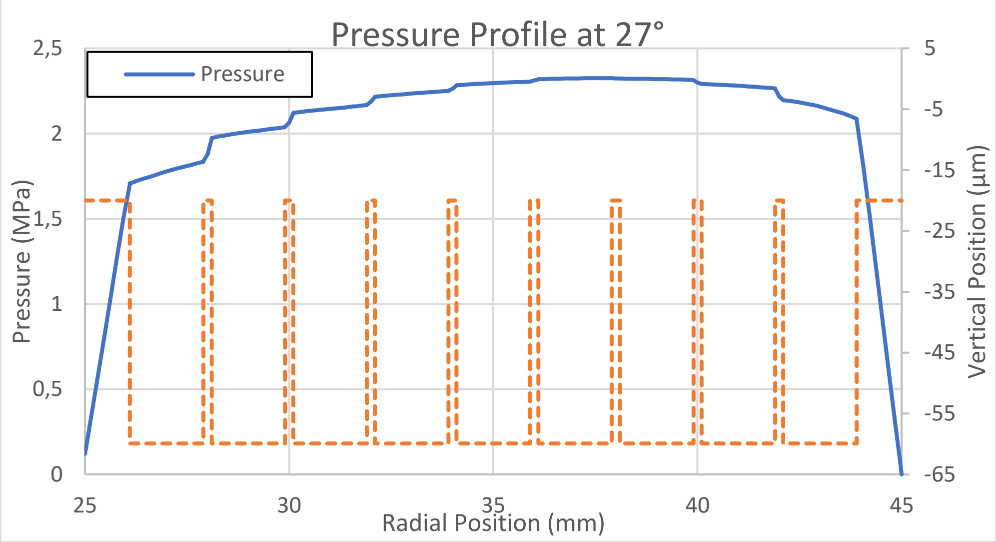

Figure 23 – Pressure Profile at 27°

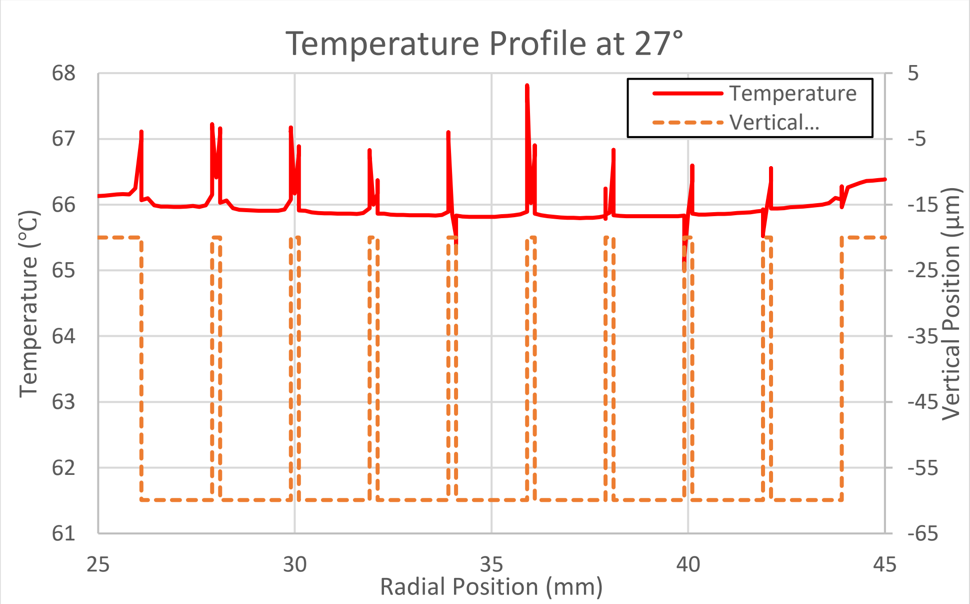

Figure 24 – Temperature Profile at 27°

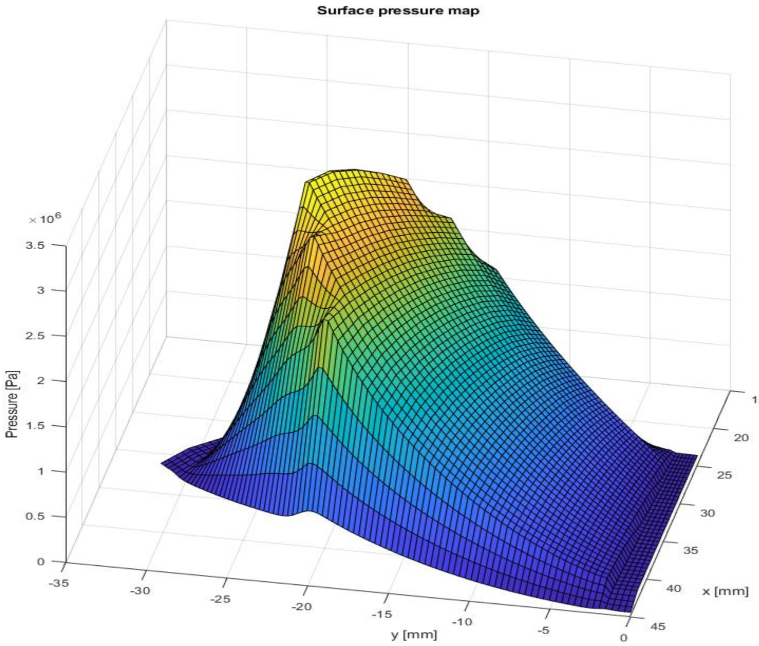

Figure 25 – 3-D Pressure Field

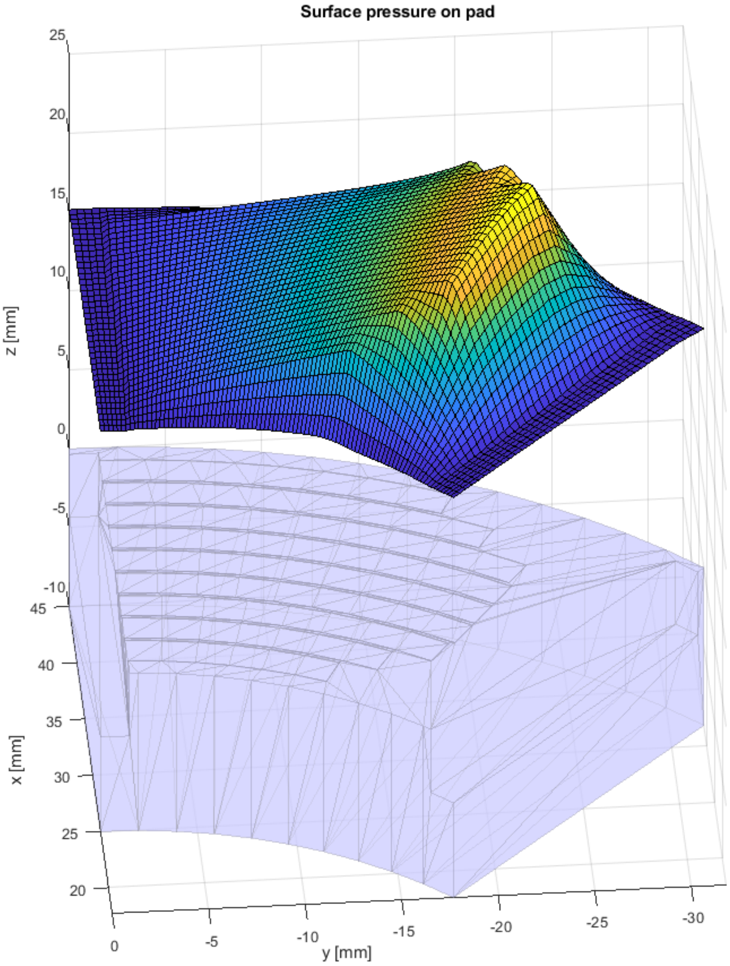

Figure 26 – 3-D Pressure Field on Pad

2.4 Rectangular Dimples Optimisation

2.4.1 Basic Geometry

The present computational models consist of three domains: the pad, the fluid, and the rotor. All domains are depicted in **Figure 16**. The geometrical dimensions and operating conditions have been selected as close as possible to those of the thrust bearing of the experiment of Henry et al. [24], and the dimensions are displayed in **Table 7**. The fluid domain is defined by the space between the rotor and pad, which contains the thin film region and half groove fore and half groove aft. This configuration has been selected in order to account for the oil mixing and the hot oil carry-over phenomena.

Table 7 – Dimensions of the thrust bearing model of the present study

Dimension	Value	Units
Pad Length (L)	45	deg
Pad Width (B)	20	mm
Pad Thickness	10	mm
Rotor Thickness	20	mm
Groove Length	3	mm
Groove Depth	4	mm

2.4.2 Texture Geometry Parameters

The designed textured geometry consists of 24 rectangular, 6 dimples in the circumferential direction and 4 dimples in the radial direction with a constant density (ρ) at 80%. Schematic of the texture configuration is presented on **Figure 27**. The overall textured width is calculated as a percentage of the total pad width and the textured length as a percentage of the total pad length, excluding the grooves. The textured depth is constant for all the dimples and in this study varied between 10 μm to 50 μm.

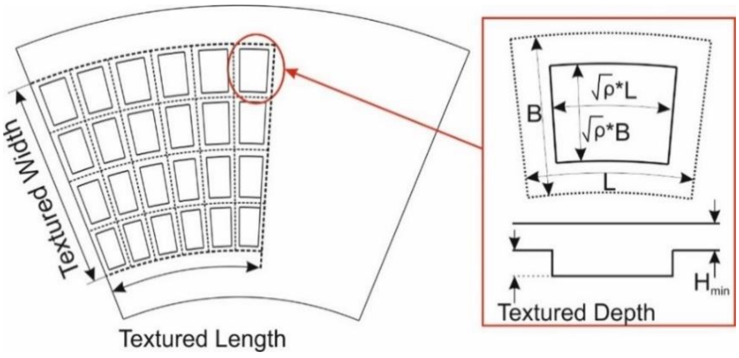

Figure 27 - Optimisation parameters of the textured geometry

2.4.3 Meshing procedure

The mesh for both models is identical. The final mesh parameters have been selected following a detailed mesh study. Regarding the pad domain, due to the thermal and mechanical deformations, a dense hexahedral mesh has been utilised, composed of 910,000elements. The fluid domain is discretised with hexahedral elements, utilising 15 layers of elements in the crossflow (film thickness) direction, whereas in the longitudinal and transverse directions, 150 and 60 elements have been used, respectively. The total number of elements in the fluid domain is 340,000, and in the rotor domain is 350,000. The rotor is assumed rigid, therefore, only the heat transfer equations are solved. Mesh details about the computational domains are presented in **Figure 28-30**.

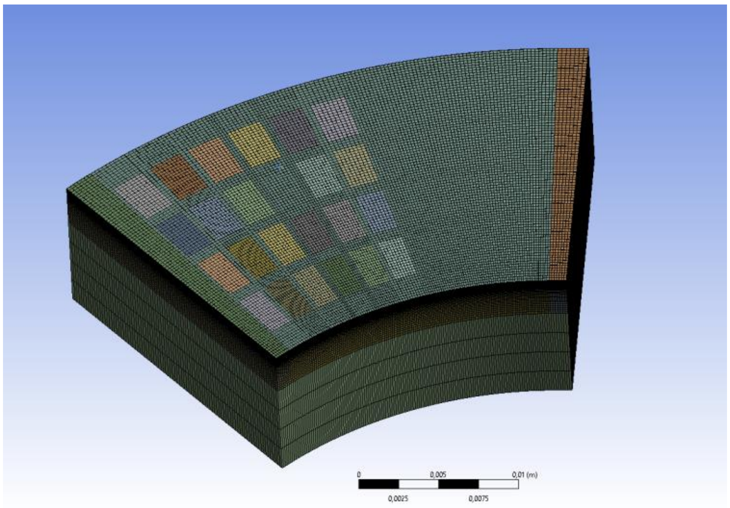

Figure 28 - Top view of fluid mesh

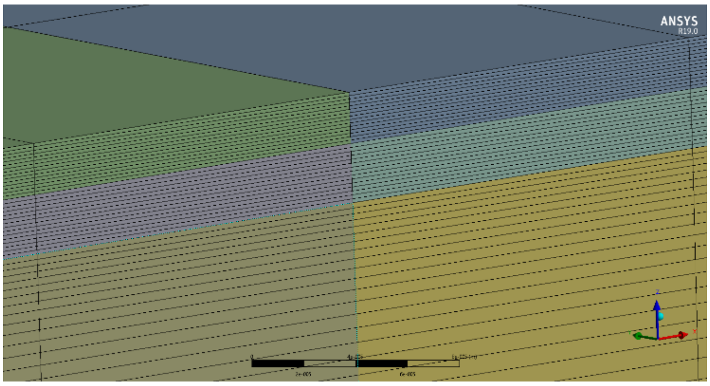

Figure 29 - Fluid cross-flow mesh details

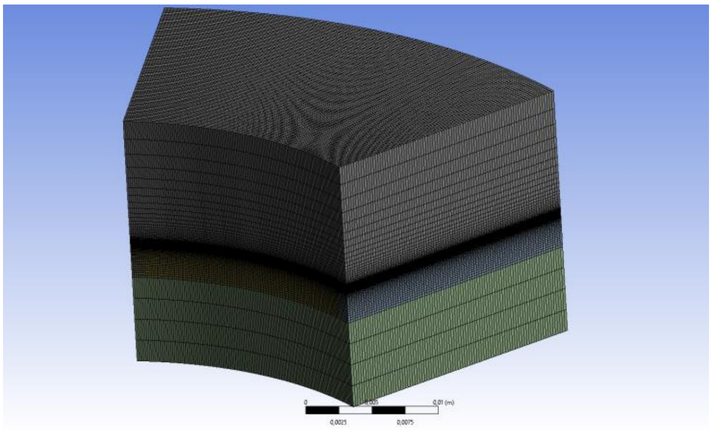

Figure 30 - View of all three domain mesh details

2.4.4 Boundary Conditions

The pad is consider fully flooded, with feeding pressure at the fluid inner surface, as denoted in **Figure 16**. The thermal boundary conditions of the thrust bearing system have been considered following the work in [8], see **Figure 16** and **Table 8**. The rotor is considered rigid. The pad is considered fixed on the bottom surface (no displacements or rotations allowed). The thermophysical properties of the pad and rotor material are presented in **Table 9**. The thermophysical properties of the oil are presented in Table 3. The density of the lubrication oil utilised (ISO VG 46) is 870 kg/m3, while a temperature dependent viscosity is considered, modeled according to the McCoull and Walther relation [24]:

$$log(log(v + a)\ ) = b - nlog(T)$$

where, v is the kinematic viscosity (cSt), T is the temperature and a = 0.6, b = 9.02865 and n = 3.52681. Finally, the rotational speed of all calculations on this study has been set at 6000 RPM.

Table 8 - Boundary conditions of the models

Pad		
Top surface	Fluid-Solid interface: Continuity of heat flux and temperature	Free displacement in all directions
Bottom surface	Heat transfer coefficient: 1000 W/(m^2.K), T=40 °C	Fixed
Inner surface	Heat transfer coefficient: 200 W/(m^2.K), T=40 °C	Free displacement in all directions
Outer surface	Heat transfer coefficient: 25 W/(m^2.K), T=40 °C	Free displacement in all directions
Sides	Periodic conditions	Free displacement in z and x directions
Rotor		
Top surface	Heat transfer coefficient: 25 W/(m^2.K), T=20 °C	Fixed
Bottom surface	Fluid-Solid interface: Continuity of heat flux and temperature	Fixed
Inner surface	Heat transfer coefficient: 1000 W/(m^2.K), T=20 °C	Fixed
Outer surface	Heat transfer coefficient: 25 W/(m^2.), T=20 °C	Fixed
Sides	Periodic conditions	Fixed
Fluid		
Fluid/Rotor interface	Fluid-Solid interface: Continuity of heat flux and temperature	Fixed
Fluid/Pad interface	Fluid-Solid interface: Continuity of heat flux and temperature	Free displacement in all directions
Fluid Sides	Periodic conditions	Free displacement in z and x directions
Fluid Inner surface	Opening with temperature 40 °C and static relative pressure 1 bar	Free displacement in z and x directions
Fluid Outer surface	Opening with temperature 20 °C and static relative pressure 0 bar	Free displacement in z and x directions

Table 9 - Thermophysical properties of the pad and rotor materials.

Property	**Rotor/Pad (Steel)**	**Units**
Specific Heat Capacity	434	J/(kg.K)
Thermal Conductivity	60.5	W/(m.K)
Molar Mass	55.85	kg/kmol
Density	7854	kg/m^3
Thermal Expansion Coef.	$1.2x10^{-5}$	C^{-1}
Young's Modulus	215	GPa

2.4.5 Results

The THD model optimisation results are depicted in **Figure 31**. The red points are the pareto optimal designs, and the blue ones all the calculated intestines of the parametric model. As it can be observed from **Figure 31**, no specific congestion points have been identified. The optimal design parameters that have been selected for the current study are those of the Pareto point with the smallest coefficient of friction, which is also the one with the largest value of LCC. In the selected parameter set is presented.

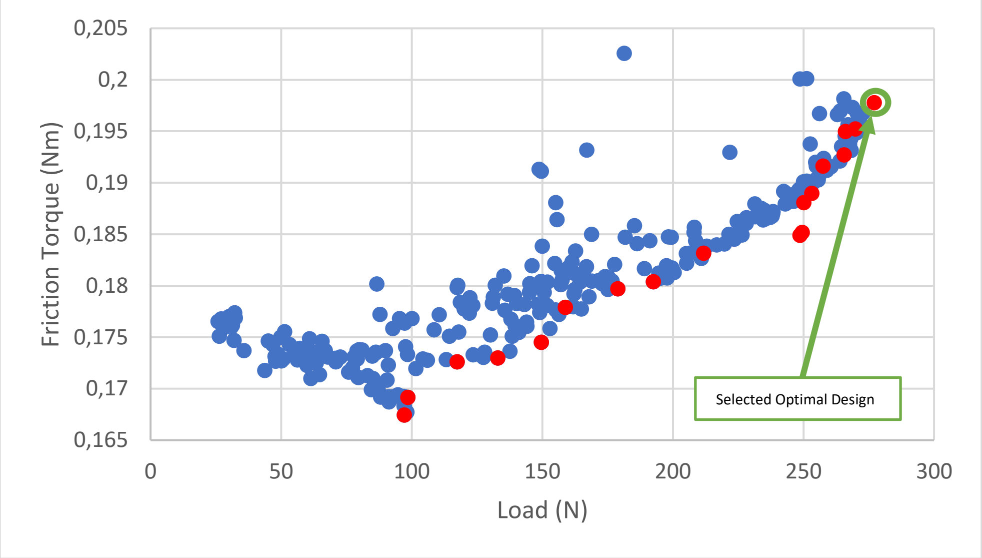

Figure 31 – Optimisation Pareto front

Table 9 – Selected Optimal Design Parameters

Selected Optimal Parameter Set	
Texture Length	56.20%
Texture Width	84.70%
Textured Depth	23 μm
Objective Function Values	
Load Carrying Capacity	278.2 N
Friction Torque	0.198 Nm
Coefficient of Friction	0.0203

The resulting pressure field of the THD optimal configuration is outlined on **Figure 32a.** The maximum oil pressure has been calculated at 1.75 MPa, resulting in an overall LCC of 278.2N, a friction torque of 0.198 Nm and a coefficient of friction of 0.0203. On the second dimple of the outer radius, a pressure drop occurs, and therefore a cavitating region has been created, as seen on **Figure 32b.** The maximum oil temperature has been calculated at 92.7 ℃ at the midline of the film thickness as displayed on **Figure 33b.** At the fluid-pad and fluid-rotor interface the temperature is higher on the outer radius of the trailing edge, as seen on **Figure 32a** and **Figure 34a**. The oil entering the pad is heated due to shear stresses, and the centrifugal forces, force the hot oil to gather on the outer radius of the trailing edge. The temperature of the rotor is significantly higher compared to the stator in **Figure 34b.** The calculated results are presented on **Table 10**.

Table 10 – THD Optimal Design Results

Min. Film Thickness	20 µm
Max Oil Pressure	1.75 MPa
Load Carrying Capacity	278.2 N
Friction Torque	0.198 Nm
Coefficient of Friction	0.0203
Max Oil Temperature	92.7 °C
Max Air/Oil Vol. Fraction	92.80%

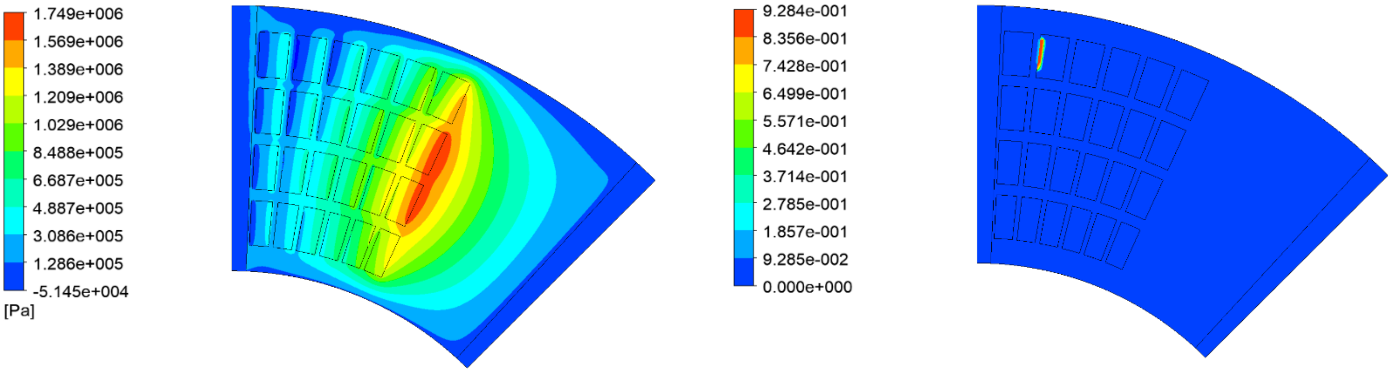

(a) **(b)**

Figure 32 – a) Pressure field at the fluid-pad interface, b) Volume fraction field (blue: liquid oil, red: oil vapor) at the fluid-pad interface

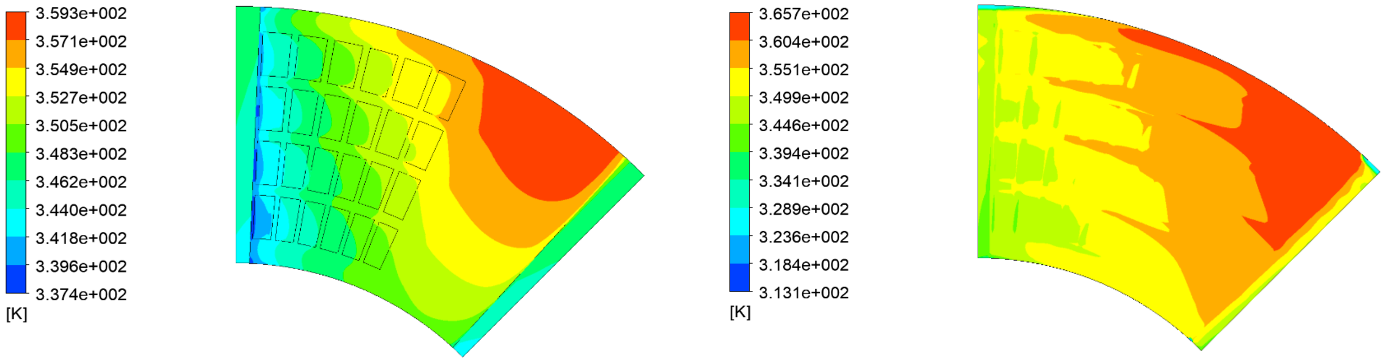

(a) **(b)**

Figure 33 – Temperature field at a) fluid- pad interface, b) Midline of Film Thickness

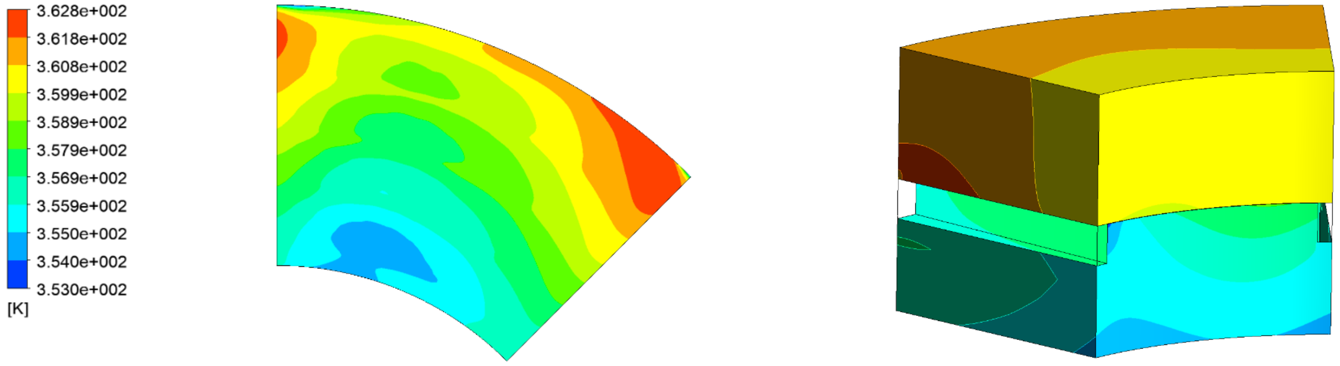

(a) **(b)**

Figure 34 – Temperature field a) fluid- rotor interface, b) pad and rotor outer surfaces

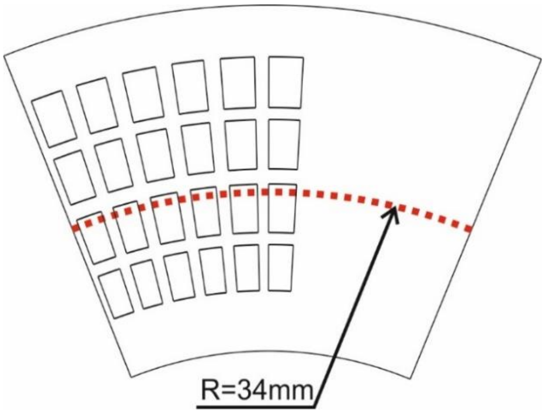

Figure 35 - Circumferential line at a radius of 34mm

In order to understand the pressure build up mechanism, the pressure profile has been calculated at a radius of 34 mm in **Figure 36**. The temperature at the same radius can be observed in **Figure 37**.

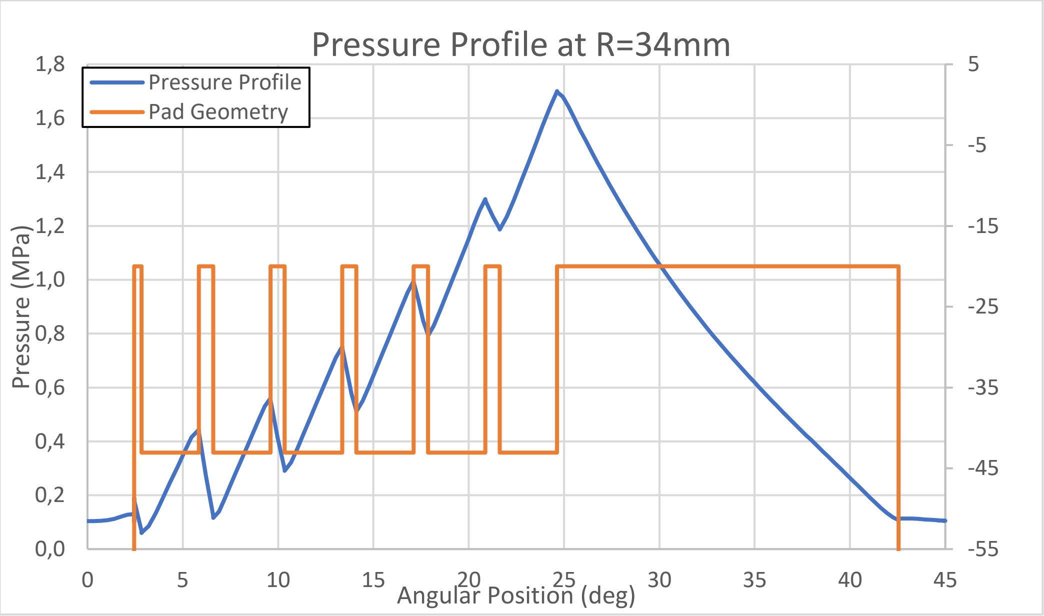

Figure 36 – Circumferential Pressure Profile at R=34mm

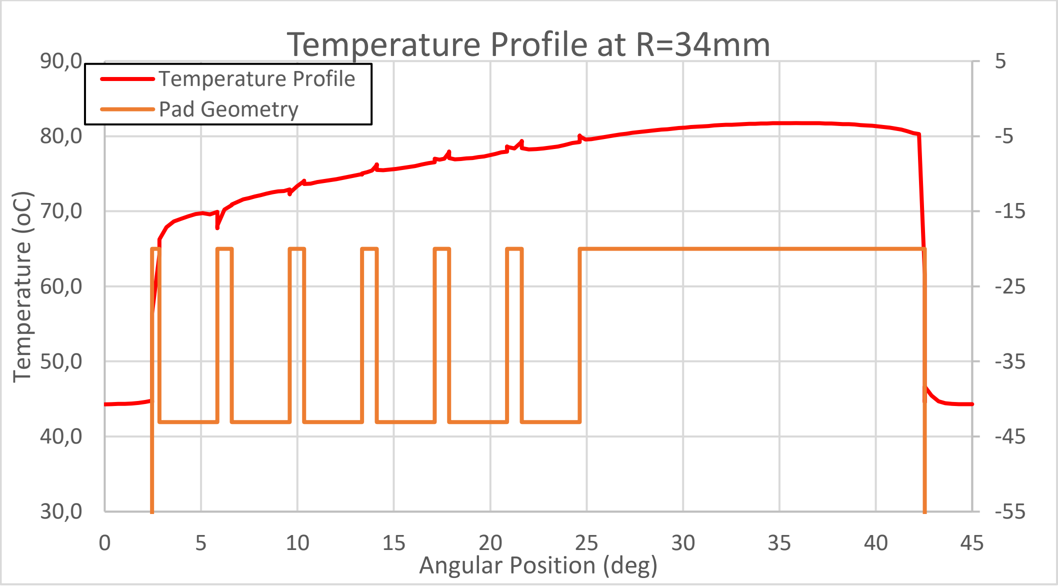

Figure 37 – Circumferential Temperature Profile at R=34mm

In the radial direction at an angle of 22.5° the pressure profile is presented on **Figure 38** and the temperature profile on **Figure 39**. The pressure distribution has the same behavior with the one in **Figure 8** as expected.

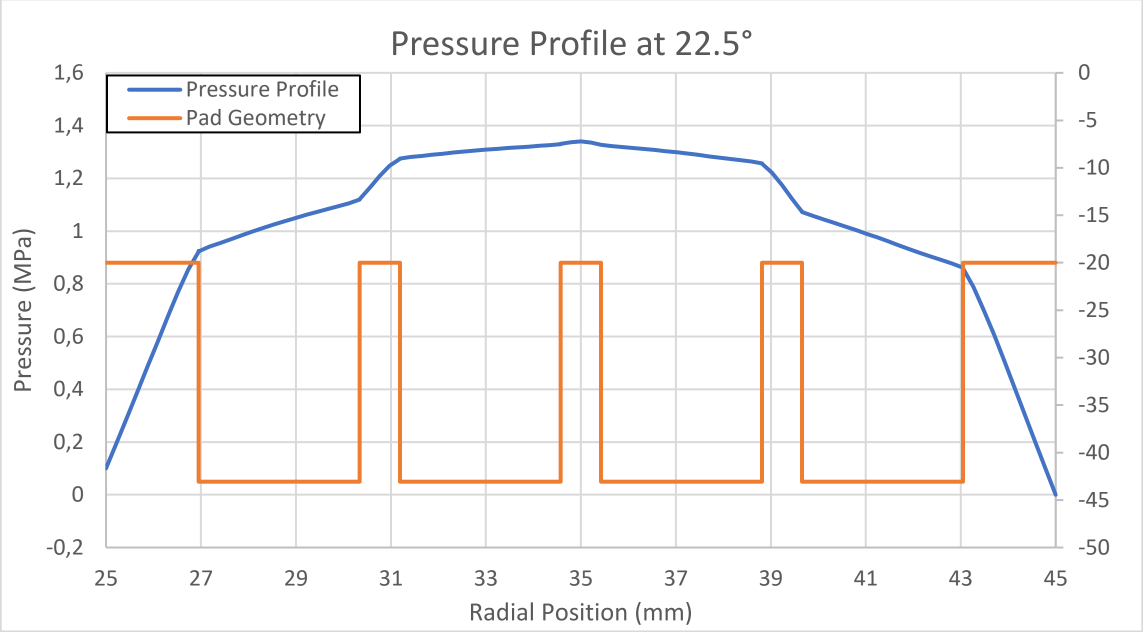

Figure 38 – Radial Pressure Profile at 22.5°

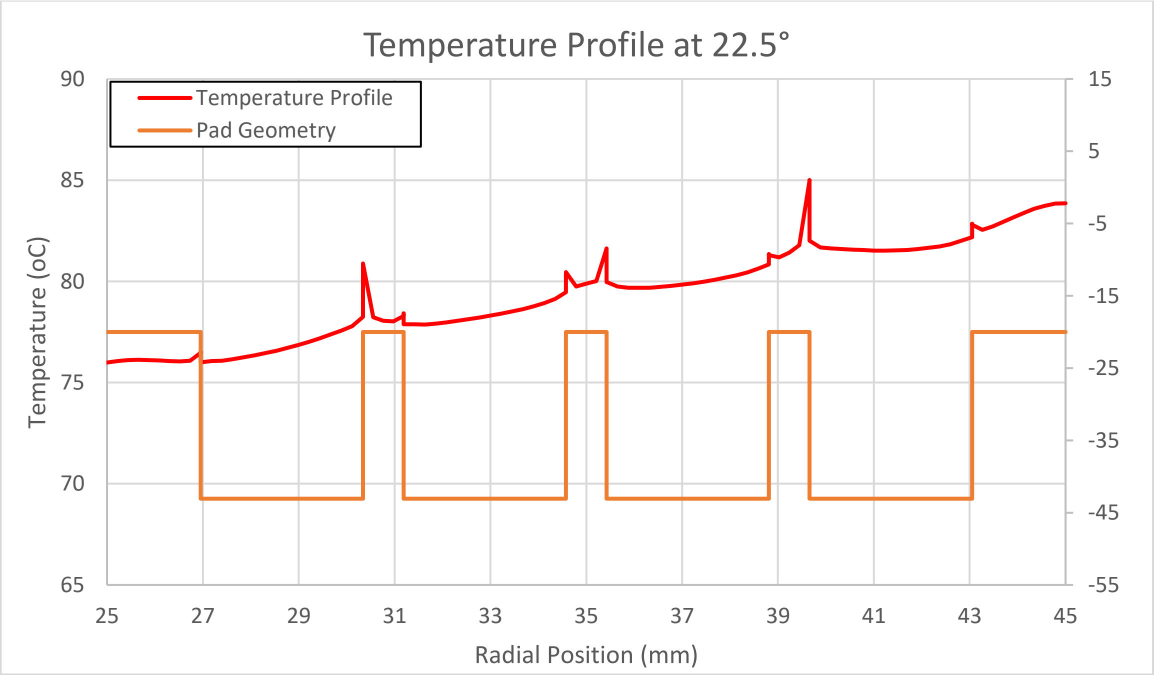

Figure 39 – Radial Temperature Profile at 22.5°

For various radii and angular positions, the pressure and temperature profiles have been calculated in order to create 3d-plots. The pressure distribution can be observed on **Figure 40** and **Figure 41** and the Temperature distribution on **Figure 42** and **Figure 43**.

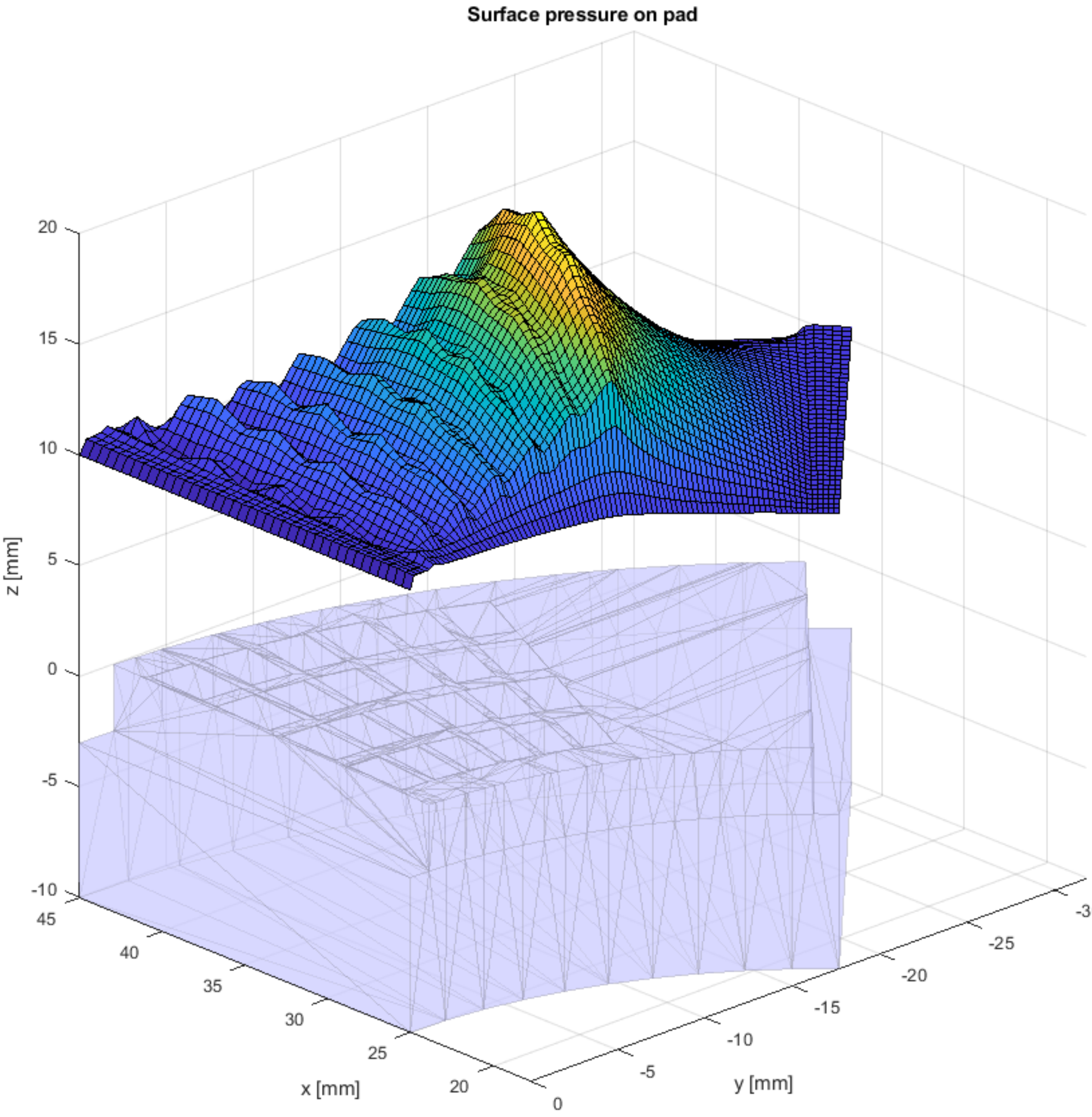

Figure 40 – 3D Pressure Field

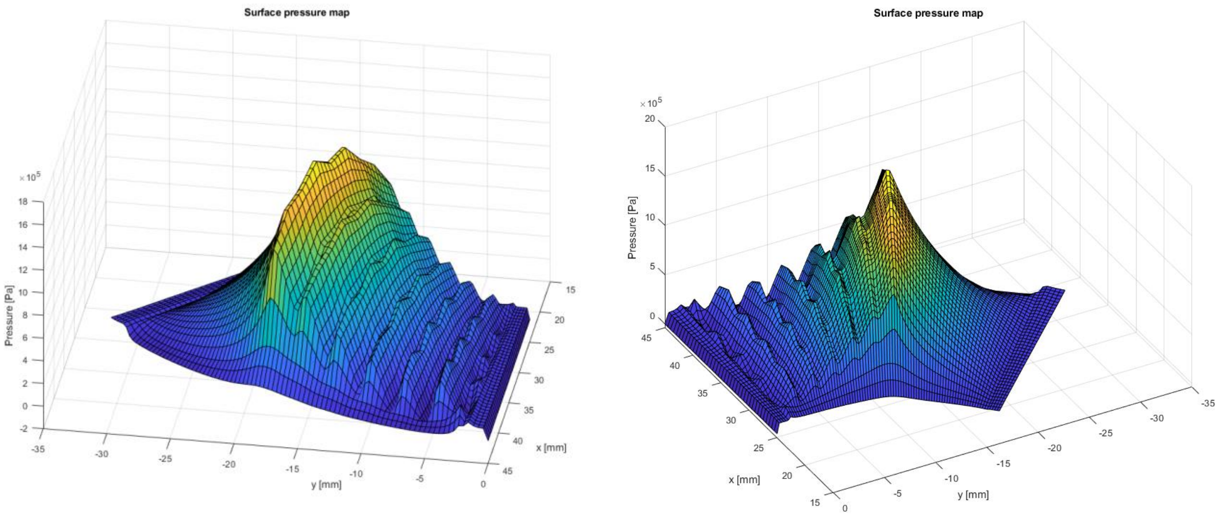

(a) **(b)**

Figure 41 – 3D Pressure Field a) Outer Radius b) Inner Radius

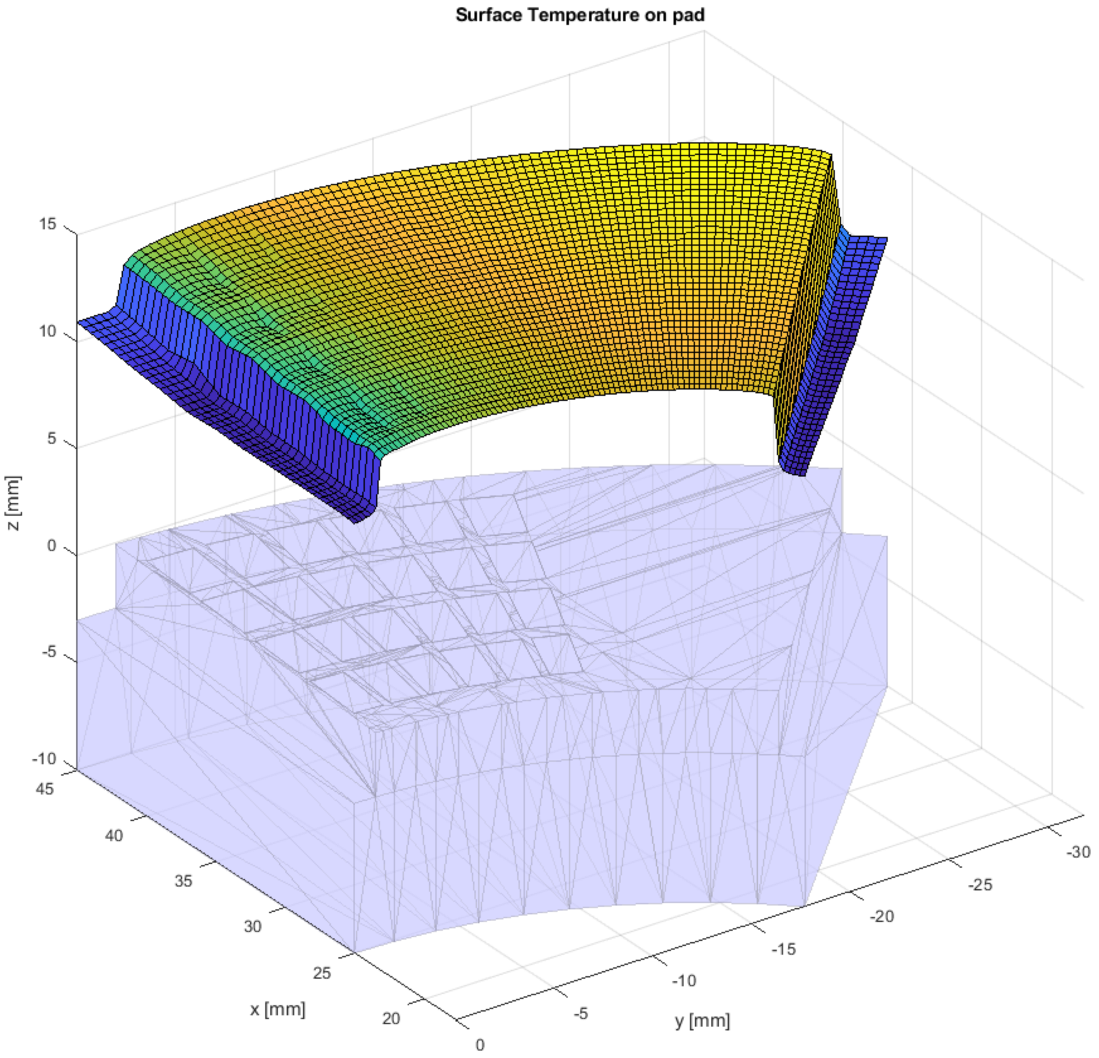

Figure 42 – 3D Temperature Field on Pad

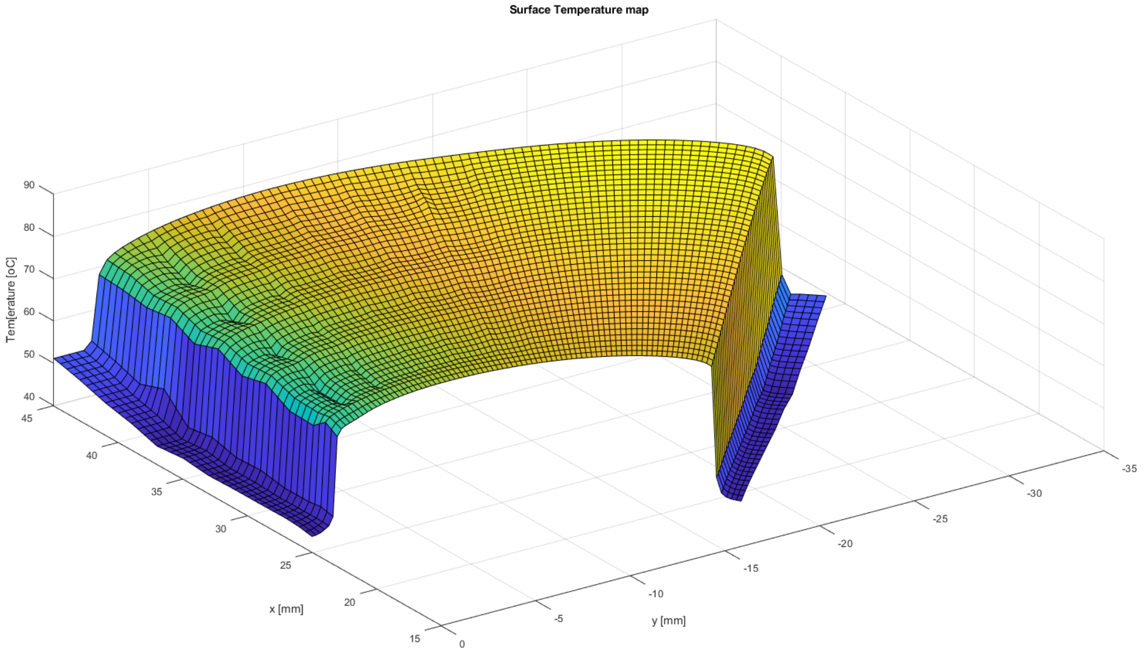

Figure 43 – 3D Temperature Field

2.4.6 Texture Geometry Parameters Sensitivity Analysis

In the vicinity of the optimal parameter set, a parametric analysis has been conducted, in order to identify the sensitivity of the design parameters. For the textured Length (L) and textured Width (B) limits of ±5% of the optimal value have been considered and for the textured Depth (TD) limits of ±3μm. As shown in **Figure 44** the local optimality is validated. Although for some parameter values the friction torque seems lower than the optimal, the LCC is also substantially decreased leading to a higher COF, observed in **Figure 46**.

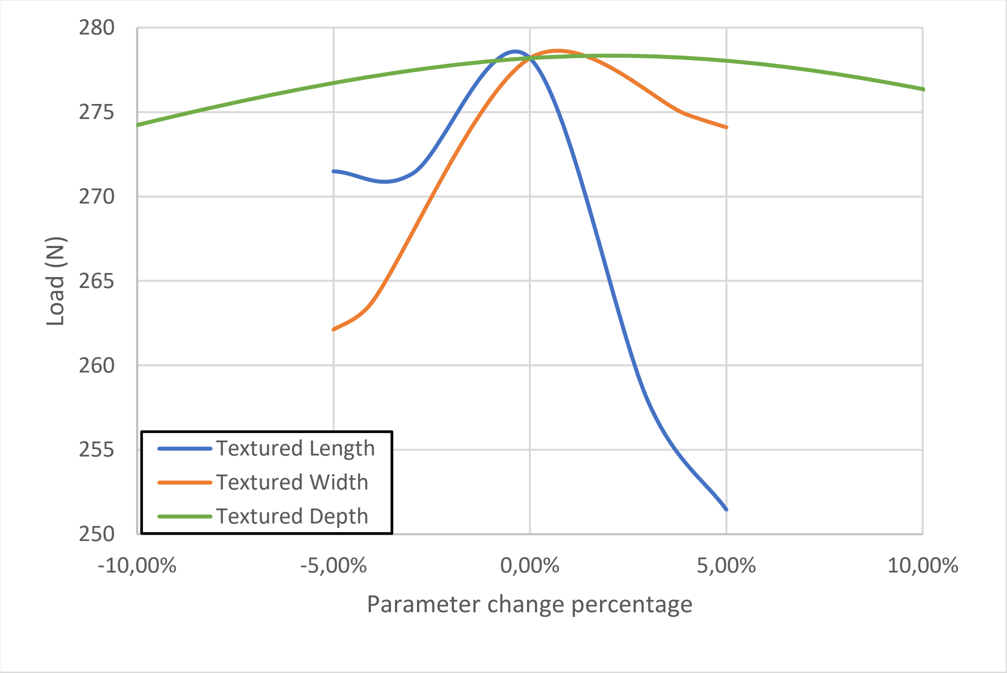

Figure 44 - THD Parametric analysis Load Carrying Capcity

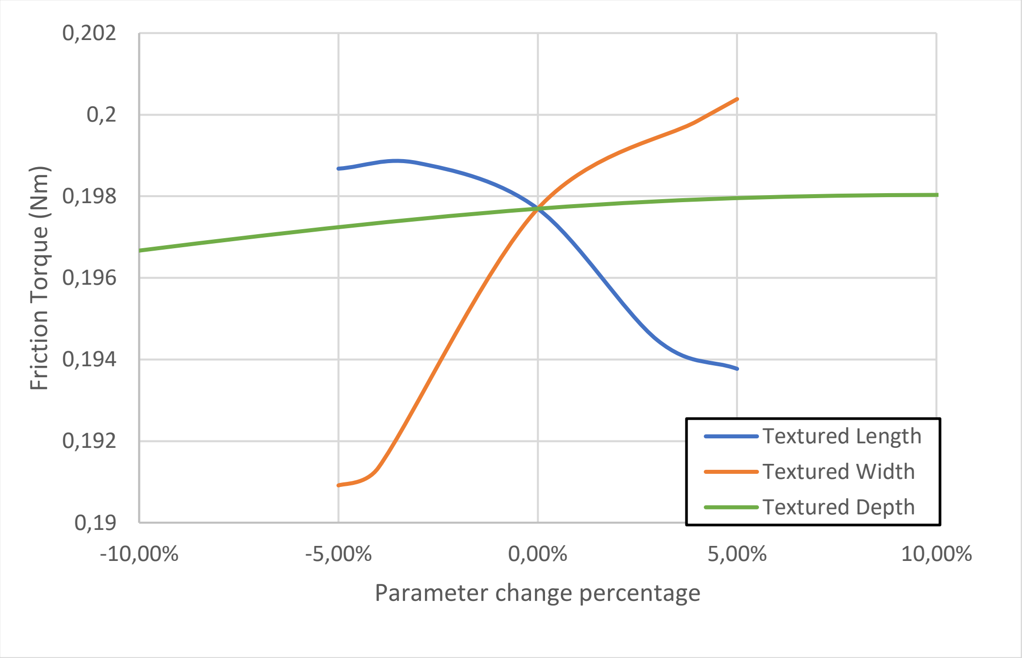

Figure 45 – THD Parametric analysis Friction torque

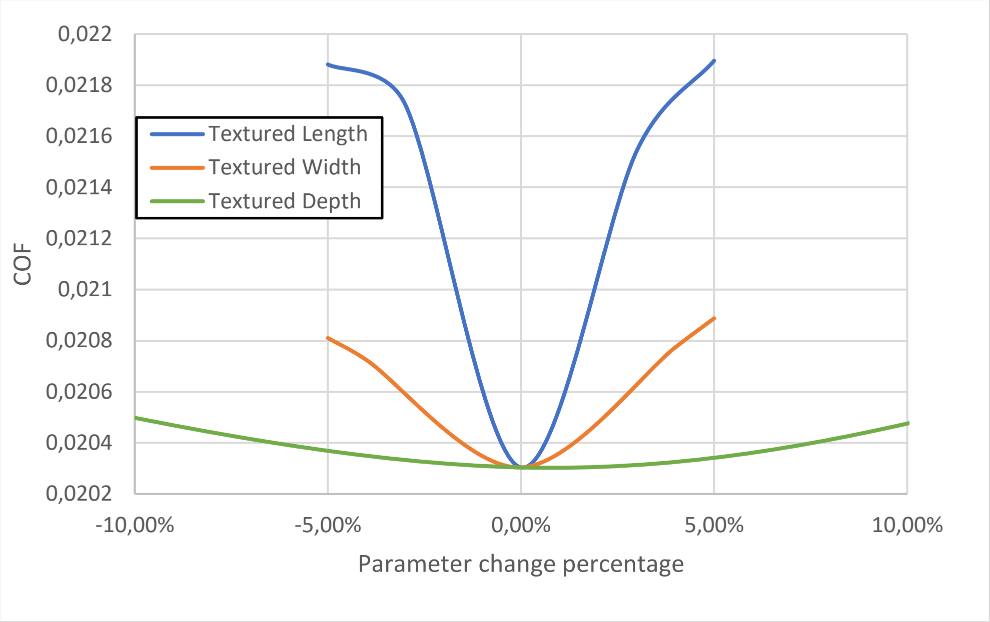

Figure 46 – THD Parametric analysis Friction coefficient

For values of ±2% of the optimal parameters, the air/oil volume fractions are presented, in order to understand the effect of the parameter change on cavitation.

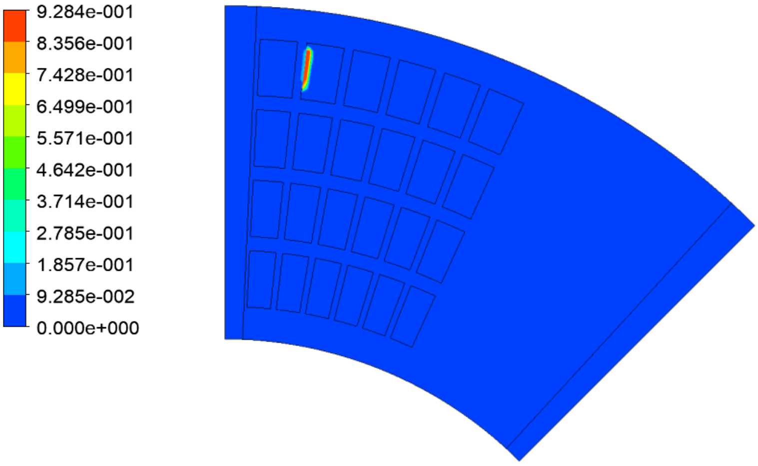

Figure 47 – Volume Fraction Optimal

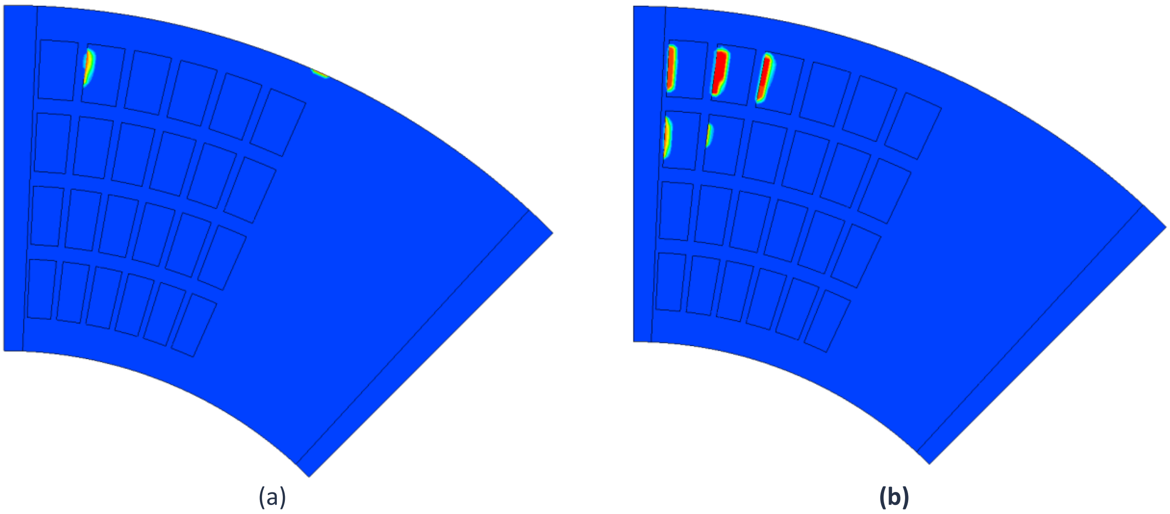

Figure 48 – Volume Fraction a) 2% Decreased Length b) 2% Increased Length

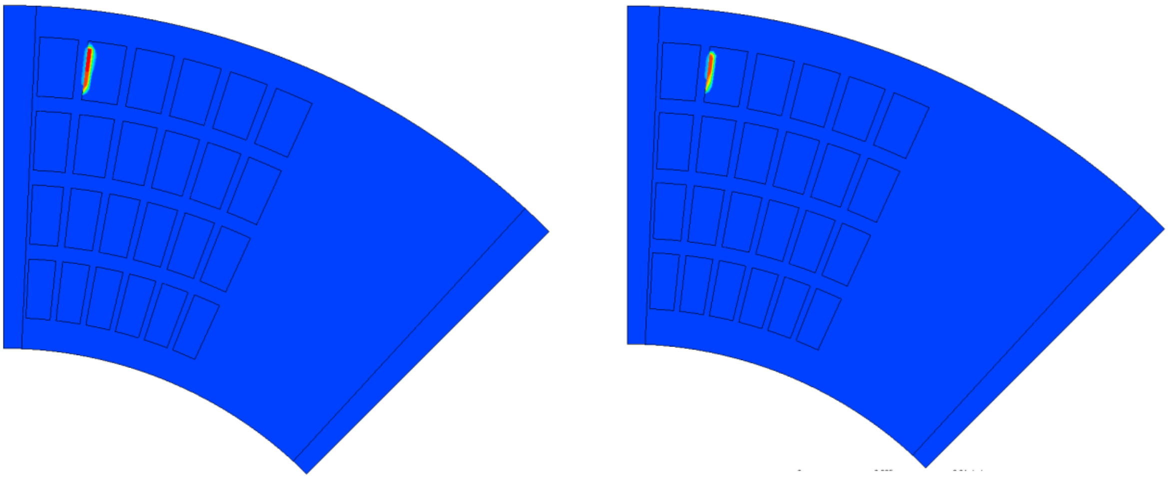

(a) **(b)**

Figure 49 – Volume Fraction a) 2% Decreased Width b) 2% Increased Width

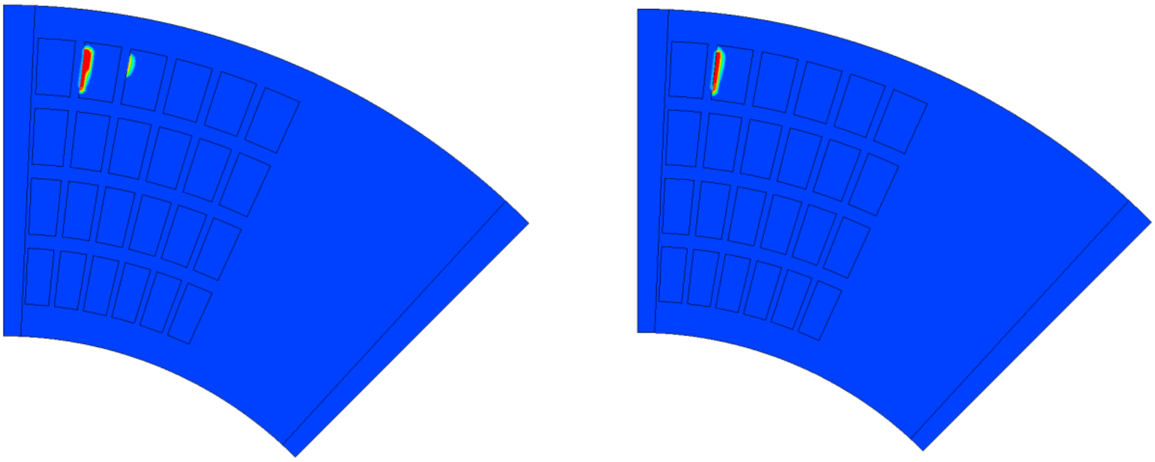

(a) **(b)**

Figure 50 – Volume Fraction a) 2% Decreased Texture Depth b) 2% Increased Texture Depth

For an increased value of texture length, the pressure drop into the dimples is significantly higher, thus cavitating regions are created in several areas. This affects the load carrying capacity and therefore the coefficient of friction. Moreover, from an operational point of view, these regions are likely to damage the surface of the pad and decrease its lifespan significantly. A comparison of the pressure profiles is presented on **Figure 51** at the midline and on **Figure 52** in the dimples area at a radius of 41mm. For the increased value of textured length, the overall pressure profile is lower and there are more areas where the pressure takes negative values and cavitation occurs, as seen on **Figure 53**.

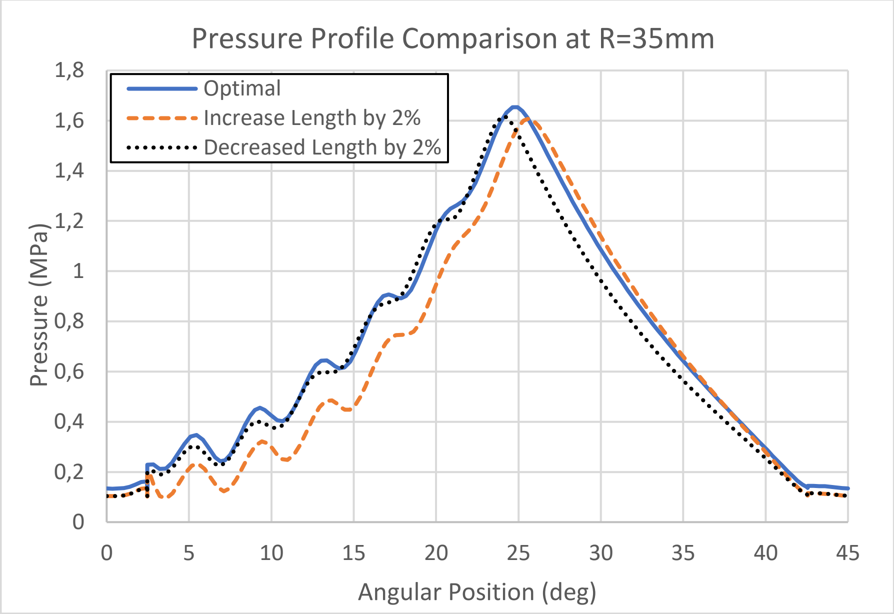

Figure 51 – Circumferential Pressure Profile on midline R=35mm

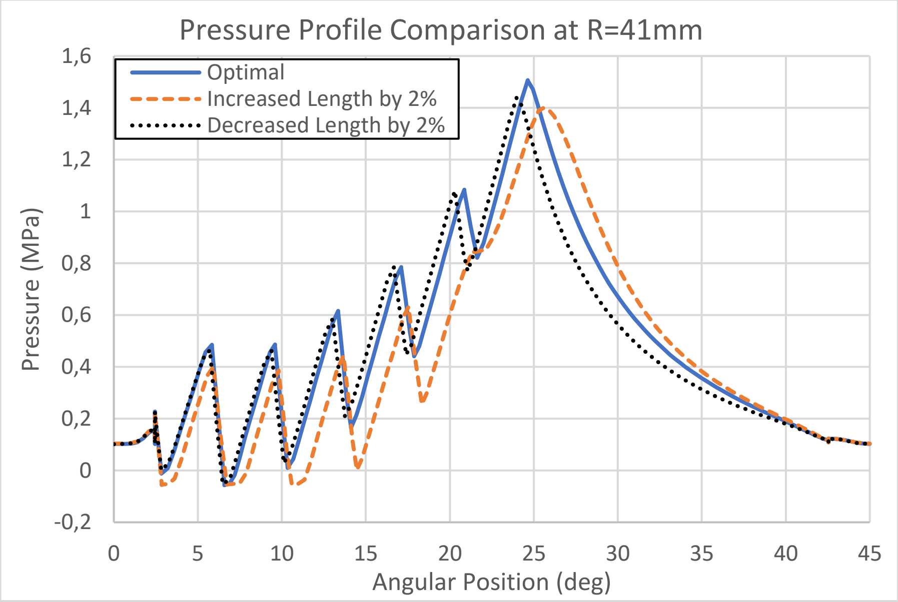

Figure 52 – Circumferential Pressure Profile at R=41mm

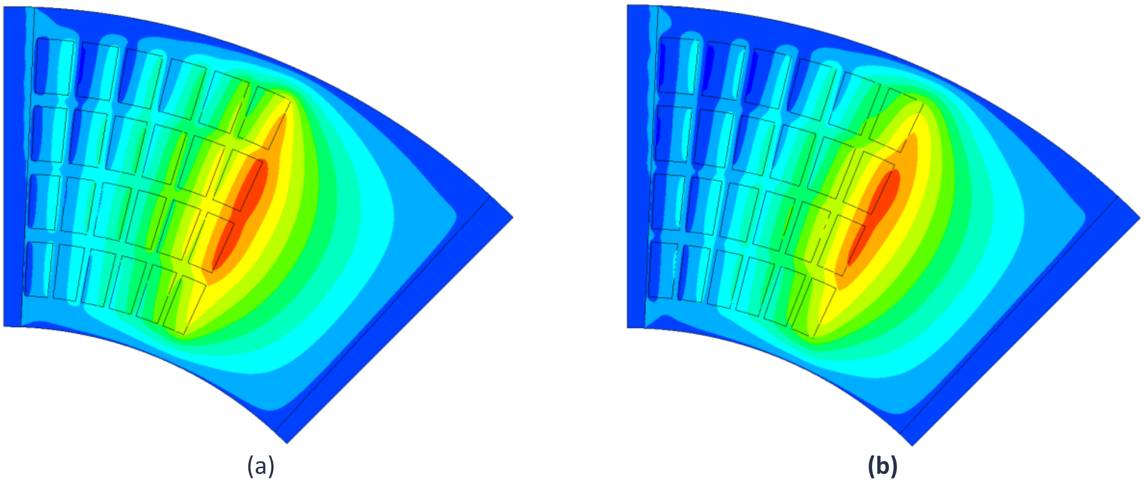

Figure 53 – Pressure Profile Comparison at Fluid-Pad interface a) optimal b) Increased L by 2%

2.4.7 Rotational Velocity Sensitivity Analysis

For a given minimum film thickness of 20μm a sensitivity analysis for the optimal geometry of the rotational velocity has been performed. In **Figure 54**, an increase of the load carrying capacity can be observed from 400 rpm to 4000 rpm and a decrease of the LCC from 4000 rpm to 10000 rpm. As the angular velocity increases the temperature increases significantly and the dynamic viscosity decreases leading to the decrease of the LCC. However, the friction torque has an asymptotic behavior. The temperature in **Figure 55** shows a linear increase with the angular velocity.

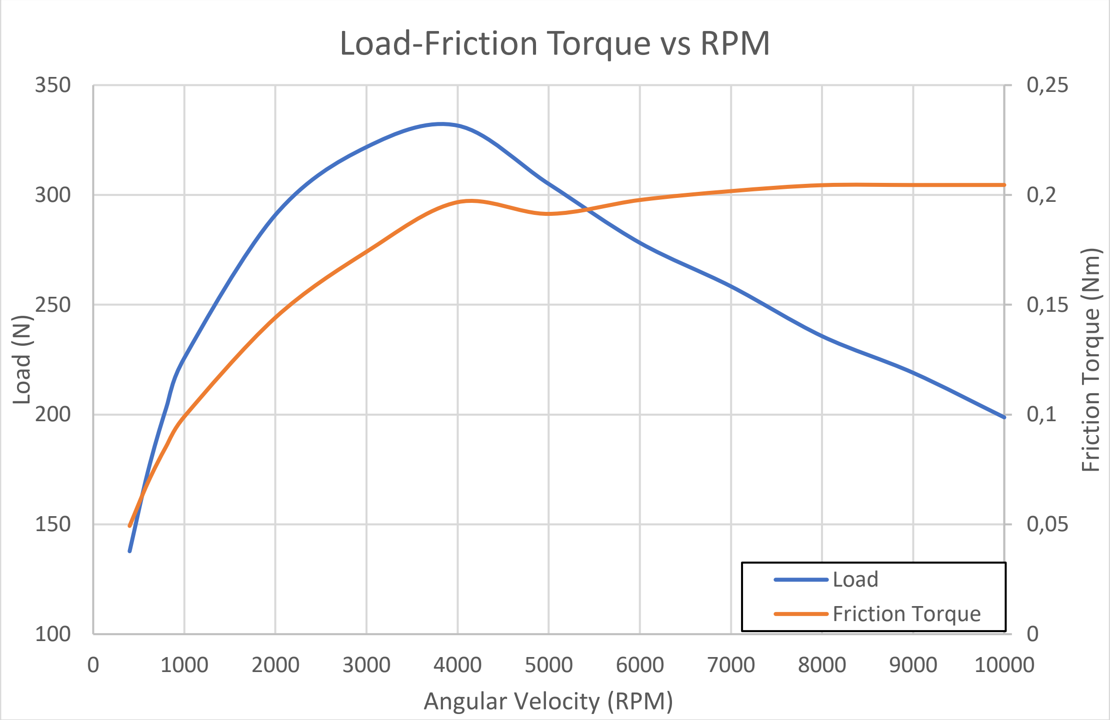

Figure 54 – Load-Friction Torque against Angular Velocity

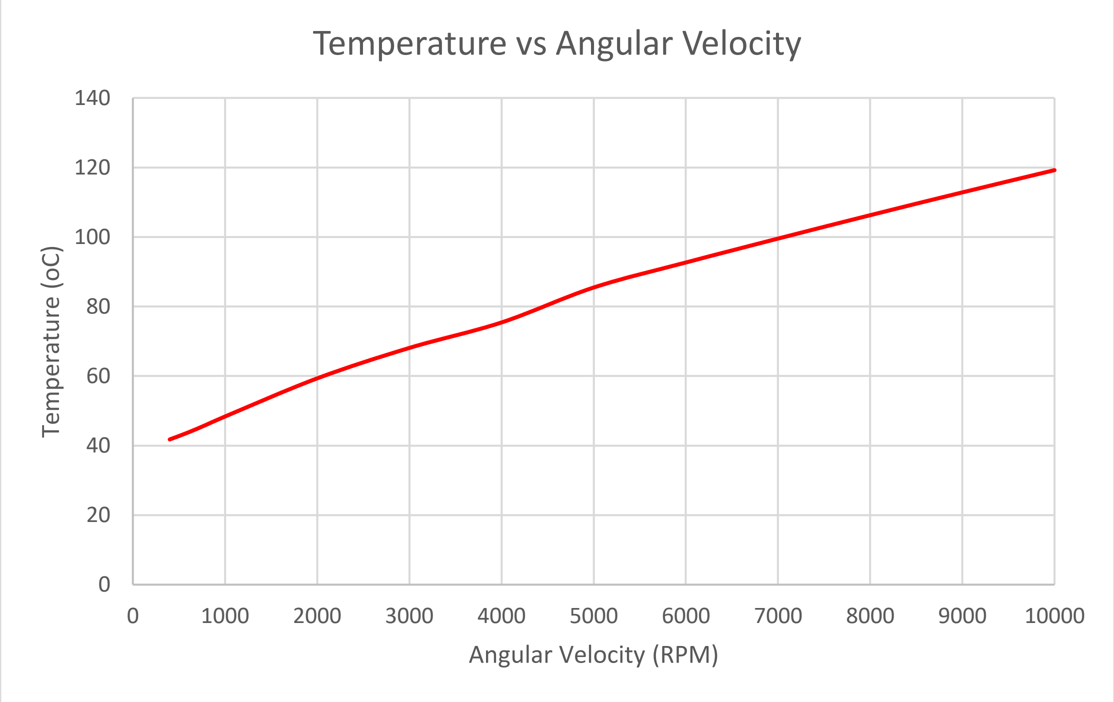

Figure 55 – Temperature against Angular Velocity

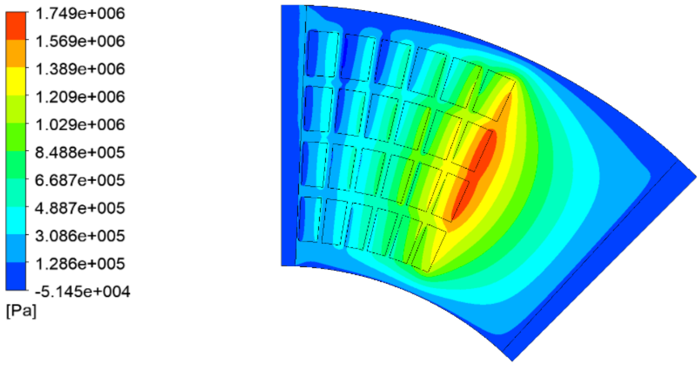

Figure 56 – Pressure Field Optimal @6000 rpm

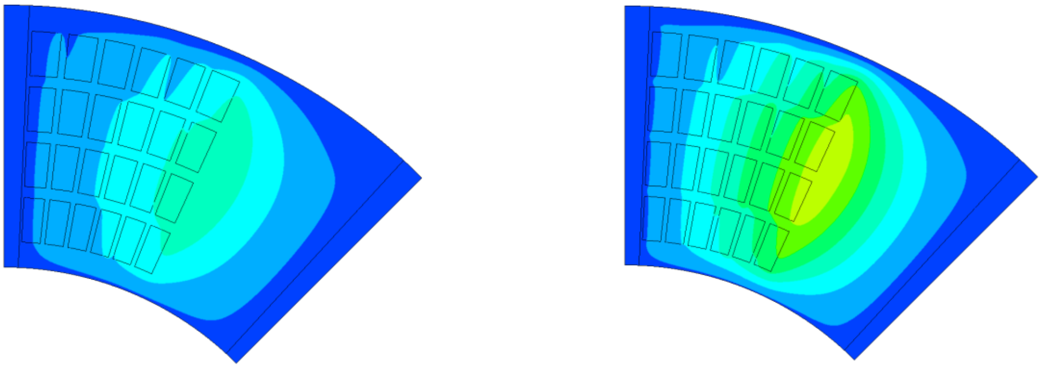

(a) **(b)**

Figure 57 – Pressure Field Optimal a) @400 rpm b) @1000 rpm

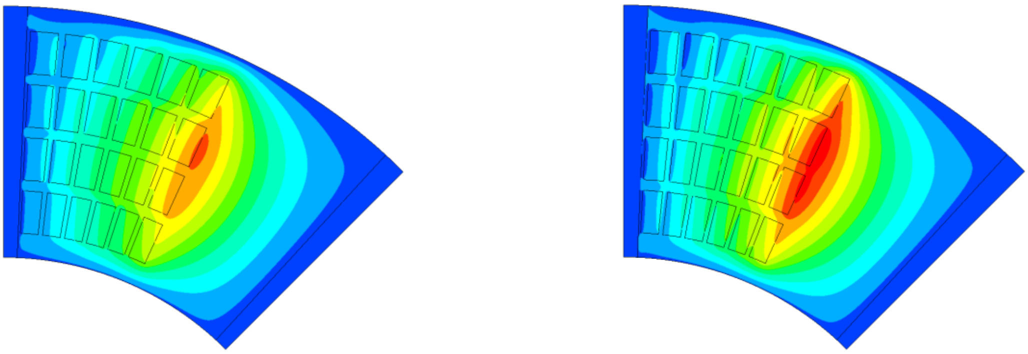

(a) **(b)**

Figure 58 – Pressure Field Optimal a) @2000 rpm b) @3000 rpm

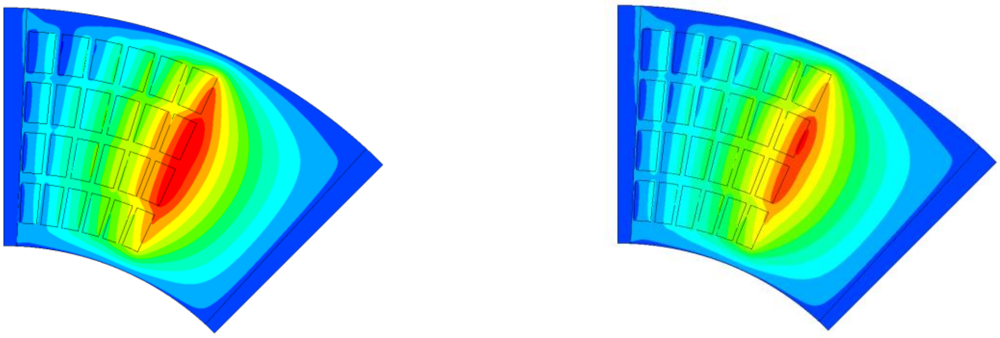

(a) **(b)**

Figure 59 – Pressure Field Optimal a) @4000 rpm b) @5000 rpm

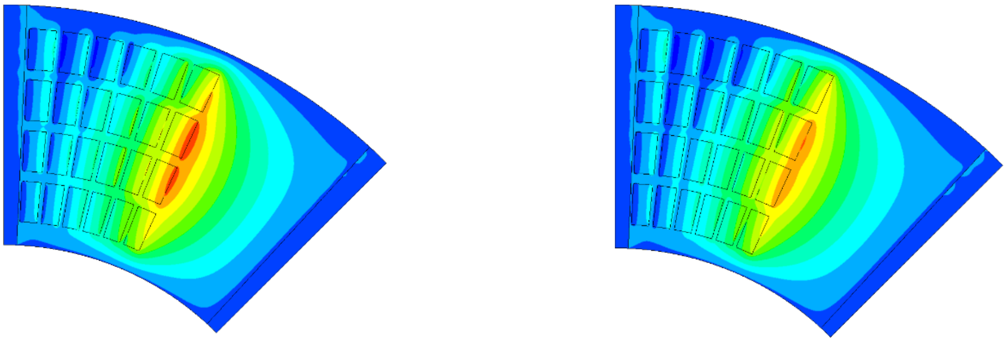

(a) **(b)**

Figure 60 – Pressure Field Optimal a) @7000 rpm b) @8000 rpm

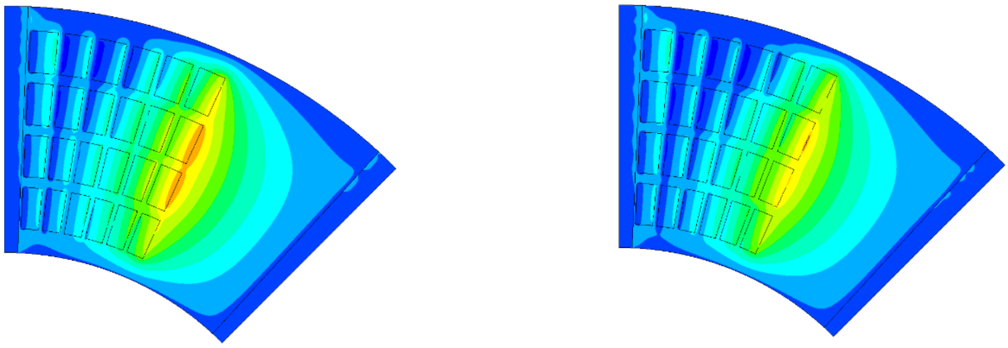

(a) **(b)**

Figure 61 – Pressure Field Optimal a) @9000 rpm b) @10000 rpm

The pressure gradually builds while the angular velocity increases to a certain point where it reaches a local optimum at around 4000 rpm, as seen in **Figure 57-59**. Then the effect of the temperature increase is significant for high rpm values, due to high shear stresses. The oil viscosity decreases dramatically, thus the pressure and the load carrying capacity decreases, **Figure 59-61**. Moreover, for high angular velocities, the pressure drops on the outer radius of the leading edge, inside the textures and cavitation occurs. The volume fraction diagrams are presented below.

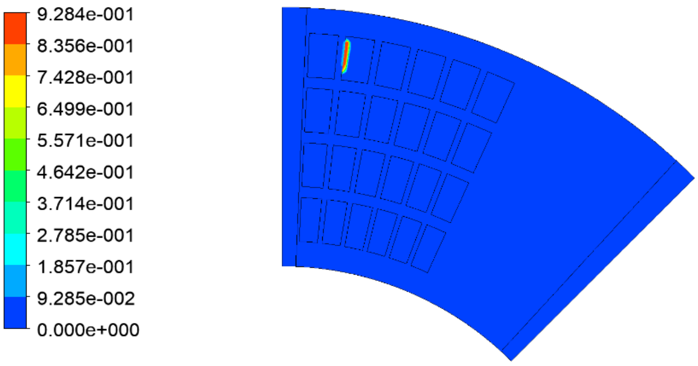

Figure 62 – Volume Fraction Field at Fluid-Pad Optimal @6000 rpm

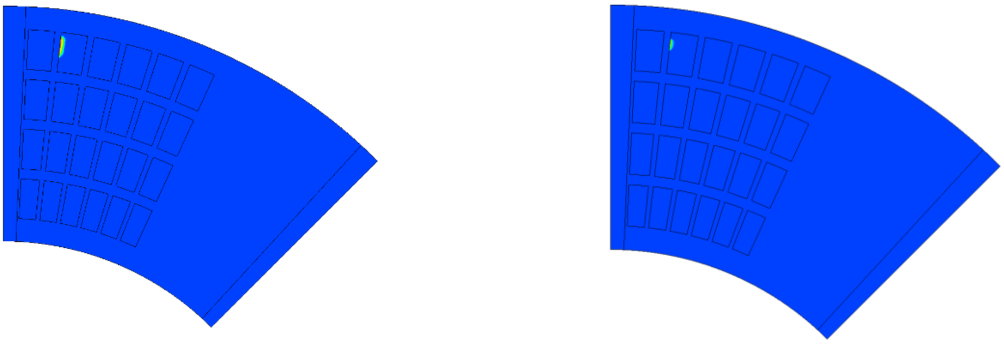

(a) **(b)**

Figure 63 – Volume Fraction Field at Fluid-Pad Optimal a) @4000 rpm b) @5000 rpm

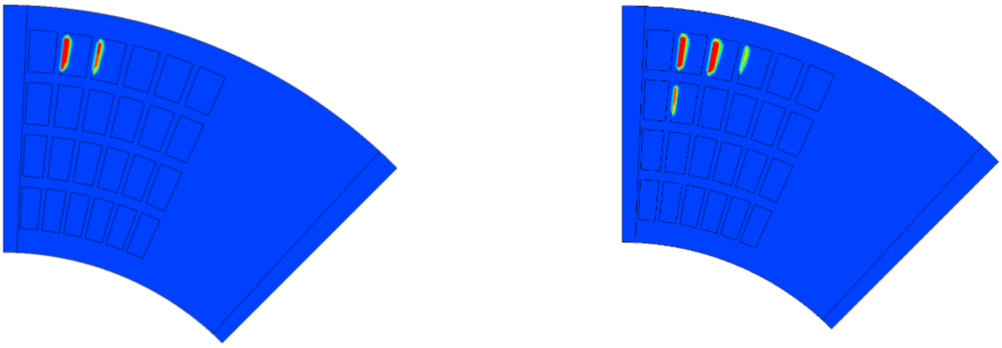

(a) **(b)**

Figure 64 – Volume Fraction Field at Fluid-Pad Optimal a) @7000 rpm b) @8000 rpm

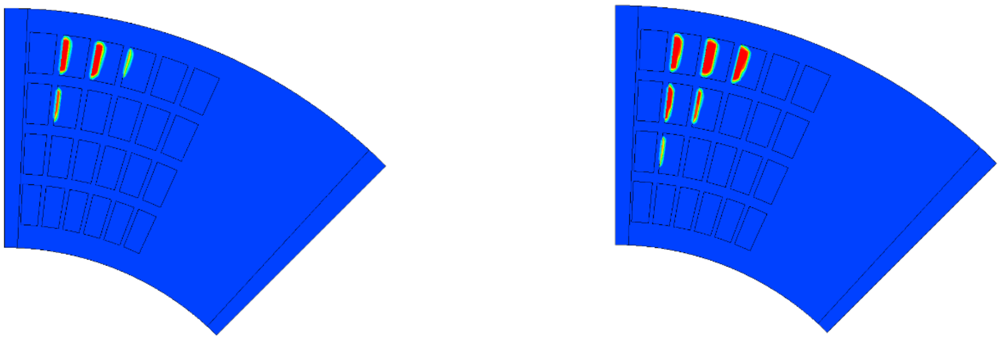

(a) **(b)**

Figure 65 – Volume Fraction Field at Fluid-Pad Optimal a) @9000 rpm b) @10000 rpm

Cavitation does not occur from 400 to 4000 rpm. The pressure drop increases gradually as the angular velocity increases leading to the formation of more cavitating regions inside the textures, as observed in **Figure 63-65**. The temperature at the fluid-pad interface, from 400 to 3000 rpm has low values. From 4000 rpm the temperature increase becomes significant as seen in **Figure 66**. Especially for high rpm values the shear stresses of the fluid are severe, therefore the fluid temperatures increase dramatically, as seen on **Figure 68** and **Figure 69**. This has a huge impact on the performance of the bearing, especially on the load carrying capacity and the thermal deformation of the pad.

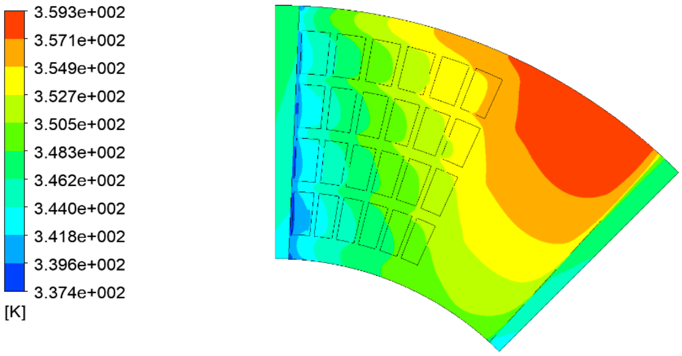

Figure 66 – Temperature at Fluid-Pad Optimal @6000 rpm

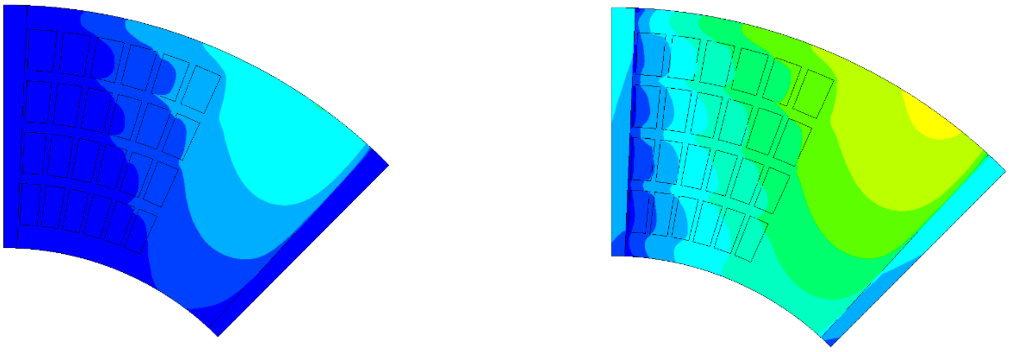

(a) **(b)**

Figure 67 – Temperature at Fluid-Pad Optimal a) @4000 rpm b) @5000 rpm

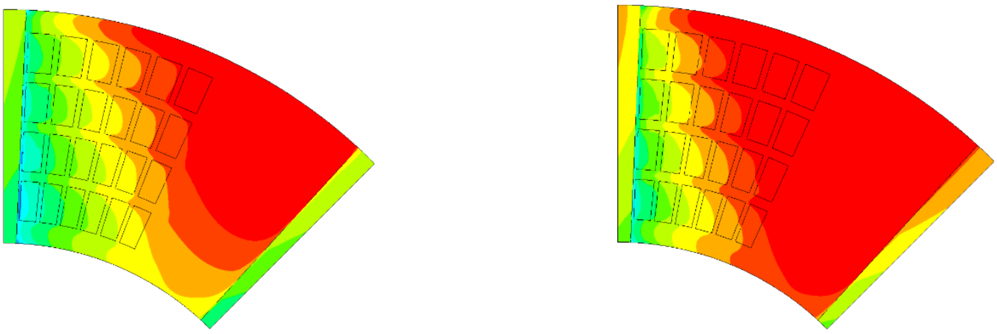

(a) **(b)**

Figure 68 – Temperature at Fluid-Pad Optimal a) @7000 rpm b) @8000 rpm

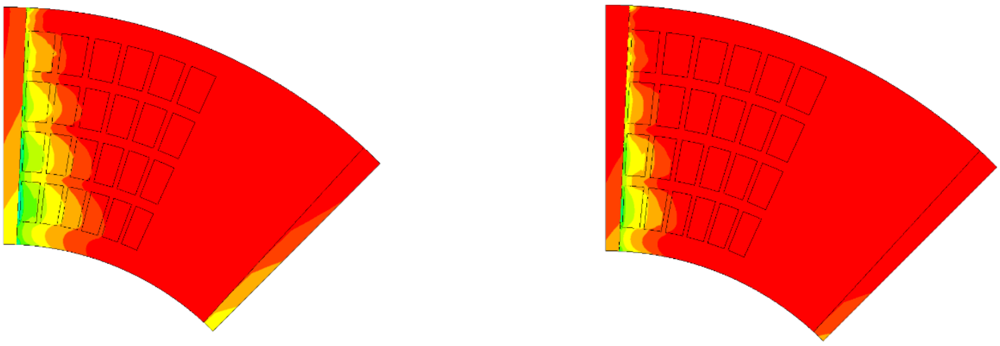

(a) **(b)**

Figure 69 – Temperature at Fluid-Pad Optimal a) @9000 rpm b) @10000 rpm

2.4.8 Minimum Film Thickness Sensitivity Analysis

For a given angular velocity of 6000 rpm, a sensitivity analysis of the minimum film thickness has been performed in order to assess the load carrying capacity of the pad. It is well known, that the load carrying capacity is proportional to the decrease of the minimum film thickness. Moreover, the decrease of the film thickness leads to the increase of the shear stresses in the fluid, thus the overall operation temperature increases. On **Figure 70**, the variation of the LCC and the friction torque against the minimum film thickness is presented. On **Figure 71** the behavior of the maximum temperature of the fluid is shown.

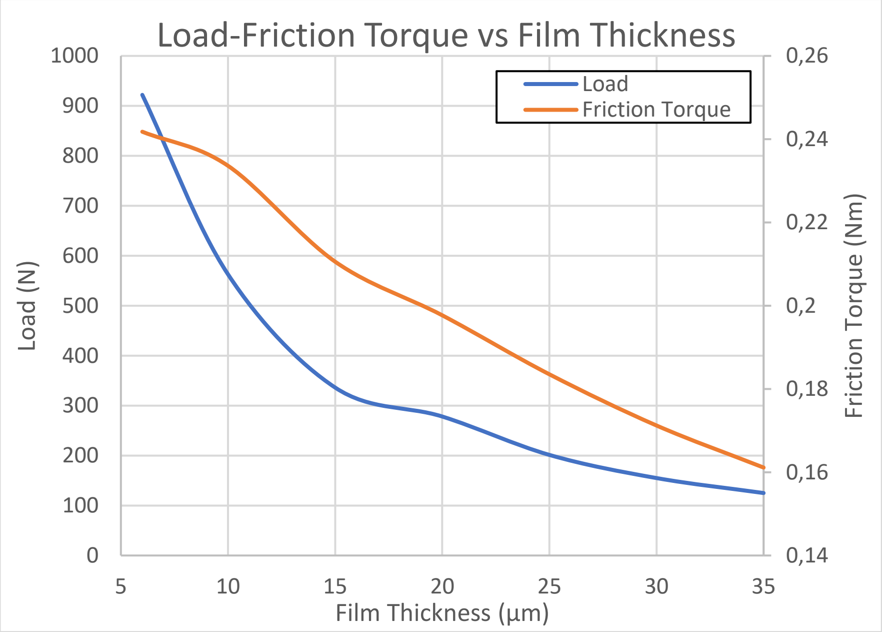

Figure 70 – Load Carrying Capacity and Friction Torque against Min. Film Thickness

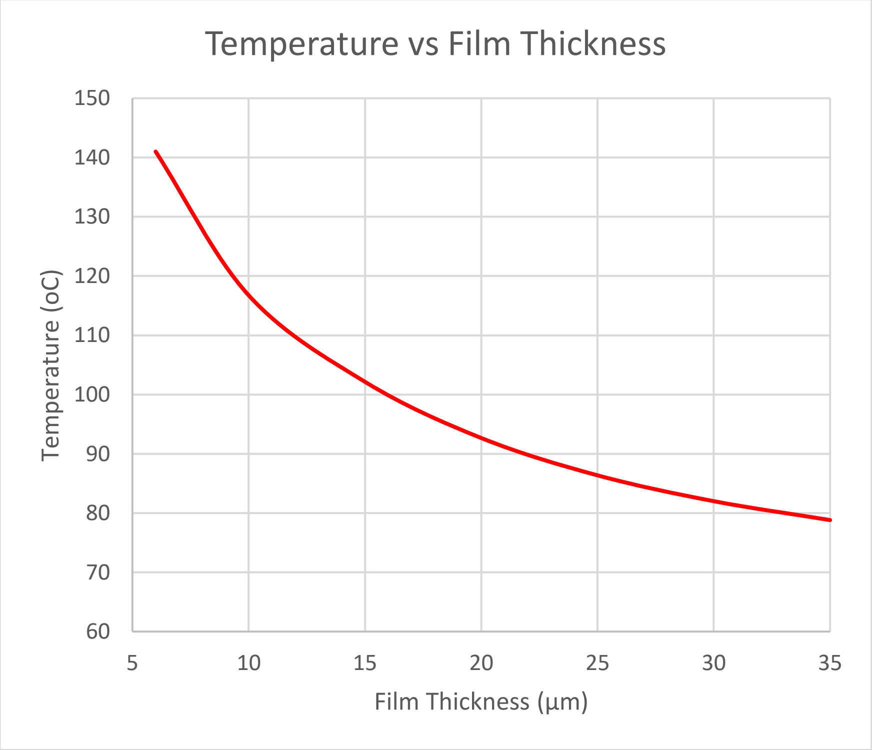

Figure 71 – Maximum Temperature of Fluid against Min. Film Thickness

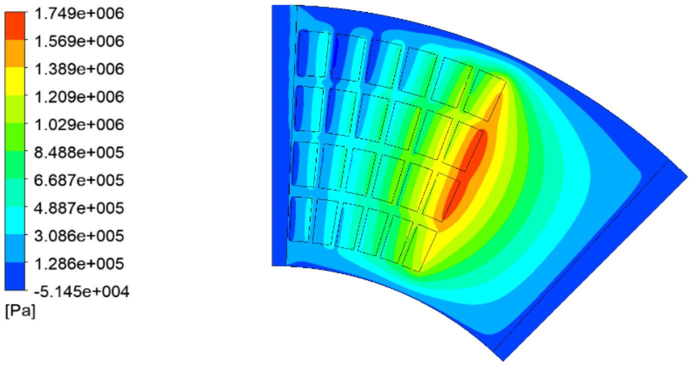

Figure 72 – Pressure Field at Fluid Pad Interface Optimal @20 μm

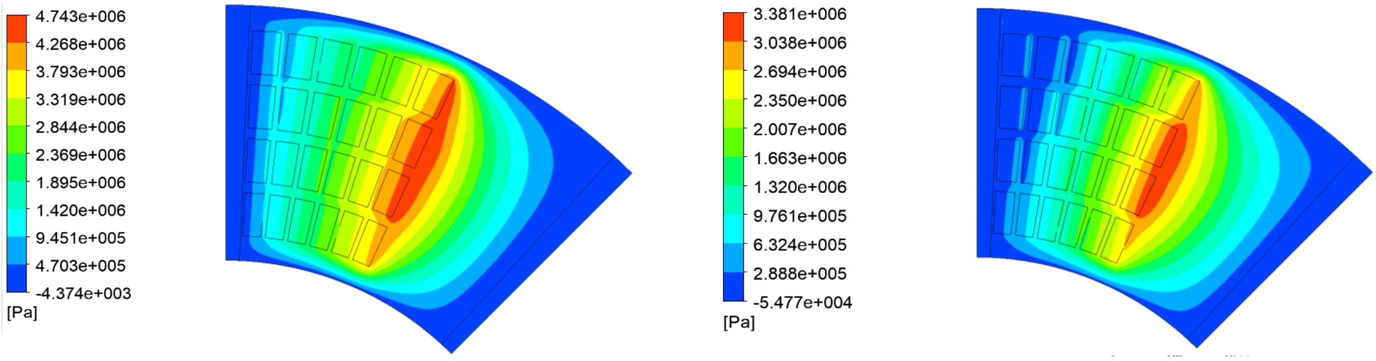

(a) **(b)**

Figure 73 – Pressure Field at Fluid Pad Interface Optimal a) @6 μm b) @10 μm

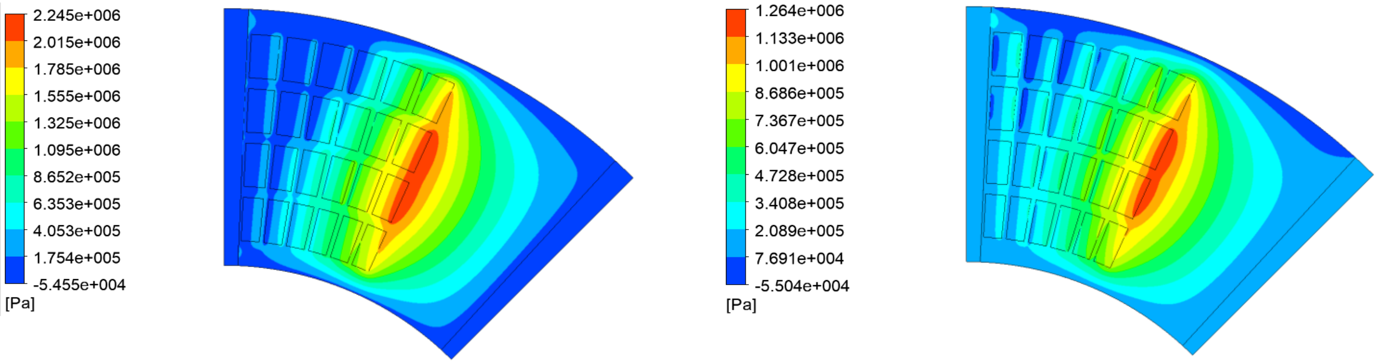

(a) **(b)**

Figure 74 – Pressure Field at Fluid Pad Interface Optimal a) @15 μm b) @25 μm

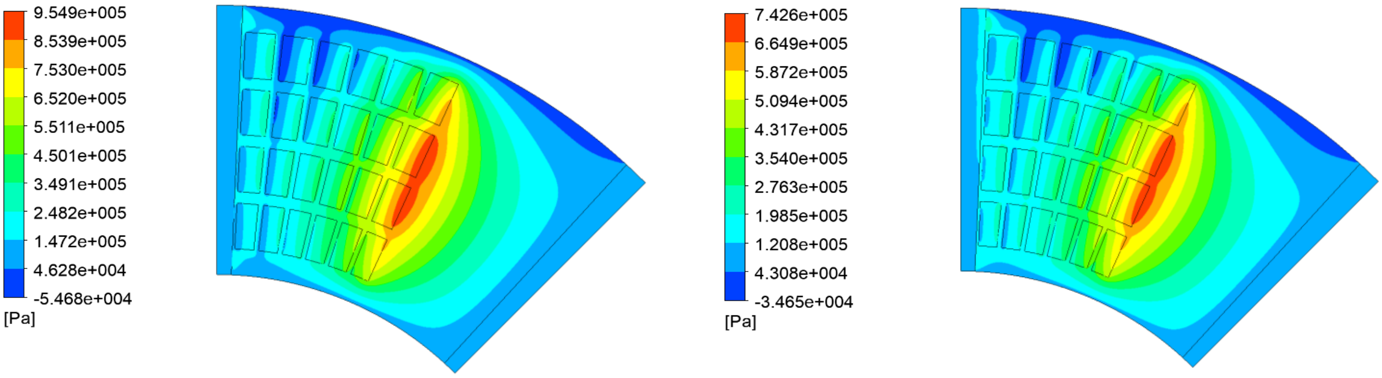

(a) **(b)**

Figure 75 – Pressure Field at Fluid Pad Interface Optimal a) @30 μm b) @35 μm

The pressure increases with the decrease of the minimum film thickness as seen on the upper Figures. The alteration of the film thickness affects both the form of the pressure profile and the maximum values of the pressure, as seen from the color bars.

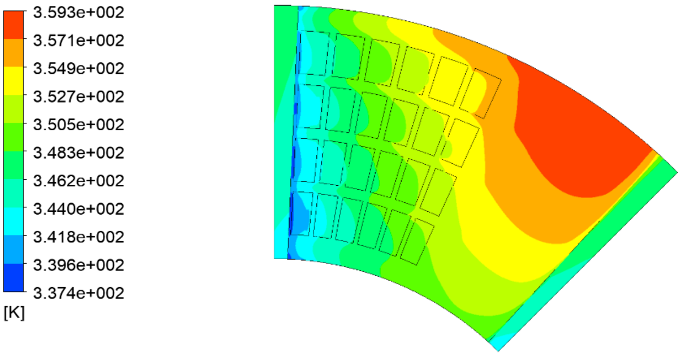

Figure 76 – Temperature Field at Fluid Pad Interface Optimal @20 μm

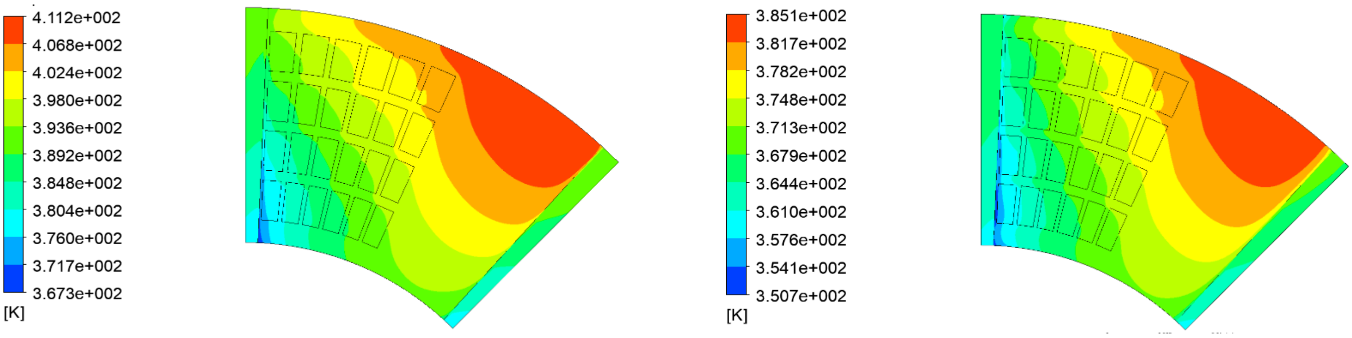

(a) **(b)**

Figure 77 – Temperature Field at Fluid Pad Interface Optimal a) @6 μm b) @10 μm

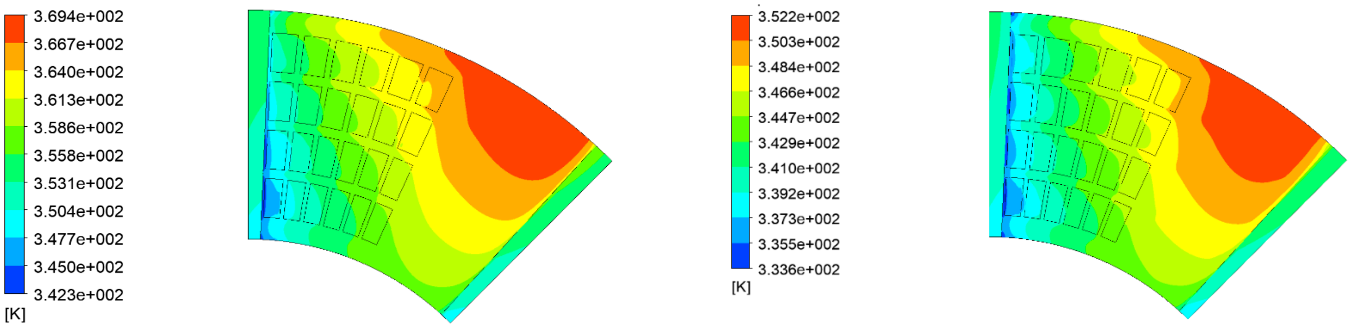

(a) **(b)**

Figure 78 – Temperature Field at Fluid Pad Interface Optimal a) @15 μm b) @25 μm

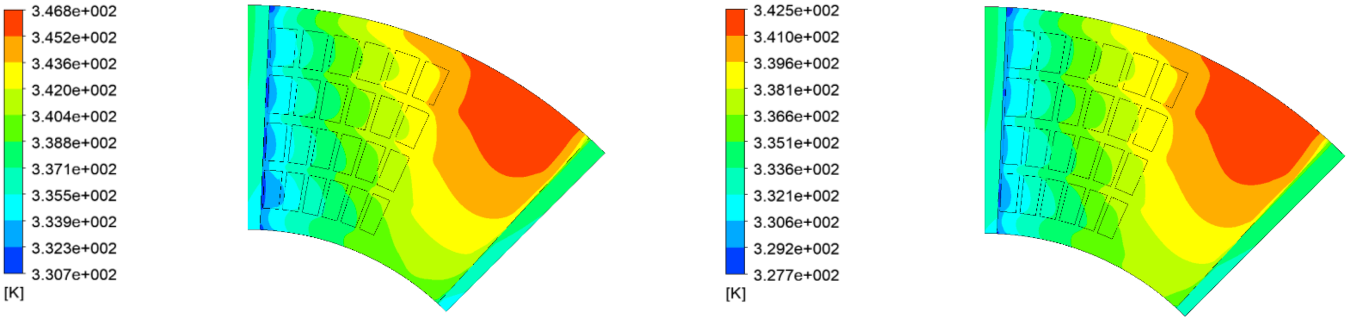

(a) **(b)**

Figure 79 – Temperature Field at Fluid Pad Interface Optimal a) @30 μm b) @35 μm

As the minimum film thickness decreases, the shear stresses increase and therefore the temperature increases. The profile of the temperature is also altered according to **Figure 76-79**.

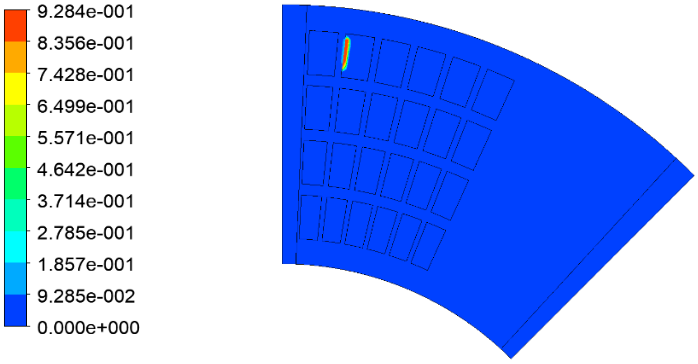

Figure 80 – Volume Fraction Field at Fluid Pad Interface Optimal @20 μm

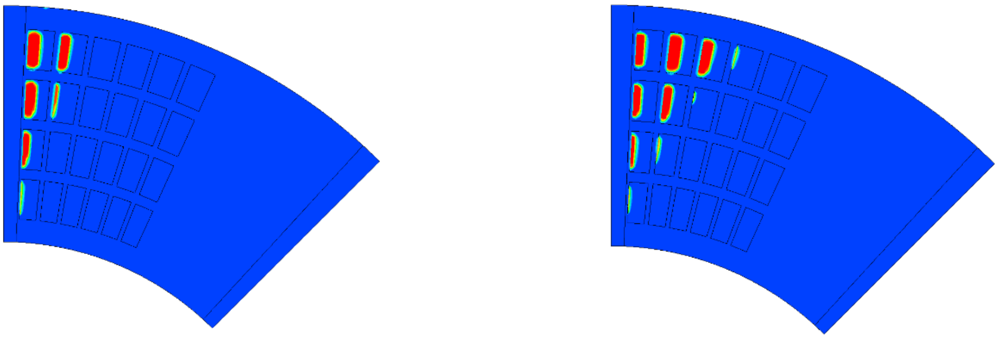

(a) **(b)**

Figure 81 – Volume Fraction Field at Fluid Pad Interface Optimal a) @10 μm b) @15 μm

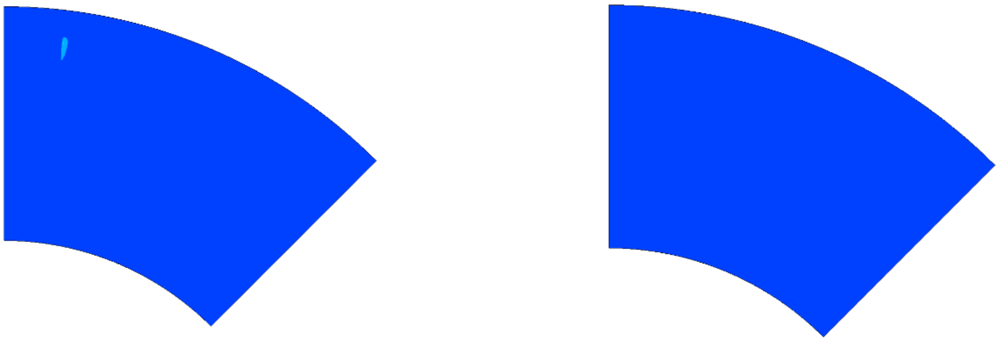

(a) **(b)**

Figure 82 – Volume Fraction Field at Fluid Pad Interface Optimal a) @25 μm b) @30 μm

The pressure drop into the textured surface area becomes significant from 10μm until 25μm. This the area where cavitation occurs. For values above 25μm cavitation does not occur.

2.5 TEHD modelling procedure

The ThermoElastoHydroDynamic (TEHD) model has been generated utilising a commercial code (Ansys CFX and Ansys Mechanical). The 2-way FSI modelling approach has been utilised for the fluid-pad interface. On the domain interface of the fluid and pad, the CFX and FE solvers exchange data for the continuity of the temperature and pressure on both domains. Temperature and pressure field data are transferred from the CFD to the FE solver, and mesh displacement and heat flux of the interface from the FE to the CFD solver. The bearing pad geometry can deform due to (a) the temperature gradient, and (b) pressure generated within the thin lubricant film.

The numerical procedure of the TEHD model comprises the following steps:

- First, the FE solver calculates the initial thermal expansion of the pad geometry, from an initial temperature of 20 °C to the ambient temperature of 40 °C and transfers the displaced geometry to the CFD solver.
- The Navier-Stokes and the energy equations are solved in the lubricant and rotor domains, respectively, calculating the corresponding flow and temperature distributions.
- The pressure and heat flux at the fluid/pad interface are transferred to the FE solver, which calculates the thermal and mechanical deformations of the pad.
- The displaced geometry of the pad is transferred to the CFD solver, and an updated lubricant geometry is computed.
- This described procedure iterates until final convergence, which is reached if the difference of the geometry change (measured in terms of maximum nodal mesh displacement between two consecutive steps) is less than $3x10^{-8}$.
- The performance indices of the bearing are calculated for the final converged film geometry.

The above procedure is followed for different values of the initial distance between the rotor and the pad. The computational calculation algorithm is depicted in **Figure 83**.

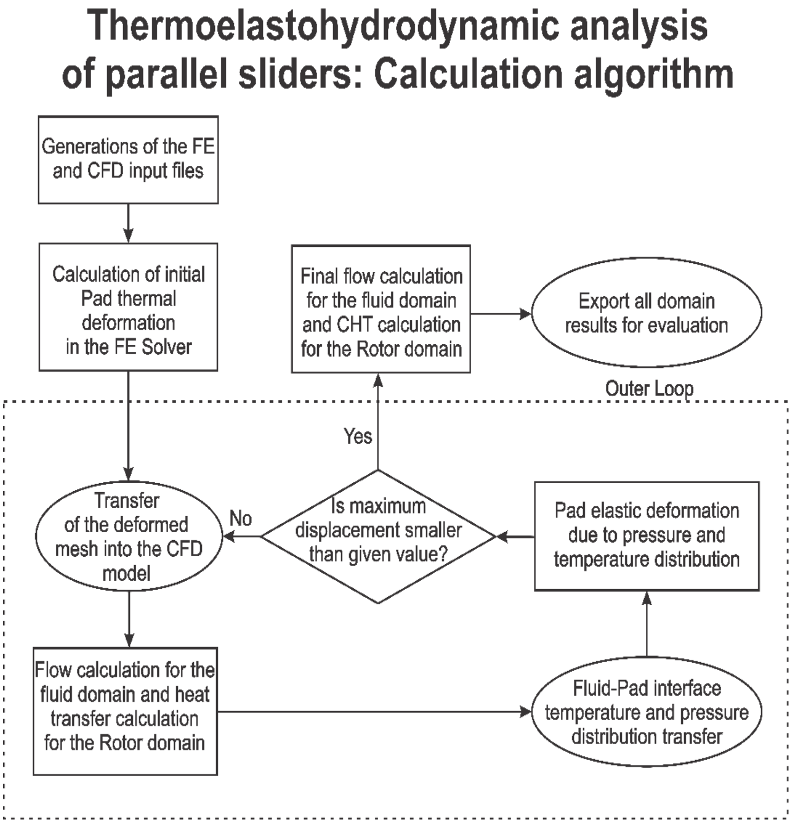

Figure 83 - ThermoElastoHydroDynamic analysis of parallel thrust bearings: Calculation algorithm

2.5.1 Governing equations

In the present models, the conservation equations are solved with the CFD code ANSYS CFX and the FE code ANSYS MECHANICAL, for steady, incompressible flow, with no gravitational forces and cavitation modeling. The equations are presented below:

Mass conservation equation: $\nabla \cdot V = 0$ [18]
Momentum equations: $\rho(V\Delta)V = -\nabla p + \nabla \cdot (\mu \cdot \nabla V)$ [19]
Energy equation, fluid domain: $\rho \cdot c_{pf} \cdot v \cdot \nabla T = \nabla\left(\lambda_f \cdot \nabla T\right) + \mu\Phi$ [20]
Energy equation, solid domains: $\nabla(\lambda_s \cdot \nabla T) = 0$ [21]

Where V is the velocity vector (m/s), p the static pressure (Pa), T the temperature (K), τ the viscous stress tensor, ρ the oil density (kg/m^3), μ the oil dynamic viscosity (kg/m.s), c_{pf} the oil specific heat capacity (J/kg.K), λ_f the oil thermal conductivity (W/m.K), λ_s the rotor thermal conductivity (W/m.K). The dissipation term Φ describes the heat generated by internal fluid friction.

The pad undergoes elastic deformation due to (a) pressure distribution on the fluid/pad interface, and (b) the thermal expansion of the solid. The stress is related to strain by:

$\{\sigma\}=[D][\{\varepsilon^{el}\}$ [25]

where $\{\varepsilon^{el}\}=\{\varepsilon\}-\{\varepsilon^{th}\}$, and $\{\varepsilon^{th}\}= \Delta T[\alpha^{se}\ \alpha^{se}\ \alpha^{se}\ 0\ 0\ 0]^T$ [26]

where α^{se} is the coefficient of thermal expansion.

2.6 TEHD model of Rectangular Dimples

The meshing and boundary conditions used for the more complicated TEHD analysis is the same as the THD model in order to be able to compare these two. In the case of the TEHD an initial minimum film thickness is selected which changes proportionally to the alteration of the fluid-pad geometry. The final minimum film thickness is measured according to the minimum distance of the stator from the rotor. In order to compare the THD model and the TEHD model, a reference minimum film thickness was selected at 20 µm. For the present study through trial and error, an initial 29.7 µm film thickness was selected.

2.6.1 Results

The optimal THD design has been re-evaluated with a TEHD based analysis. The results shown on **Figure 84a** indicate a substantial alteration of the Fluid-Pad interface geometry due to thermal and mechanical deformation of the pad domain. The deformed geometry affects significantly all the fields resulting in a decreased LLC and an increase of the coefficient of friction. The main evaluation results are presented on **Table 11**. The mechanical and thermal deformation on the vertical axis leads to the formation of a converging region which extends from the leading edge of the pad (inflow) to the end of the textured surface area, and a diverging region from the end of the textured surface area to the trailing edge (outflow). The converging region results in a better pressure build up in the inflow direction, which eliminates the cavitation into the dimples. However, because of the diverging region the pressure drop is increased in the outflow direction and therefore a cavitating region is created on the outer radius of the trailing edge as observed on **Figure 84b**. The pressure-drop combined with the lower maximum pressure decreases the LLC. The deformed geometry is outlined on **Figure 88**, along with the pressure profile on **Figure 89** and **Figure 92** and the temperature profile on **Figure 90** and **Figure 93**, at a radius of 34mm- **Figure 87** and angular position of 22.5°- **Figure 91**.

Table 11 – TEHD evaluation results

Final Min. Film Thickness	20 µm
Max Oil Pressure	1.72 MPa
Load Carrying Capacity	242.6 N
Friction Torque	0.190 Nm
Coefficient of Friction	0.0224
Max Oil Temperature	89.5°C
Max Air/Oil Vol. Fraction	63.50%
Maximum Mesh Displacement	9.7 µm

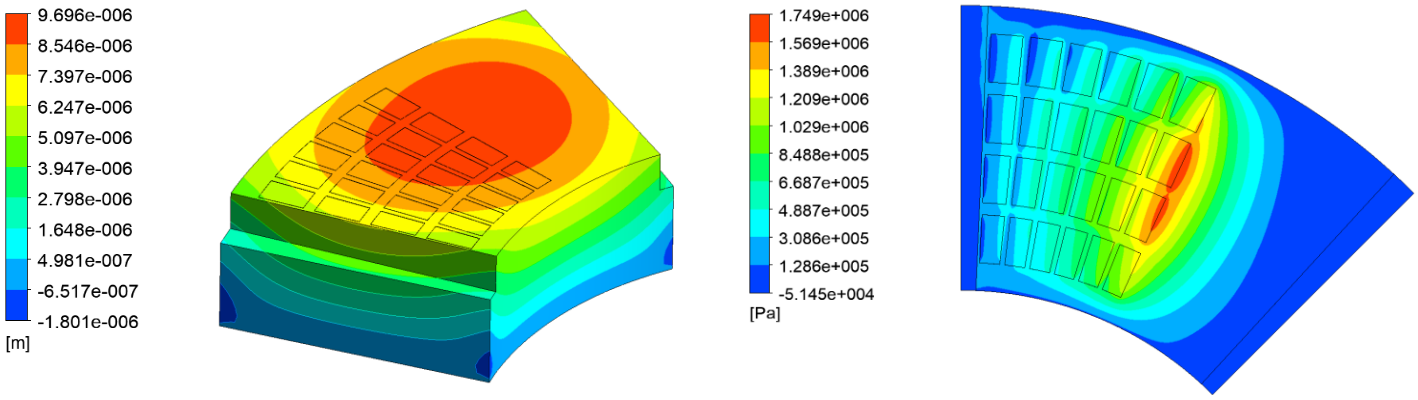

(a) **(b)**

Figure 84 – a) Mesh Displacement at the fluid-pad interface, b) Pressure field at the fluid-pad interface

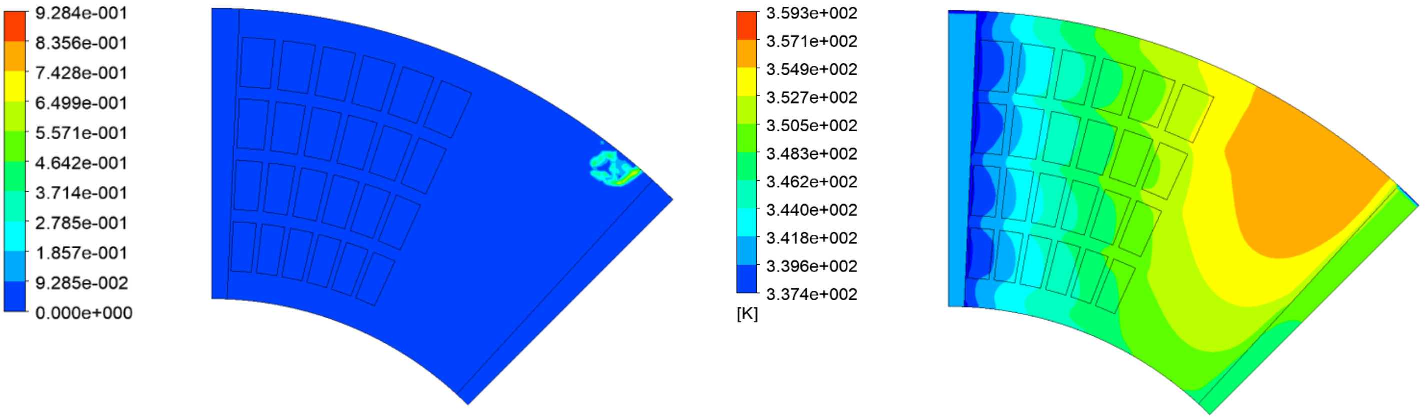

(a) **(b)**

Figure 85 - a) Volume fraction field at the fluid-pad interface, b) Temperature field at fluid- pad interface

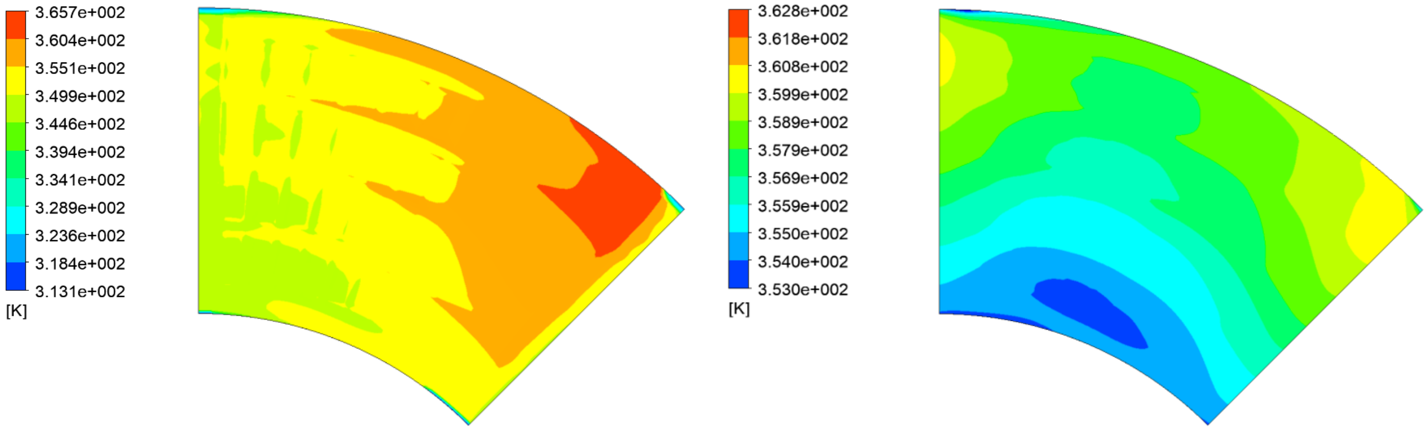

(a)

(b)

Figure 86 – Temperature field at a) Midline of Film Thickness, b) Fluid-Rotor Interface

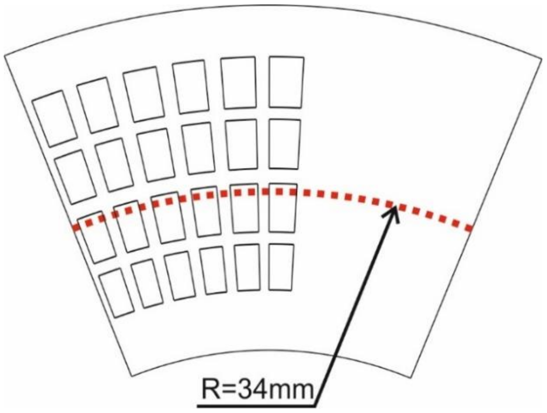

Figure 87 – Circumferential line at a radius of 34mm

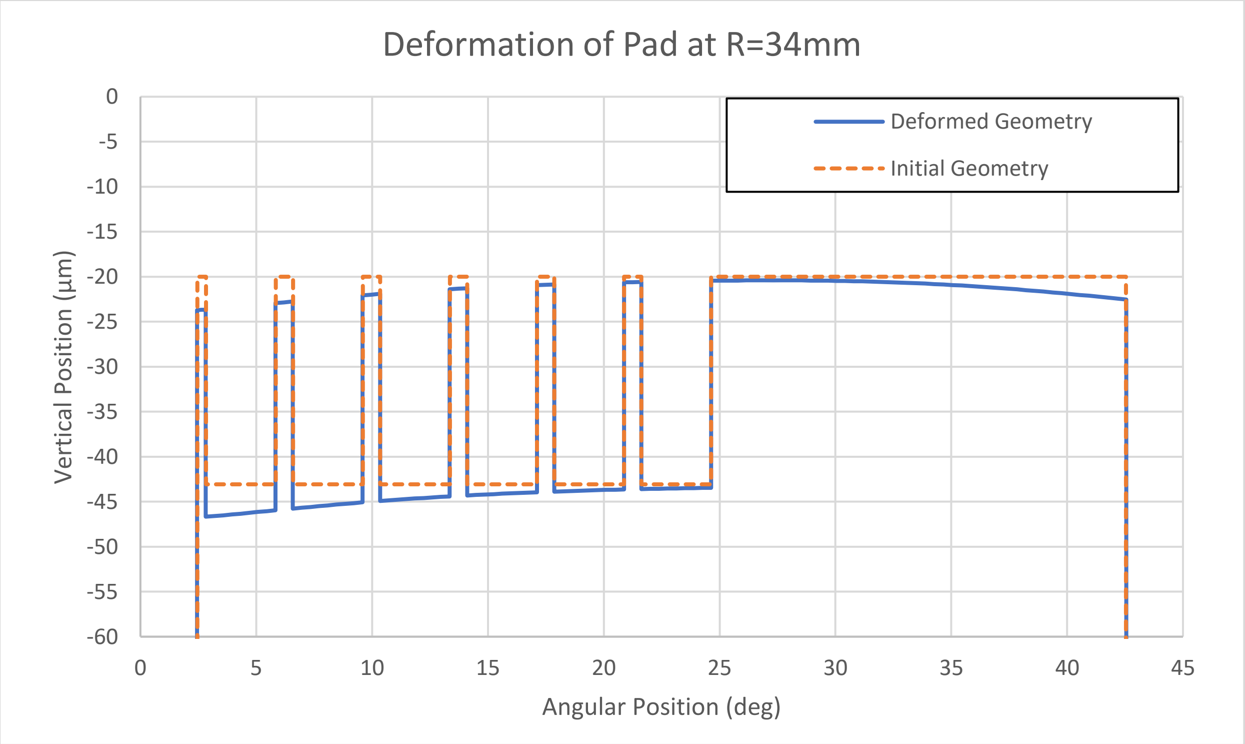

Figure 88 – Deformation of Pad at R=34mm

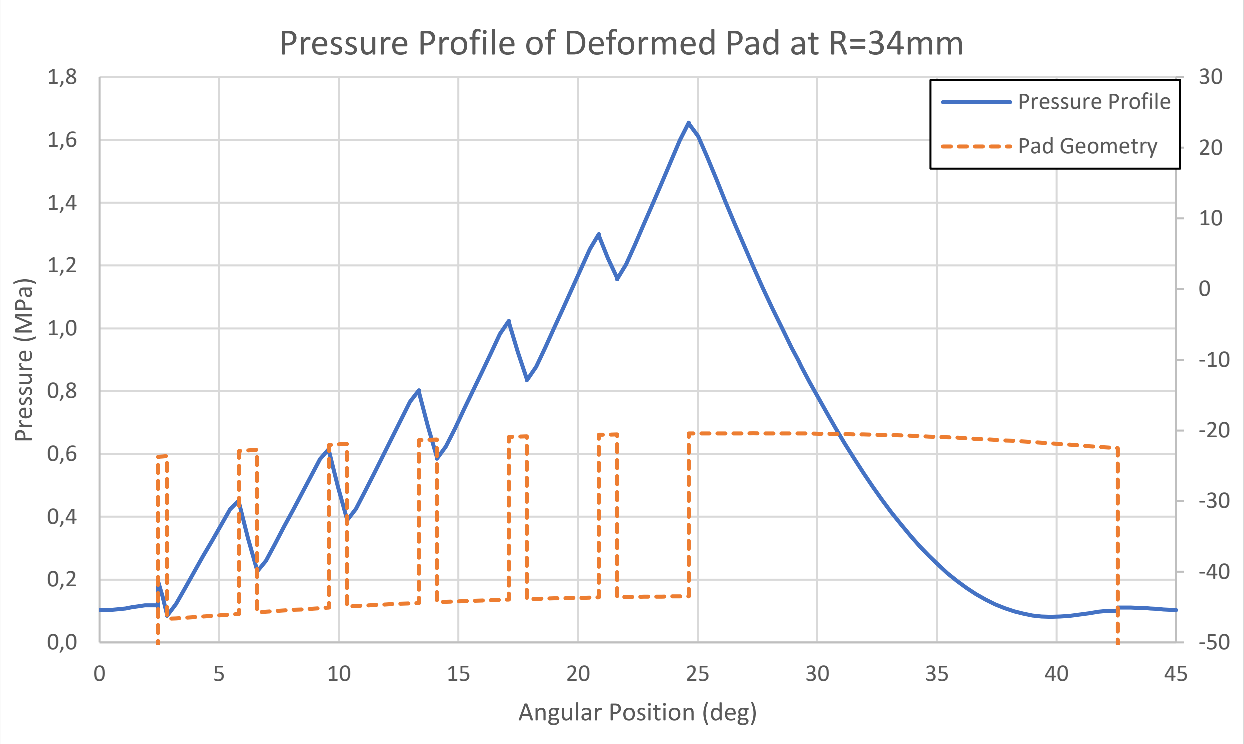

Figure 89 – Pressure Profile at R=34mm

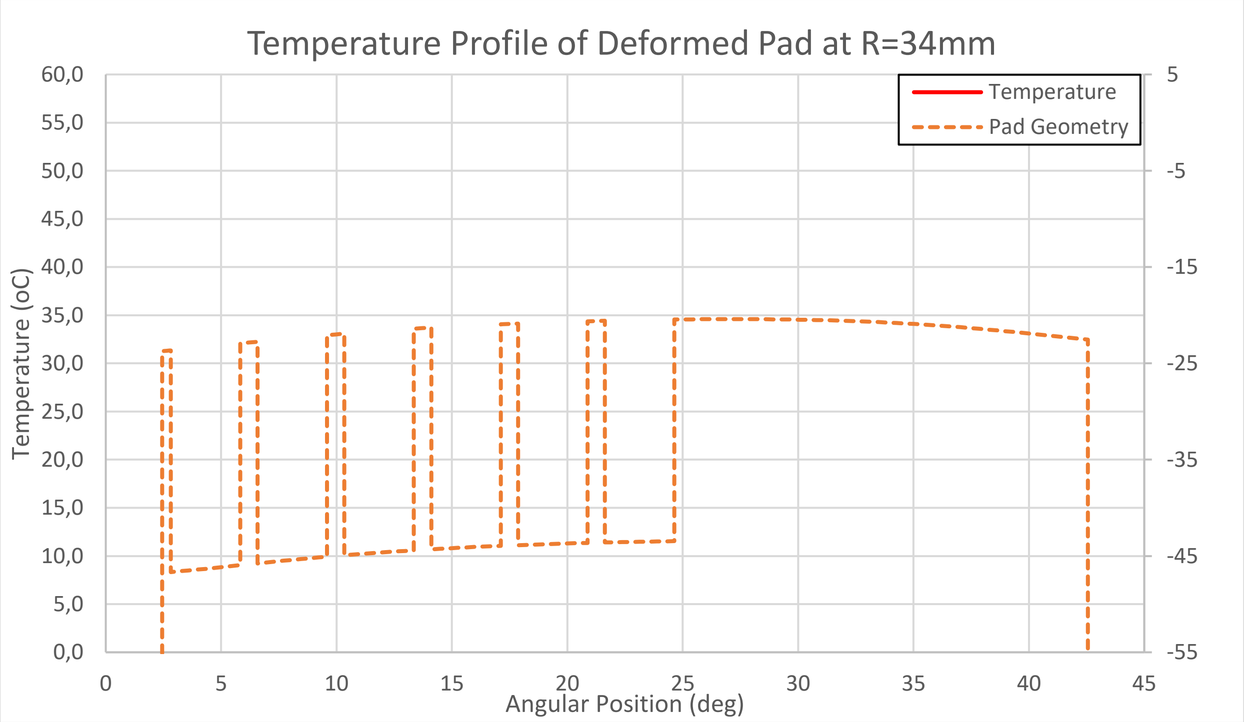

Figure 90 – Temperature Profile at R=34mm

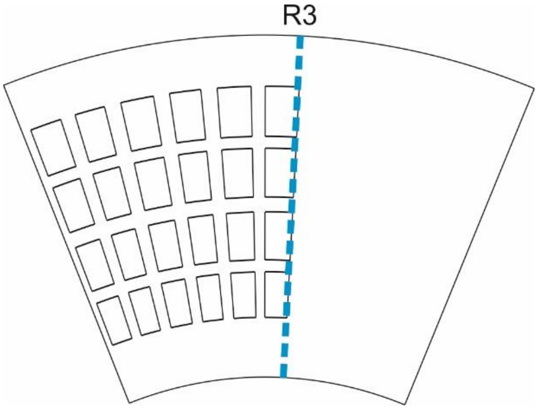

Figure 91 – Radial Position at 22.5°

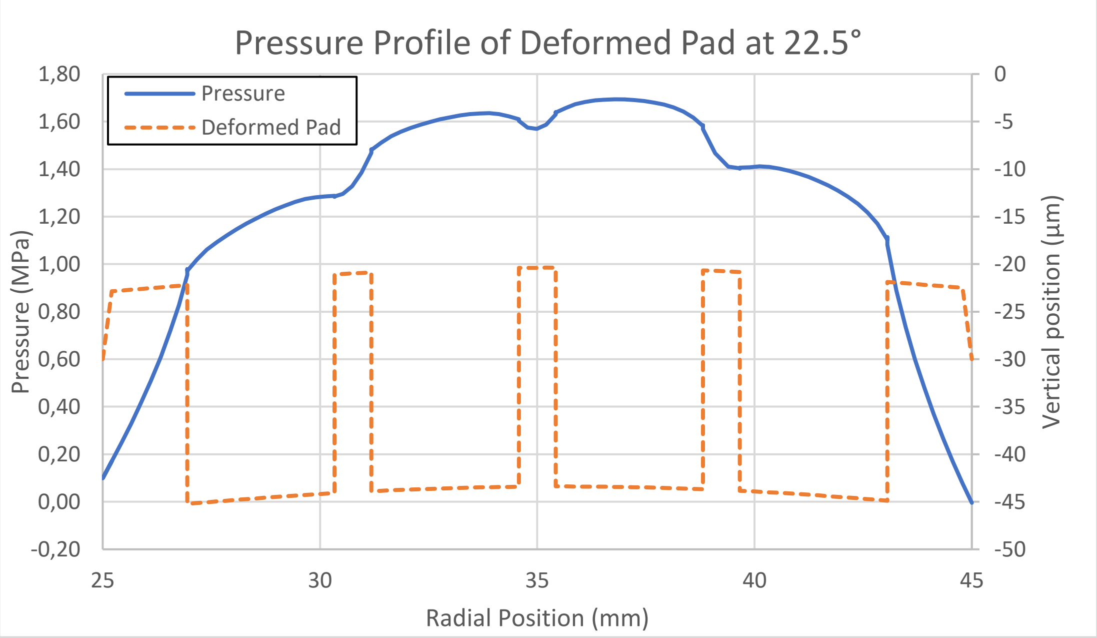

Figure 92 – Pressure Profile at 22.5°

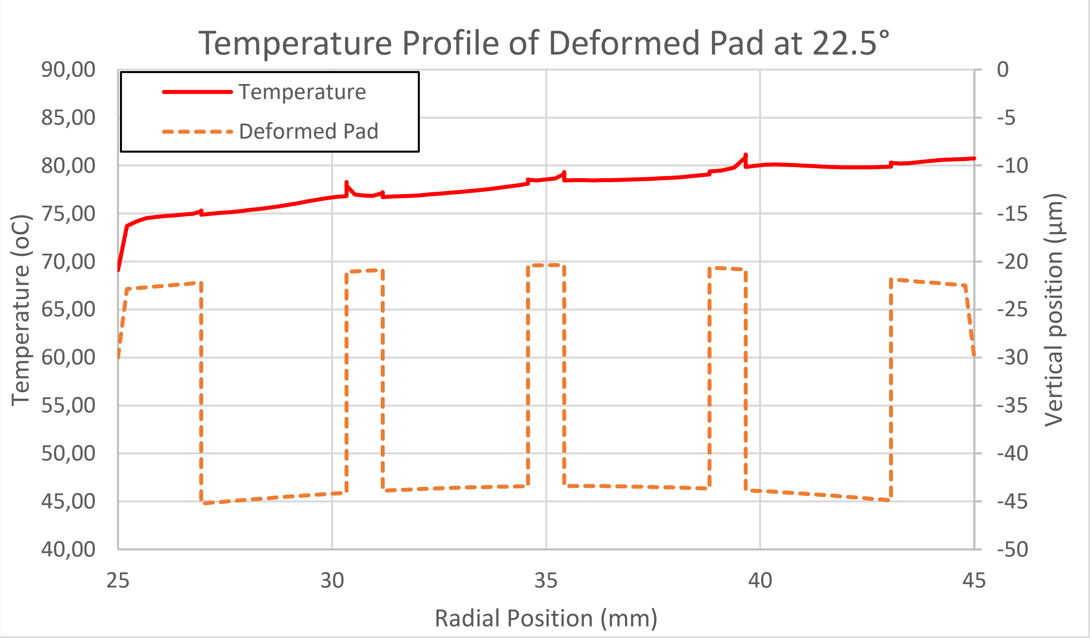

Figure 93 – Temperature Profile at 22.5°

For various radii and angular positions, the pressure and temperature profiles have been calculated in order to create 3d-plots. The pressure distribution can be observed on **Figure 94** and **Figure 95** and the Temperature distribution on **Figure 96** and **Figure 97**.

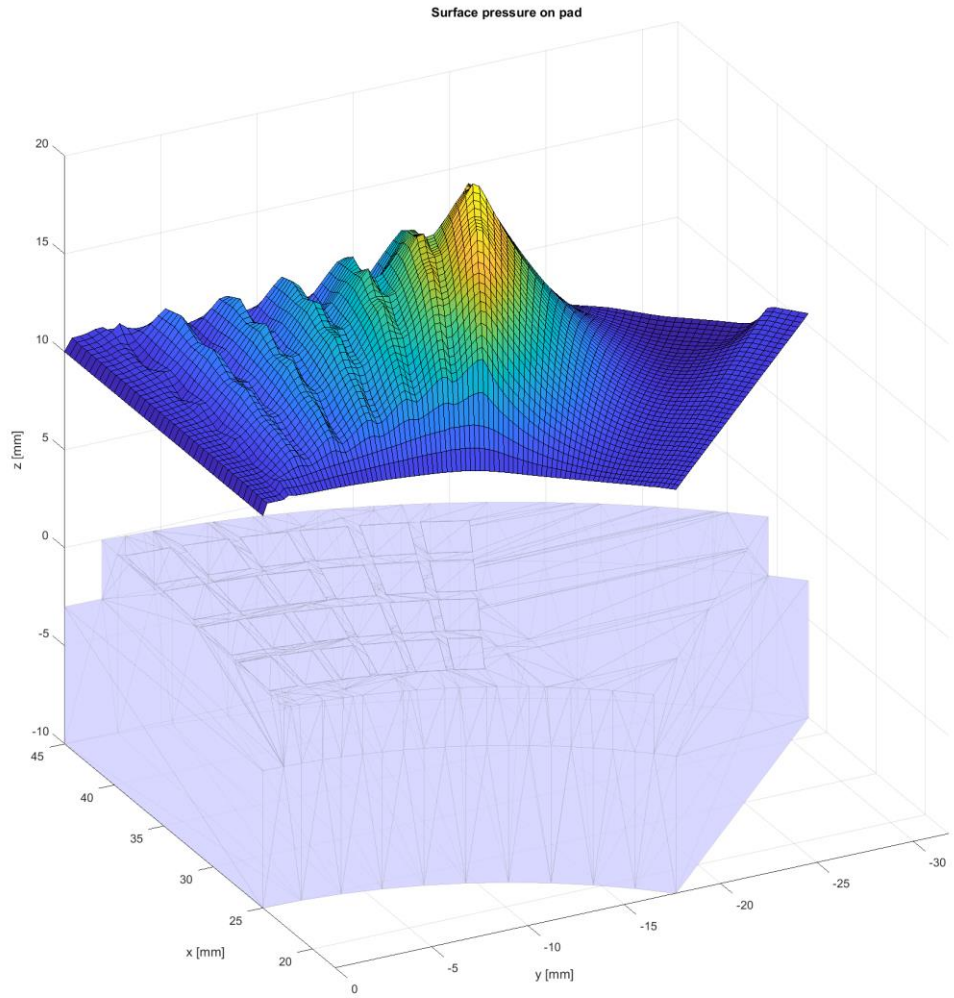

Figure 94 – 3D Pressure of TEHD model on Pad

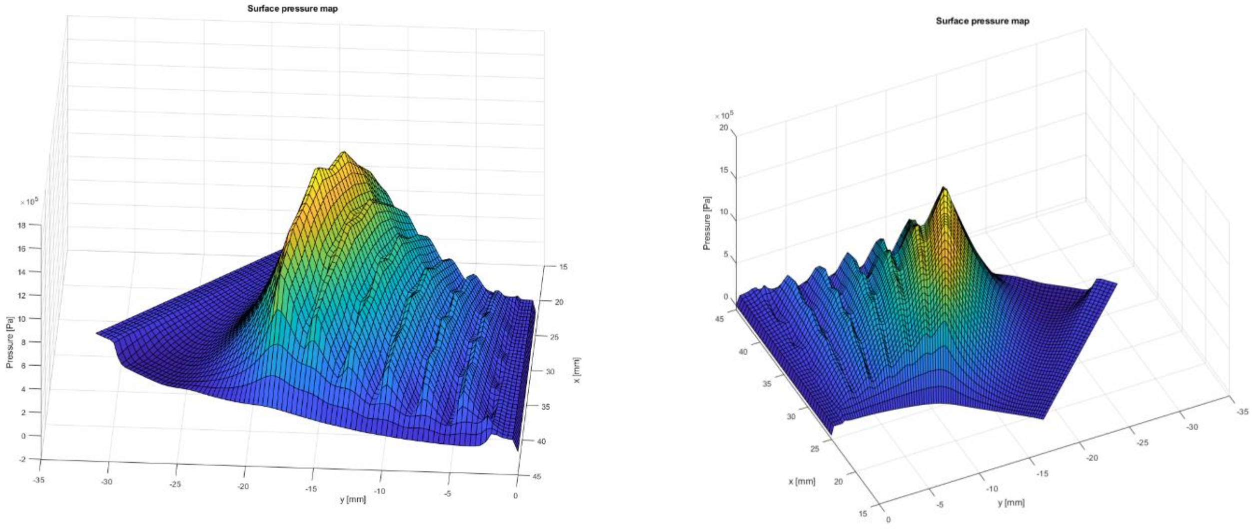

(a)

(b)

Figure 95 – 3D Pressure Field of TEHD model a) Outer Radius b) Inner Radius

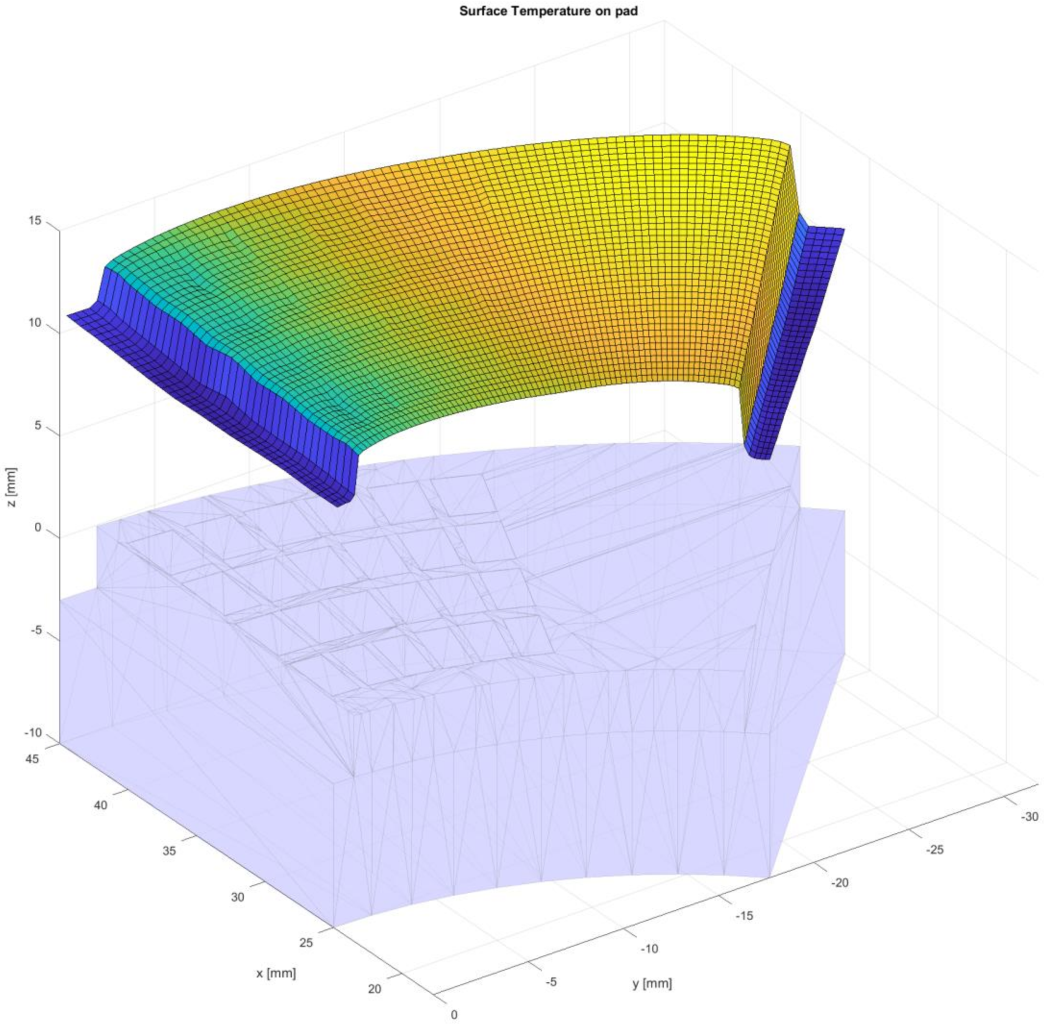

Figure 96 – 3D Temperature Field of TEHD model on Pad

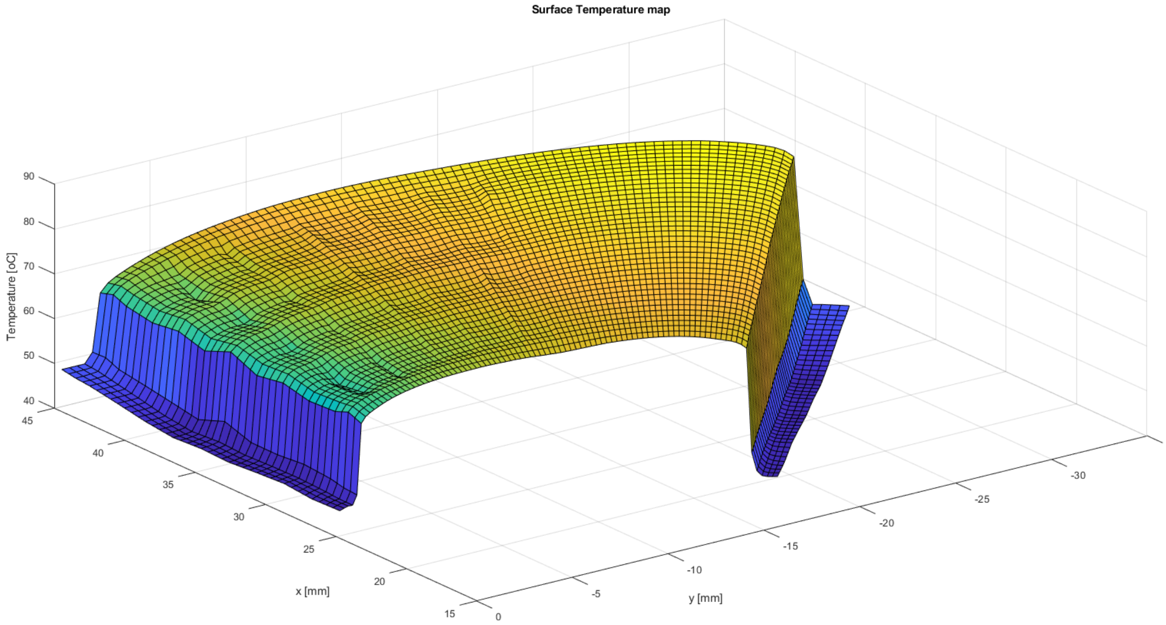

Figure 97 – 3D Temperature Field of TEHD model

In **Figure 95** the pressure drop on the outer radius of the trailing edge can be observed. In this area the pressure field bends the surface inwards, creating a cavitating region. Also, from **Figure 97** a temperature drop can be observed inside the dimples.

2.6.2 TEHD and THD comparison

The converging and diverging region can be clearly identified from **Figure 101**. Also, the effect of these regions on the pressure profile can be indicated on **Figure 102**. From 0° to 22.5° the pressure build-up is increased. However, from 24.5° to 45° the pressure drops sharply for the TEHD model leading to a decreased overall pressure integral and therefore a lower value of Load Carrying Capacity. Moreover, the overall oil temperature is lower for the TEHD model as pointed out on **Figure 99** and **Figure 103**. This can be attributed to the insertion of more cold fluid into the pad domain due to the converging region in the inlet. The difference of the calculated values can be seen on **Table 12**.

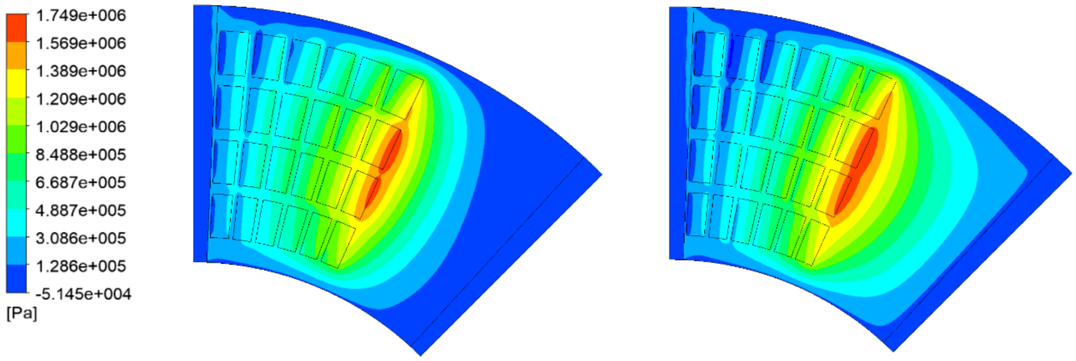

(a) **(b)**

Figure 98 – Pressure field at the fluid-pad interface a) TEHD, b) THD

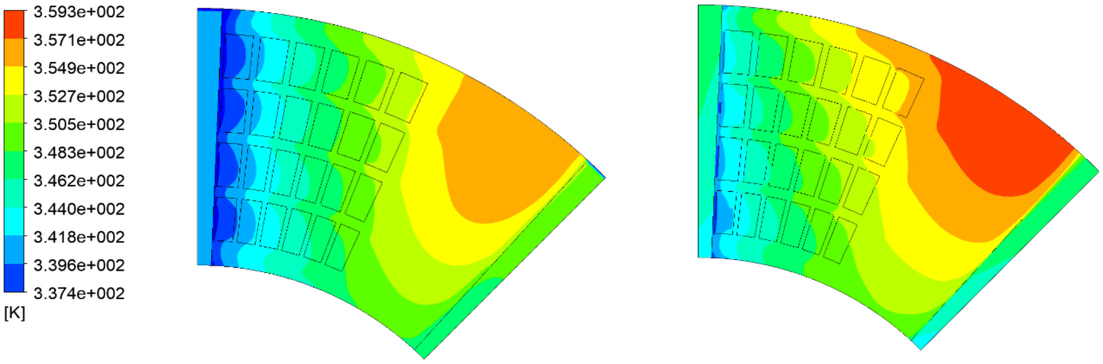

(a) **(b)**

Figure 99 – Temperature field at fluid-pad interface a) TEHD, b) THD

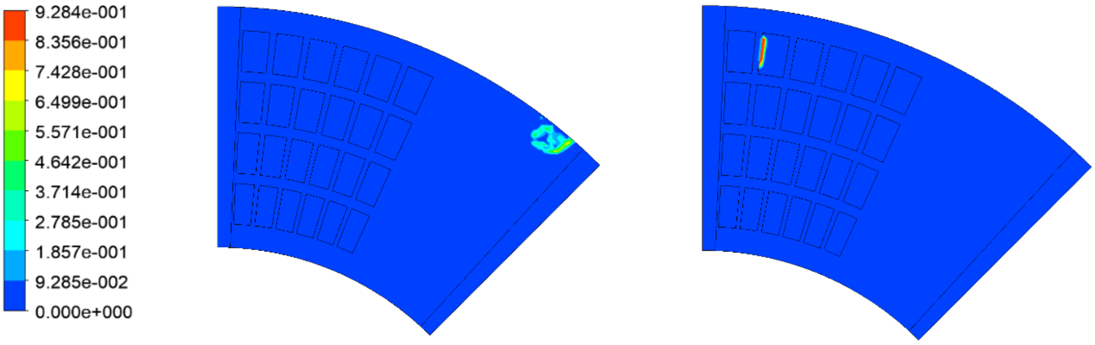

(a) **(b)**

Figure 100 - Volume fraction field at fluid-pad interface a) TEHD, b) THD

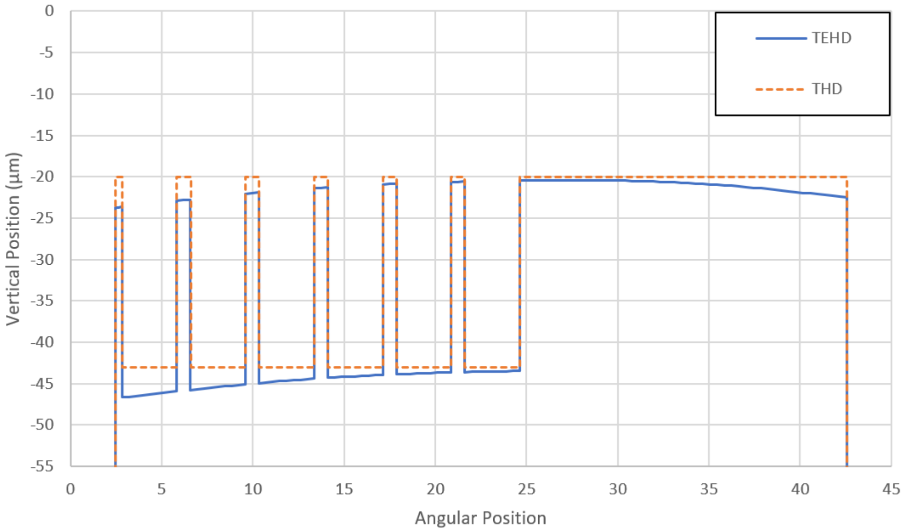

Figure 101 – Pad Geometries for TEHD and THD models at a radius of 34mm

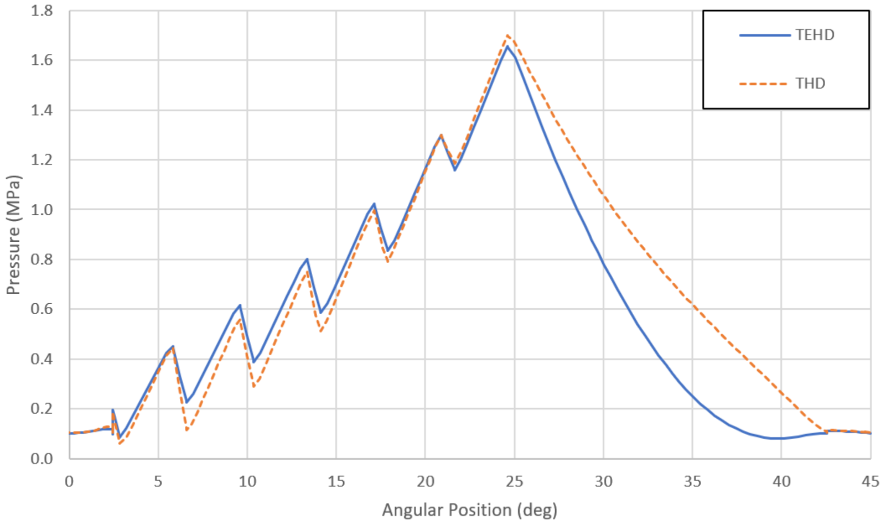

Figure 102 – Pressure Profiles for TEHD and THD models at a radius of 34mm

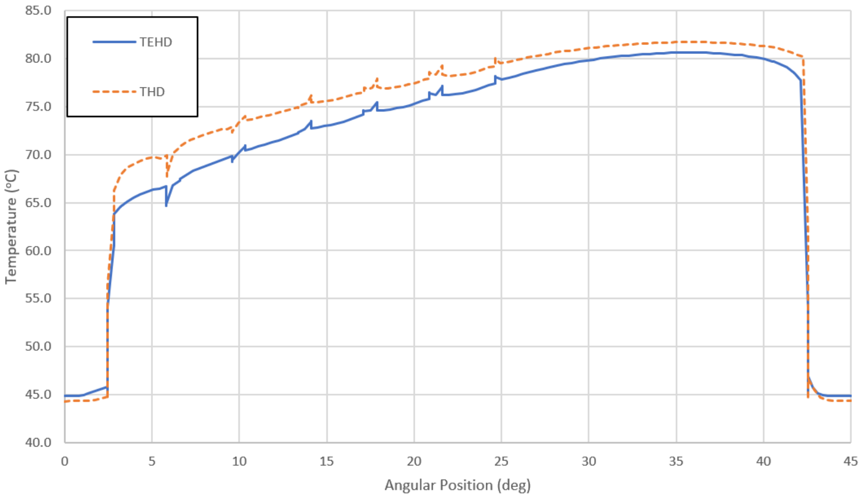

Figure 103 – Temperature Profiles for TEHD and THD models at a radius of 34mm

Table 12 – TEHD vs THD results comparison

	Units	THD	TEHD	Difference
Maximum Pressure	MPa	1.75	1.72	-1.7%
Load Carrying Capacity	N	278.2	242.6	-12.7%
Friction Torque	Nm	0.198	0.19	-4.0%
Coefficient of Friction	ul	0.0203	0.0224	+10.3%
Maximum Temperature	℃	92.7	89.5	-3.2
Maximum Volume Fraction	ul	92.8%	63.5%	-
Maximum Mesh Displacement	µm	-	9.7	-

In the process of understanding the behavior of the pressure and temperature fields the 3D graphs of the pressure and temperature distribution at the Fluid-Pad interface have been compared for both the TEHD and THD models. The colors are proportional to the Pressure and Temperature values. It can be clearly observed in **Figure 104** that the pressure drop is steeper for the TEHD model on the outlet. Moreover, in **Figure 104b** the cavitation area for the TEHD model is highlighted. The decreased value of pressure bends the surface inwards in this region. From **Figure 105** a drop of the fluid temperature can be observed inside the dimples.

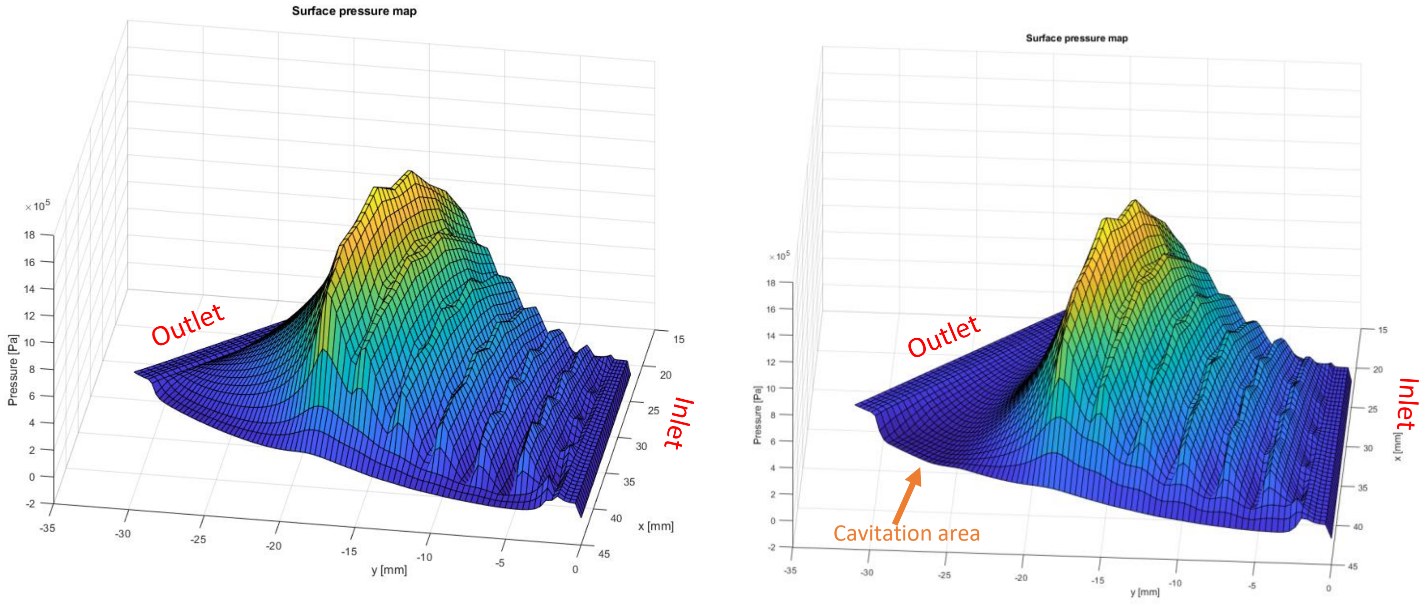

(a) (b)

Figure 104 – 3-D pressure field at Fluid-Pad interface a)THD, b)TEHD

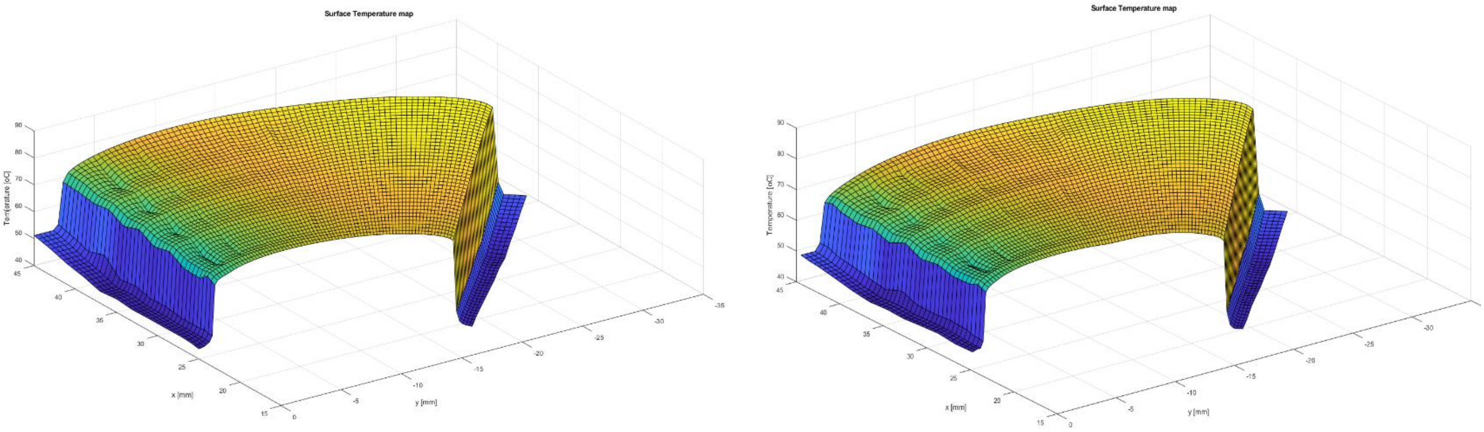

(a) (b)

Figure 105 – 3-D temperature field at Fluid-Pad interface a)THD, b)TEHD

2.6.3 TEHD Sensitivity Analysis

A sensitivity analysis of the design parameters has been performed utilising the TEHD model. A variation of ±2% for the textured Length (L) and textured Width (B) has been considered and ±2μm for the textured Depth (TD).

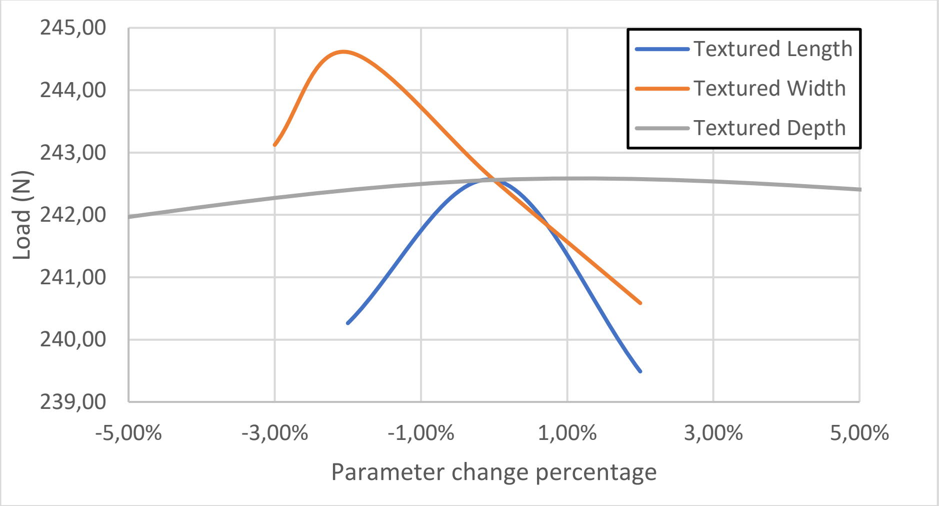

Figure 106 - TEHD Parametric Analysis Load

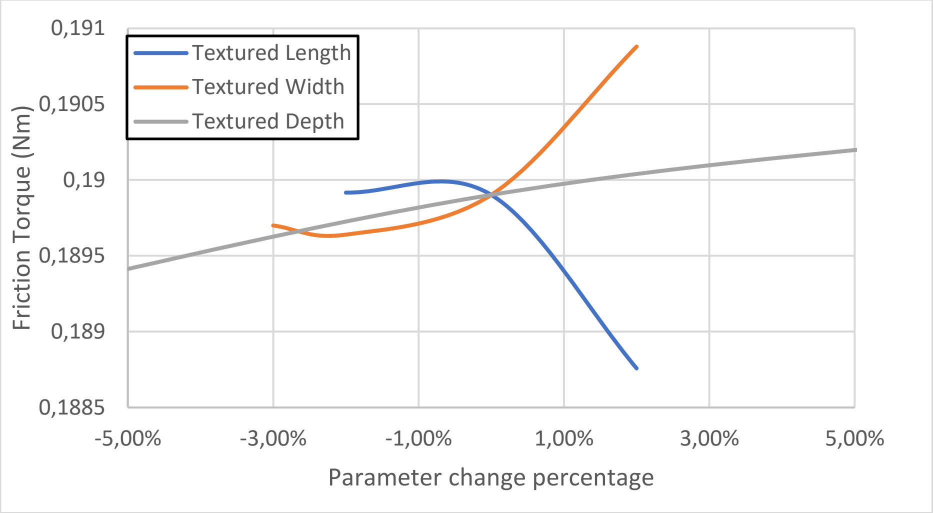

Figure 107 - TEHD Parametric Analysis Friction Torque

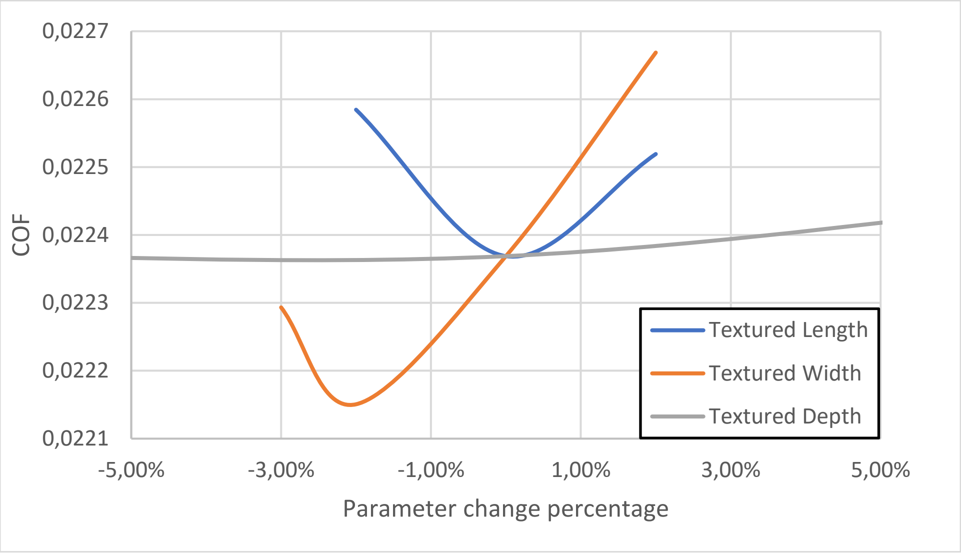

Figure 108 - TEHD Parametric Analysis Friction Coefficient

The results of the THD and TEHD optima are almost the same for the textured length and depth as seen on **Figure 106-108**. However, for a lower value of textured width there seems to be an increase of the LLC and a decrease of the friction torque, leading to an improvement of the coefficient of friction. On **Figure 109a** the pad with decreased texture width indicates a better pressure distribution on the center, which results in an increase of LCC by approximately 1%. The temperature of the fluid is slightly higher both at the fluid-pad and fluid-rotor interfaces for this design, as seen on **Figure 110** and **Figure 111**, which results in lower viscosity on this region and therefore decreased value of friction torque. The overall coefficient of friction is decreased by 1%. This indicates that bearing design optimisation with THD modeling is relevant and for accurate bearing performance quantification, TEHD simulations must be performed.

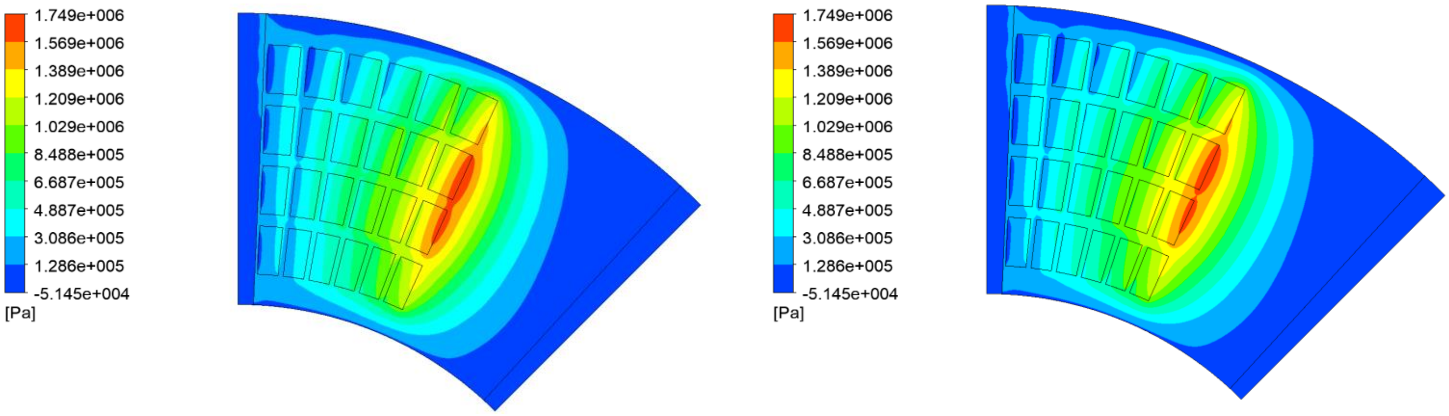

(a) **(b)**

Figure 109 – Pressure field at the fluid-pad interface a) -2% of optimal Textured Width, b) THD optimal

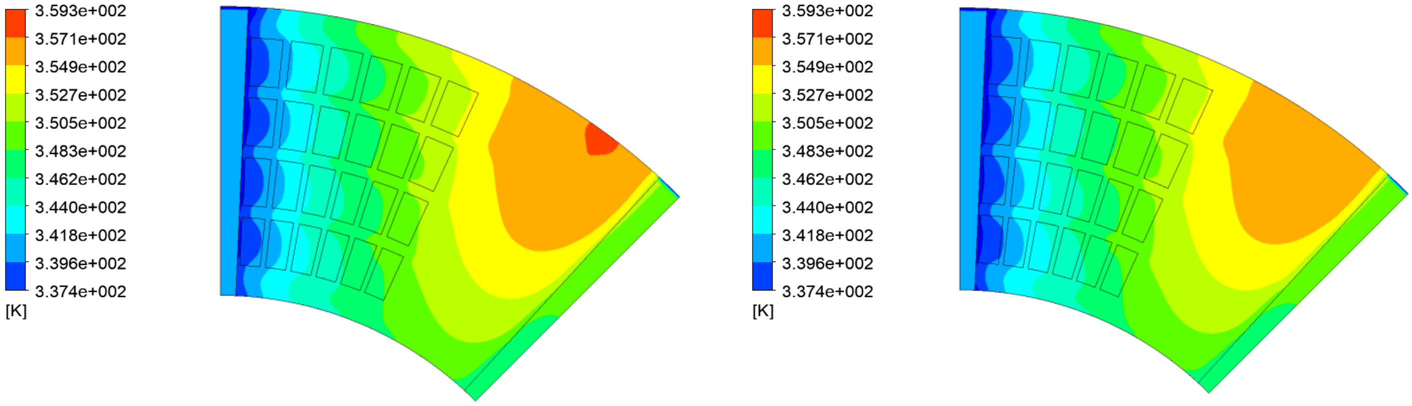

(a) **(b)**

Figure 110 – Temperature field at the fluid-pad interface a)-2% of optimal Textured Width, b) THD optimal

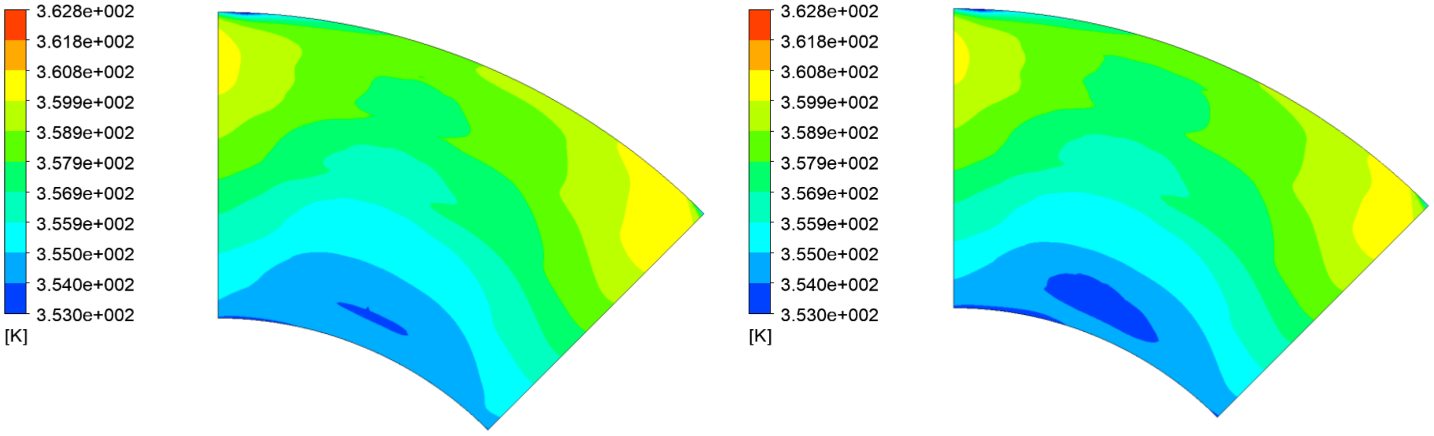

(a) **(b)**

Figure 111 – Temperature field at the fluid-rotor interface a)-2% of optimal Textured Width, b) THD optimal

2.7 TEHD model of Tapered Land

In this case a tapered land thrust bearing was designed in order to assess the mechanical and thermal deformations on the performance of this type of geometry. The geometry parameters were selected from a previous optimisation (Koutsoubas). The minimum film thickness was set at 20μm. According to **Figure 5,** hmin=20μm and h1=85μm.

2.7.1 Meshing procedure

The final mesh parameters have been selected following a detailed mesh study. Regarding the pad domain, due to the thermal and mechanical deformations, a dense hexahedral mesh has been utilised, composed of 510,000elements. The fluid domain is discretised with hexahedral elements, utilising 15 layers of elements in the crossflow (film thickness) direction, whereas in the longitudinal and transverse directions, 150 and 60 elements have been used, respectively. The total number of elements in the fluid domain is 340,000, and in the rotor domain is 350,000. The rotor is assumed rigid, therefore, only the heat transfer equations are solved. Mesh details about the computational domains are presented in **Figure 112-113**. The boundary conditions were selected as in **2.4.4 Boundary Conditions.**

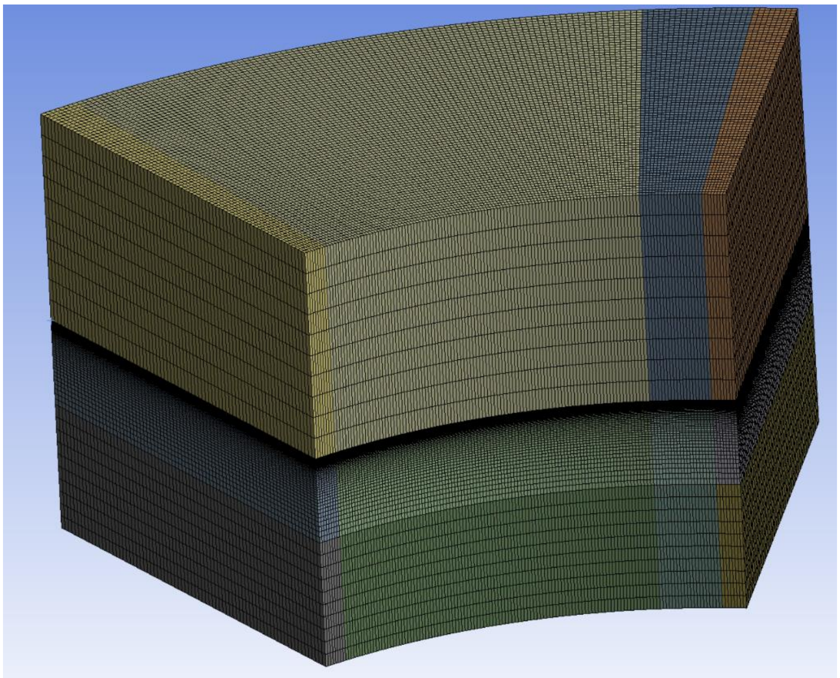

Figure 112 – Tapered-land Meshing

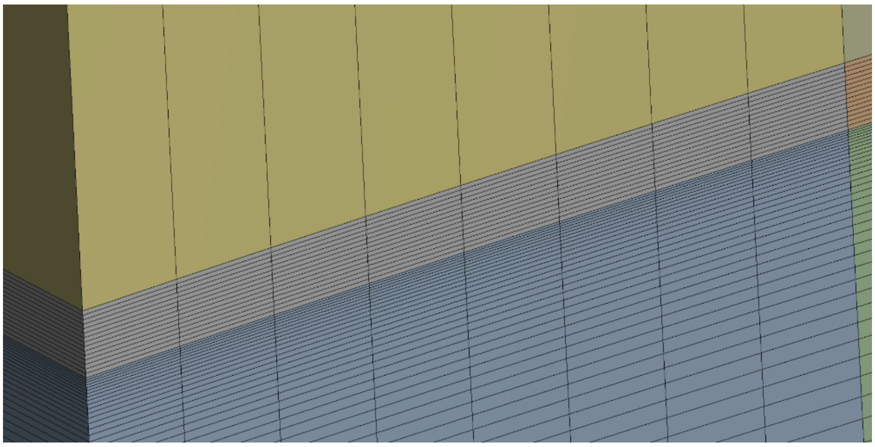

Figure 113 - Elements in crossflow direction

2.7.2 Results

The results on **Figure 114a** indicate an alteration of the Fluid-Pad interface geometry due to thermal and mechanical deformation of the pad domain. The pressure field shown on **Figure 114b,** is as expected for a tapered-land geometry. The maximum temperature occurs in the midline of the film thickness, as seen on **Figure 115b.** The temperature values are higher on the outer radius of the trailing edge, as seen on **Figure 115** and **Figure 116.** The temperature on the rotor is significantly higher compared to the stator. The stator is cooled by the inflow of cold oil whereas the rotor is heated due to heat convection from the fluid.

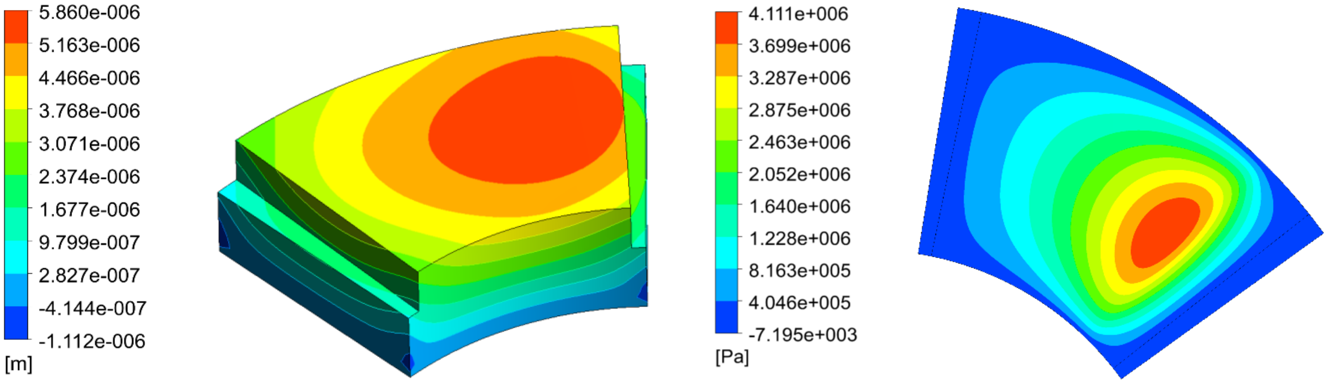

(a) **(b)**

Figure 114 – a) Mesh Displacement at Pad, b) Pressure field at the fluid-pad interface

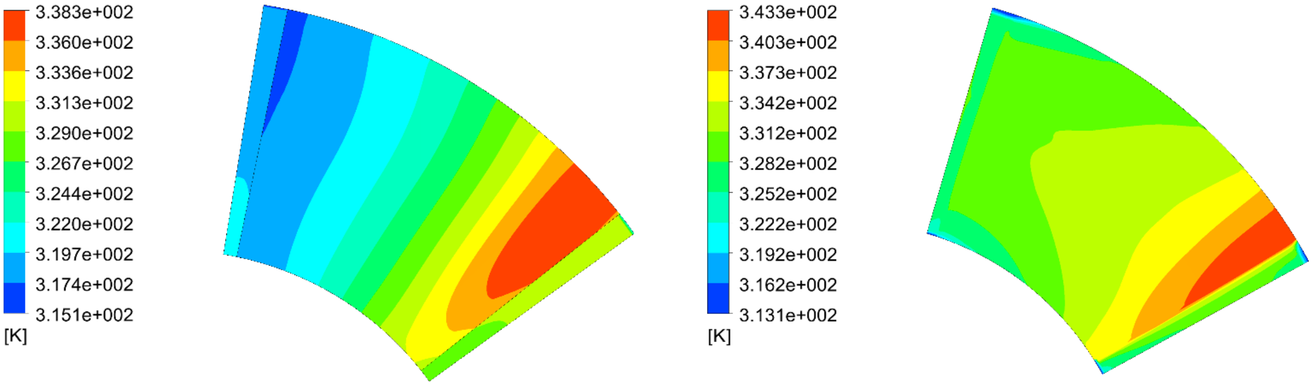

(a) **(b)**

Figure 115 - Temperature Field at a) fluid-pad interface, b) midline of Film Thickness

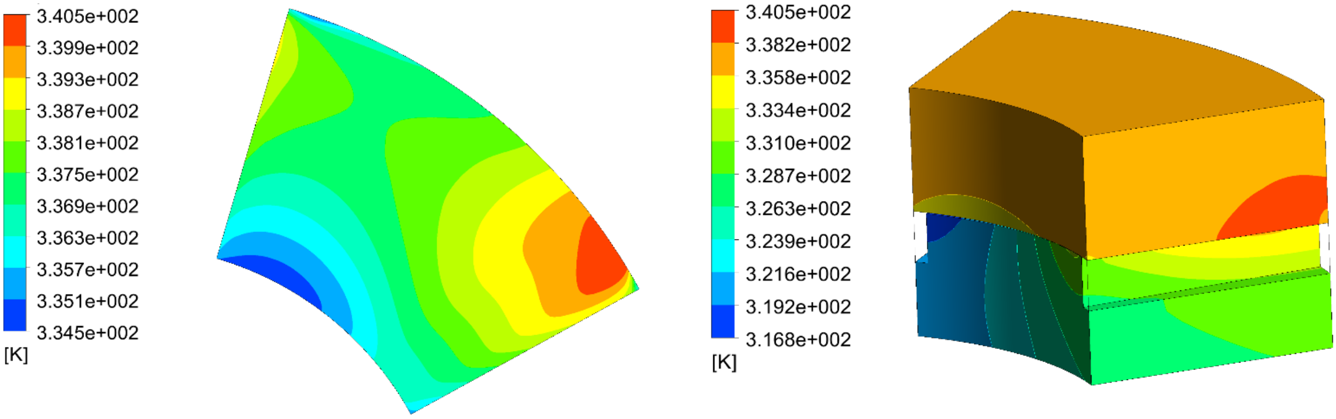

(a) **(b)**

Figure 116 - Temperature Field at a) fluid-rotor interface, b) solids

The results shown on Table 13, indicate a maximum pressure of 4.1 MPa, at an angle of 33.3°. The load carrying capacity was calculated at 688.63N, with a friction torque of 0.258 Nm, leading to a coefficient of friction of 0.0106. The maximum temperature was calculated at 70.3℃. The results from a previous THD analysis, conducted by Koutsoubas, show a decrease of the LCC by 6.81% leading to an increase of the COF by 3.6%. The circumferential pressure and temperature profiles, at a radius of 35mm, are shown on Figure 117 and Figure 118, respectively whereas the radial pressure and temperature profiles, at an angle of 33° are presented on Figure 119 and Figure 120. For a better understanding of the pressure distribution, a 3D pressure field diagram has been generated, shown on Figure 121 and Figure 122.

Table 13 - TEHD and THD Tapered-Land Results

	Units	TEHD	THD	Difference
Final Min. Film Thickness	µm	20	20	-
Max Oil Pressure	Mpa	4.1	4.3	-4.65%
Load Carrying Capacity	N	688.63	738.94	-6.81%
Friction Torque	Nm	0.258	0.267	-3.46%
Coefficient of Friction	ul	0.0106	0.0103	3.59%
Max Oil Temperature	℃	70.3	70.7	-0.4
Max Air/Oil Vol. Fraction	ul	0%	0%	-
Maximum Mesh Displacement	µm	5.86	-	-

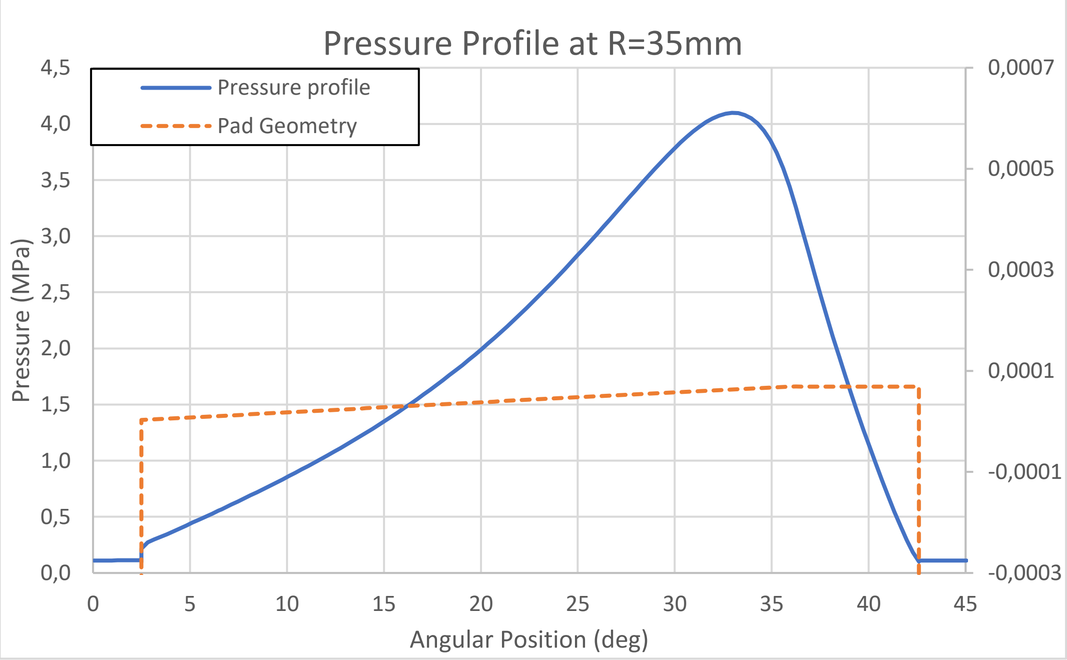

Figure 117 - Pressure profile at R=35mm

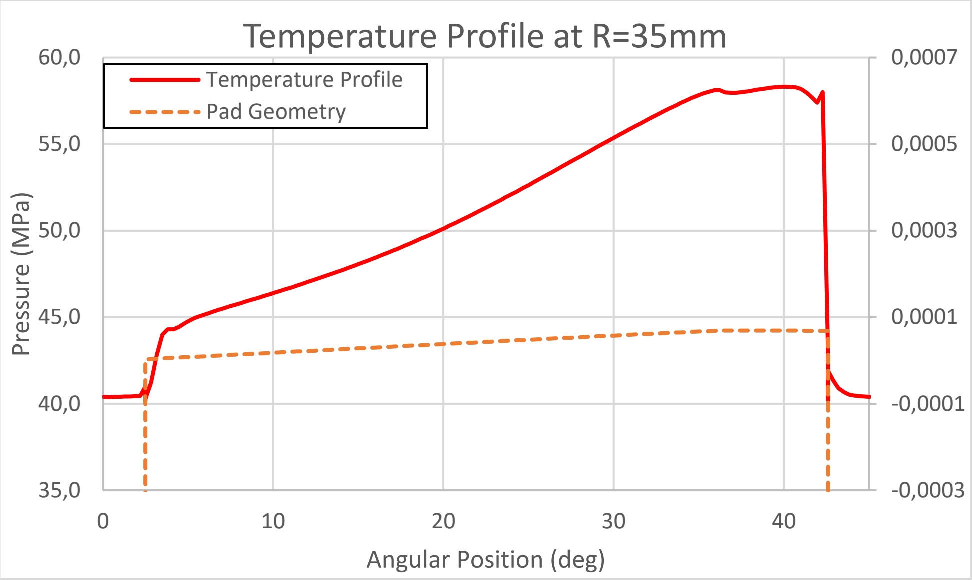

Figure 118 - Temperature profile at R=35mm

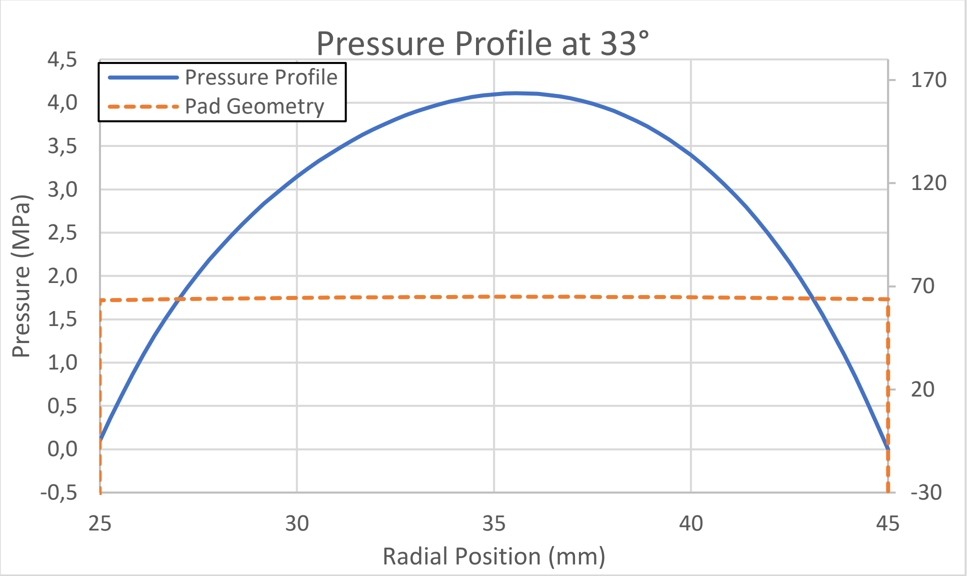

Figure 119 - Pressure profile at 33°

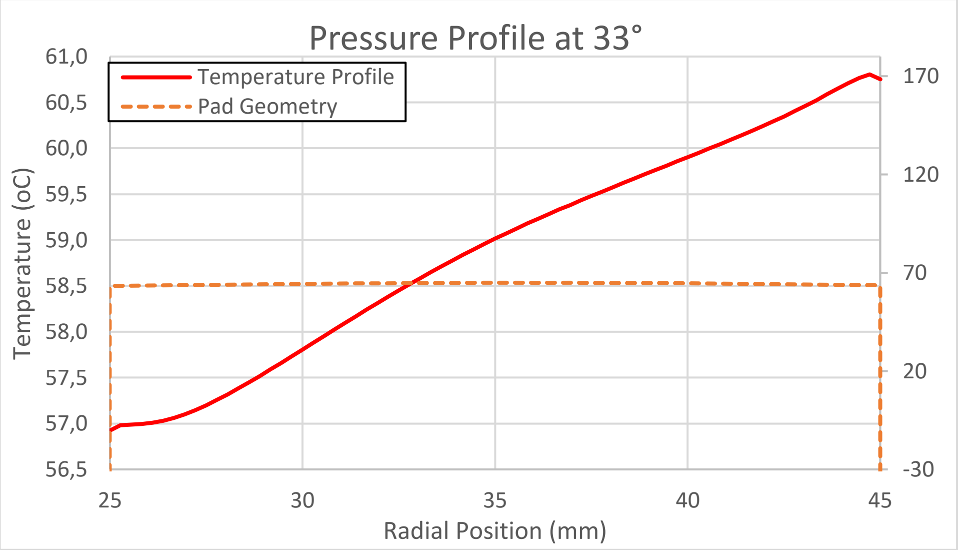

Figure 120 - Temperature profile at 33°

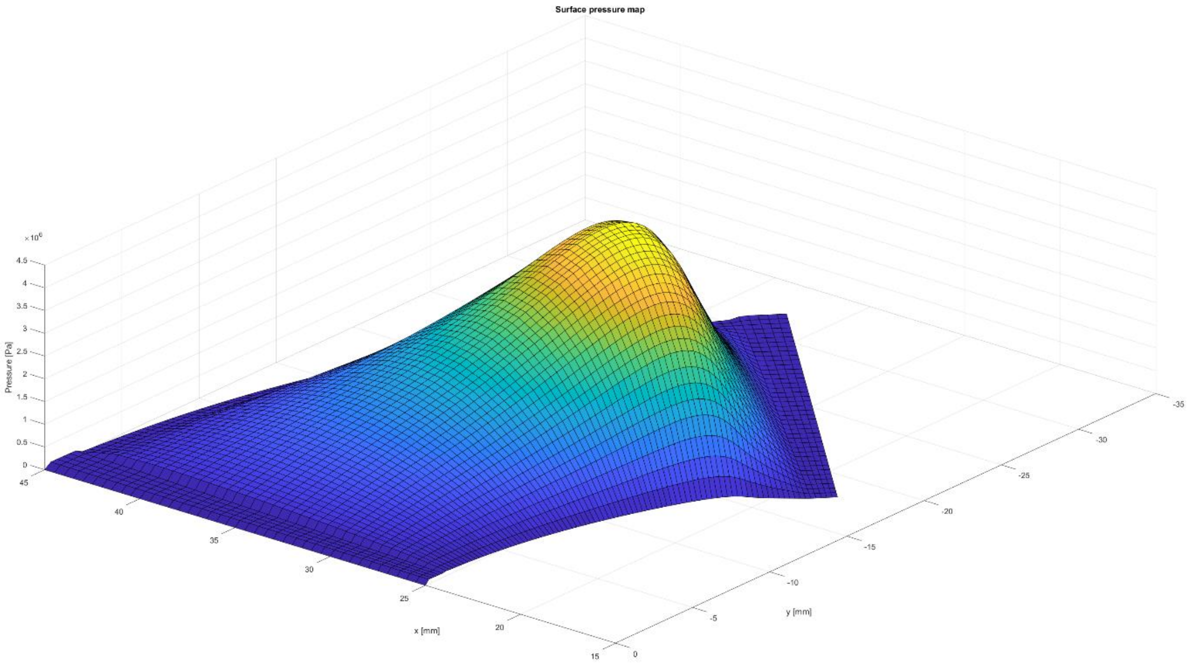

Figure 121 - 3D Pressure profile Inner Radius

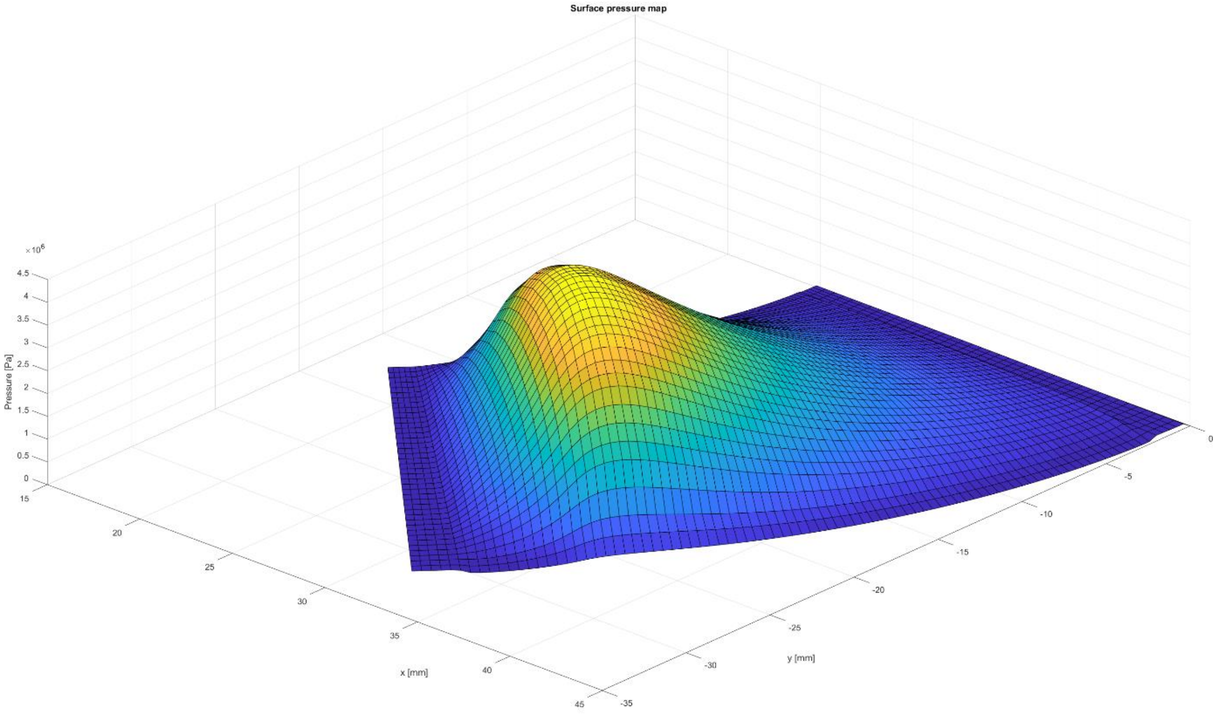

Figure 122 - 3D Pressure profile outer radius

2.8 TEHD model of a Textured Open Pocket Thrust Bearing

In this case a parallel textured thrust bearing with an open pocket was designed in order to assess the mechanical and thermal deformations on the performance of this type of geometry. The geometry parameters were selected from a previous optimisation. The minimum film thickness was set at 20µm. A schematic of the pocket geometry is shown on **Figure 123**. The textured depth was set at 35µm. The textured width was calculated as a percentage of the total width of the pad. The rotor thickness in this case is 15mm.

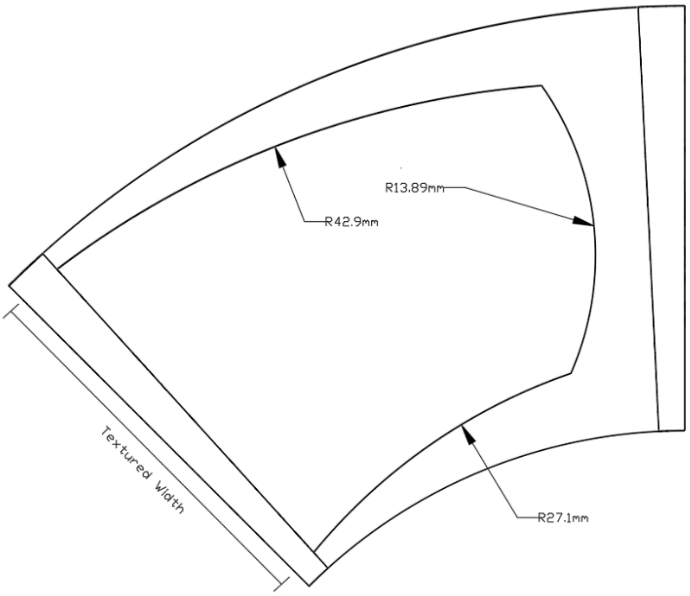

Figure 123 - Pocket Bearing Dimensions

2.8.1 Meshing procedure

The meshing details are the same as in **2.7.1 Meshing procedure.** The generated mesh is a purely hexahedral mesh with a total number of elements of approximately 1.2 million. The boundary conditions set for this study are the same as in **2.4.4 Boundary Conditions.** Meshing details of the pocket can be observed in **Figure 124**.

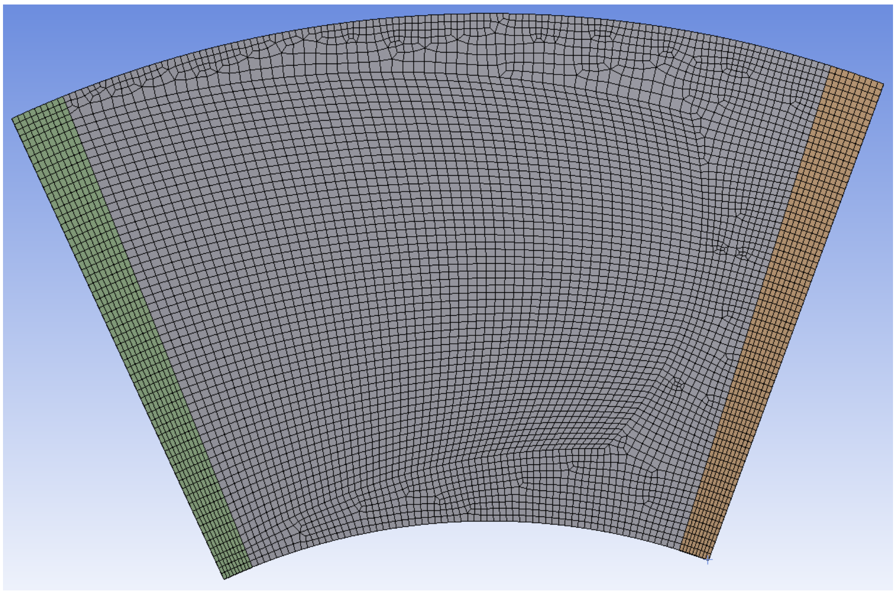

Figure 124 - Mesh Details of Pocket

2.8.2 Results

The initial film thickness was set at 26μm. The thermal and mechanical deformation led to a final minimum film thickness of 19.65 μm. The total mesh displacement of the pad is present on **Figure 125** along with the Pressure field on the fluid-pad interface. The maximum temperature was calculated at 75.4 °C, in the midline of the minimum film thickness as seen on Figure 126b. The temperature is higher on the outer radius of the trailing edge, as expected on **Figure 126a**. The temperature of the rotor is significantly higher compared to the stator, due to heat exchange with cold fluid. The calculated results are summarised on **Table 14**.

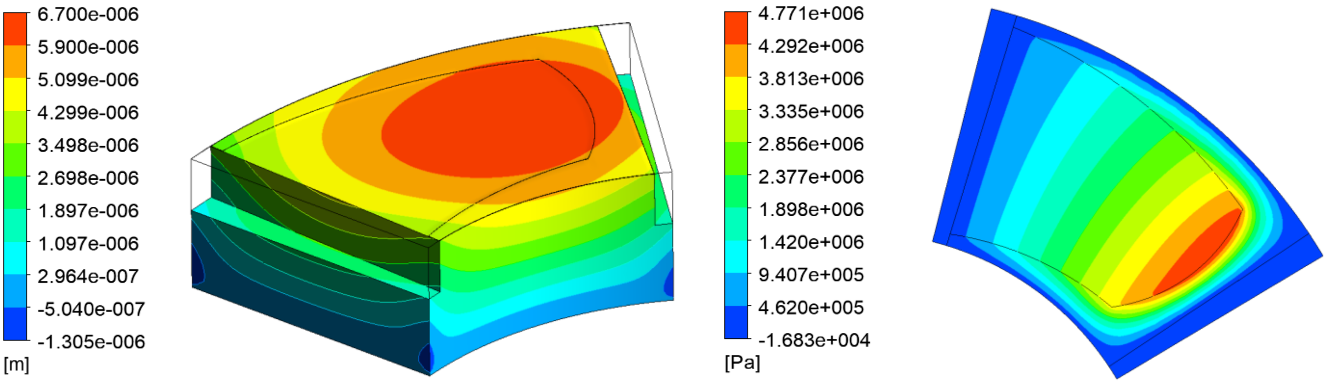

(a) **(b)**

Figure 125 - a) Mesh Displacement at Pad b) Pressure field at the fluid-pad interface

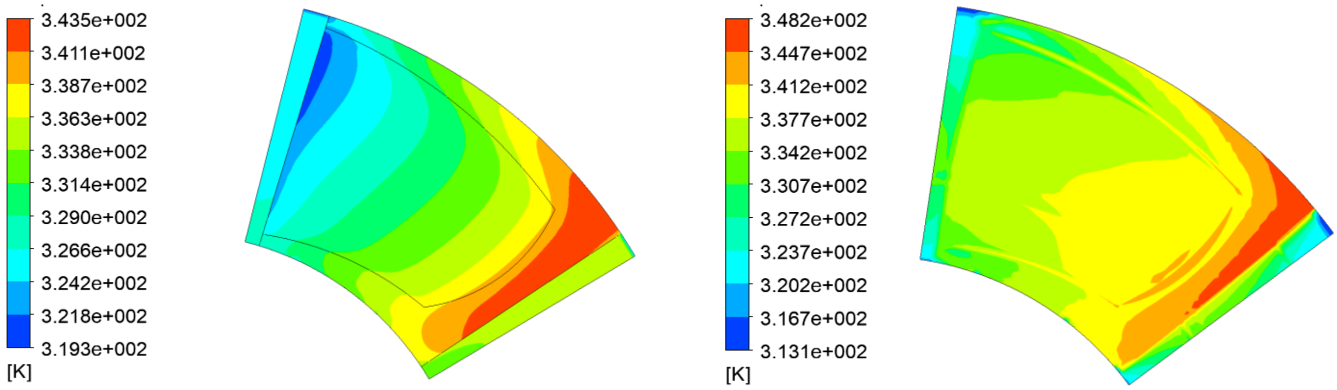

(a) **(b)**

Figure 126 - Temperature field at a) fluid-pad interface, b) midline of film thickness

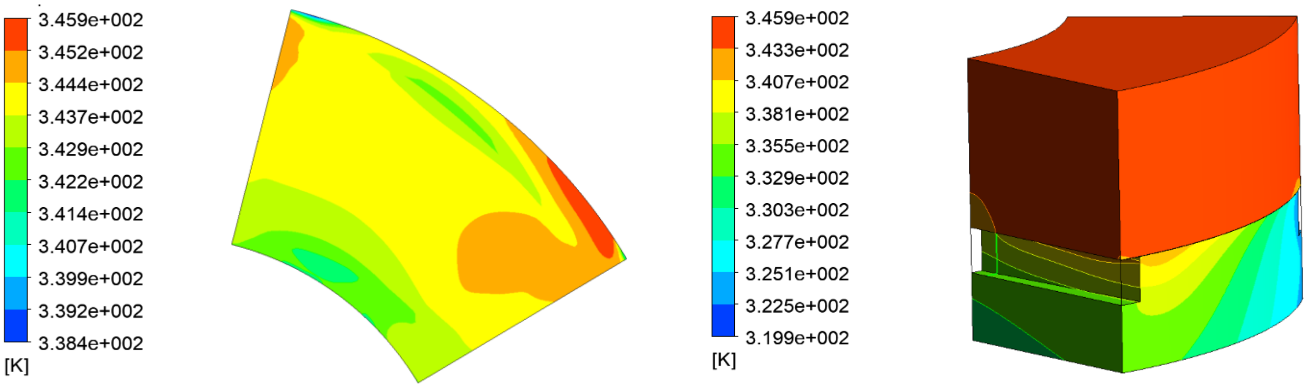

(a) **(b)**

Figure 127 - Temperature field at a) fluid-rotor interface, b) Solids

Table 14 – TEHD pocket results

	Units	TEHD
Final Min. Film Thickness	μm	19.65
Max Oil Pressure	Mpa	4.77
Load Carrying Capacity	N	909.3
Friction Torque	Nm	0.240
Coefficient of Friction	ul	0.0075
Max Oil Temperature	℃	75.4
Max Air/Oil Vol. Fraction	ul	0%
Maximum Mesh Displacement	μm	6.7

The pocket bearing exhibits a total LCC of 909.3 N. The friction torque was calculated at 0.240 Nm, resulting in a COF of 0.0075. Although the film thickness is lower than the tapered-land and textured bearings by 0.35 μm, the pocket design indicates better tribological performance in all aspects. The circumferential pressure and temperature profiles in the midline are shown in **Figure 129** and **Figure 130**. The radial pressure and temperature profiles are presented in **Figure 132** and **Figure 133.**

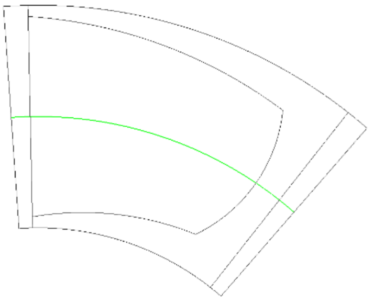

Figure 128 - Circumferential Line at R=35mm

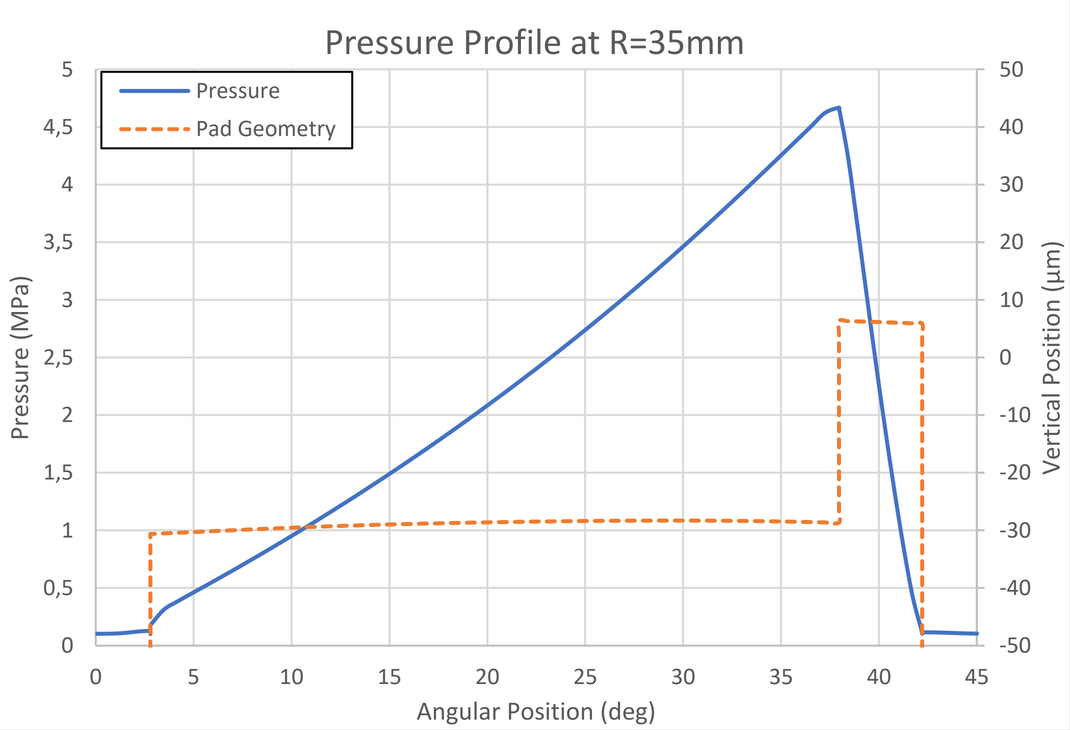

Figure 129 - Pressure Profile at R=35mm

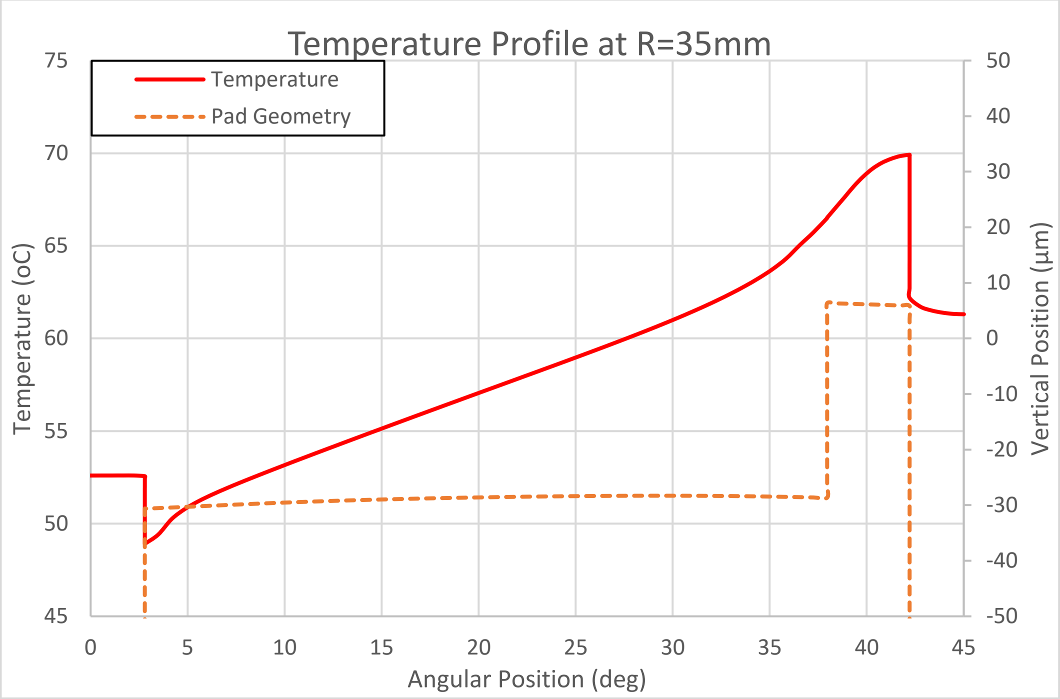

Figure 130 - Temperature Profile at R=35mm

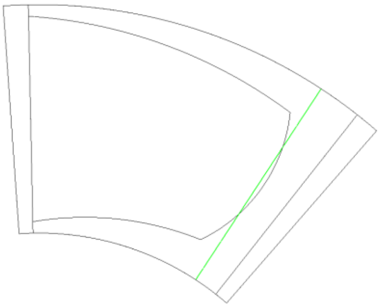

Figure 131 - Radial Line at 37.5°

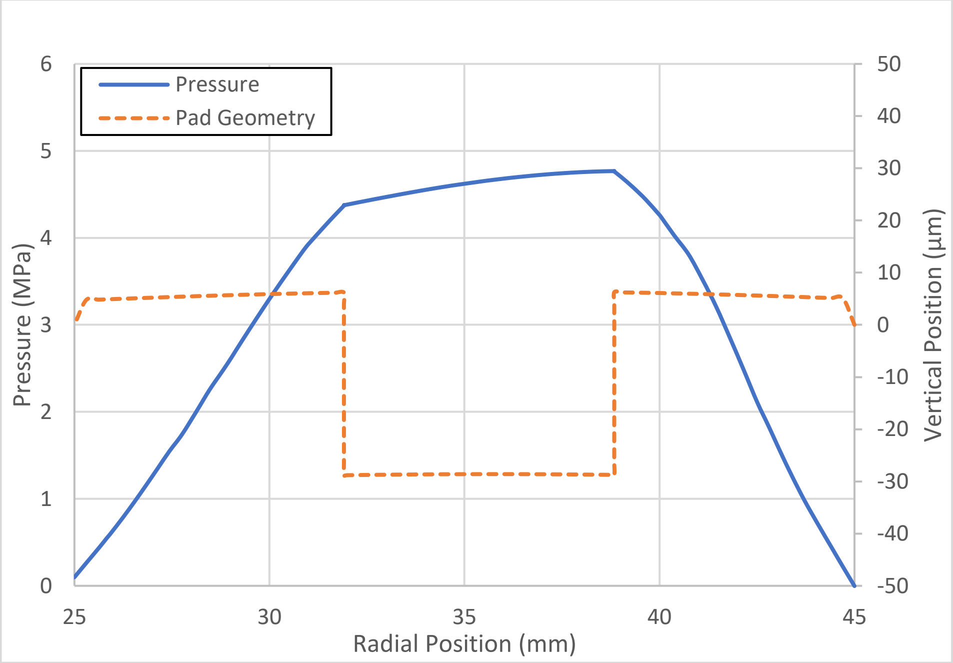

Figure 132 - Pressure Profile at 37.5°

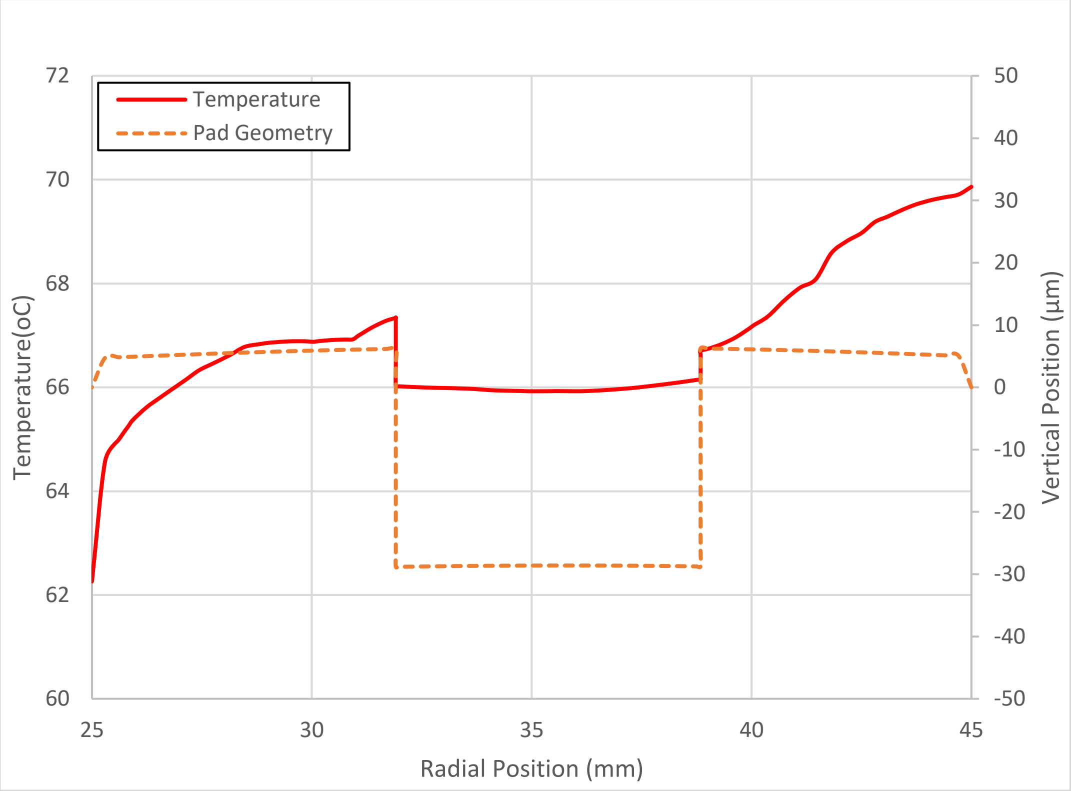

Figure 133 - Temperature Profile at 37.5°

From **Figure 133** it can be observed that the temperature of the fluid increases from 25mm to 32mm and inside the pocket it decreases. This is happens due to the change of film thickness in this area. The shear stresses are lower in this region, thus the frictional heat is lower. From 38mm to 45mm the temperature increases. A 3D representation of the pressure profile is shown on **Figure 134** and **Figure 135.**

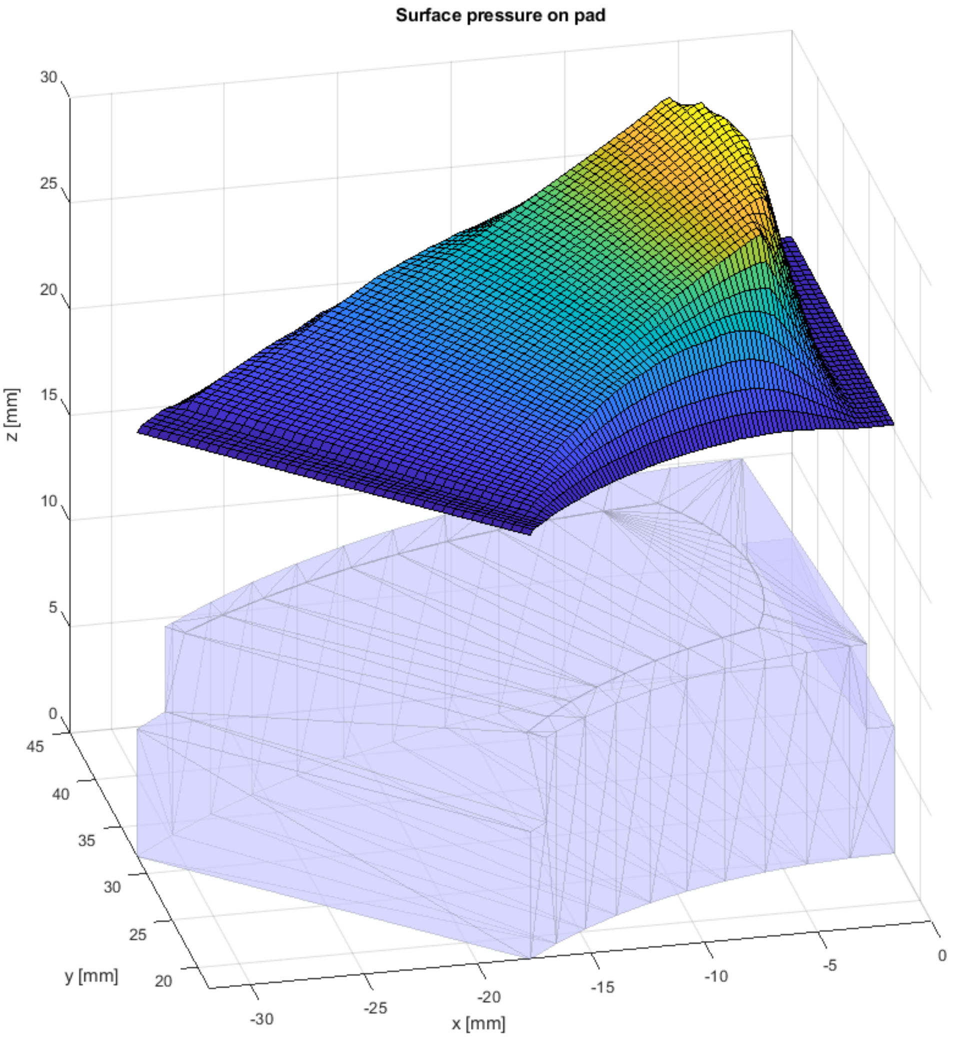

Figure 134 - 3D Pressure profile on pad

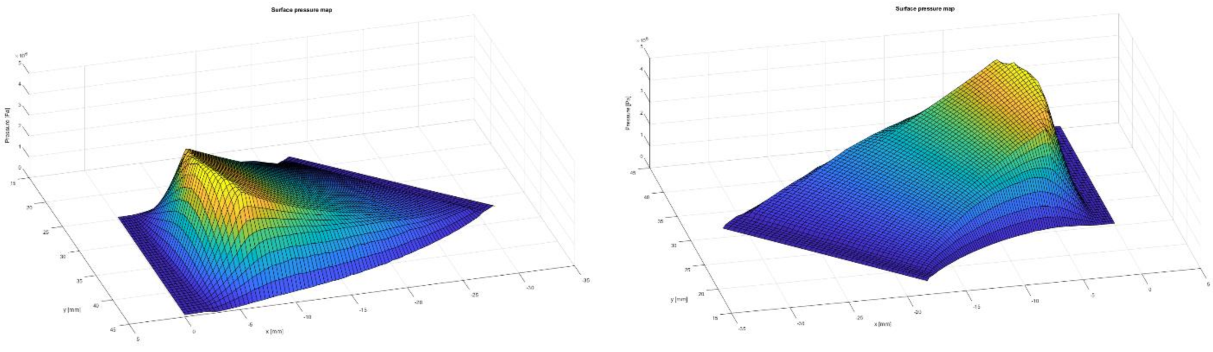

(a)

(b)

Figure 135 - 3D pressure profile a) outer radius, b)inner radius

3 Experimental Set Up

During the carry out of the current thesis an experimental set up was prepared in the laboratory of Marine Engineering of the NTUA, in order to perform certain experiments on thrust bearings, to assess their tribological properties and compare them with computational results. The manufacturing process took place in our workshops. The first stage was the design of the pad and rotor geometries on a CAD software and the generation of a CAM algorithm. Multiple manufacturing methods were utilised, including CNC and conventional milling, conventional turning with lathe, drilling, cutting, polishing and resurfacing. The second stage was the preparation of the equipment. The lab has a comprehensive materials tester for mechanical and tribological properties provided by UMT Bruker. A more thorough description of the lab components will be discussed later.

3.1 Parallel Thrust Bearing

It has already been proposed that a parallel thrust bearing can withstand serious amounts of specific pressures, thus it can be used in certain applications. It is a rather simple, easy and low-cost solution in terms of manufacturing. The dimensions of the designed bearing are the same as in **Table 1**.

3.1.1 CAD and CAM Process

Firstly, the geometry was generated in a CAD program. The model is shown on **Figure 136**.

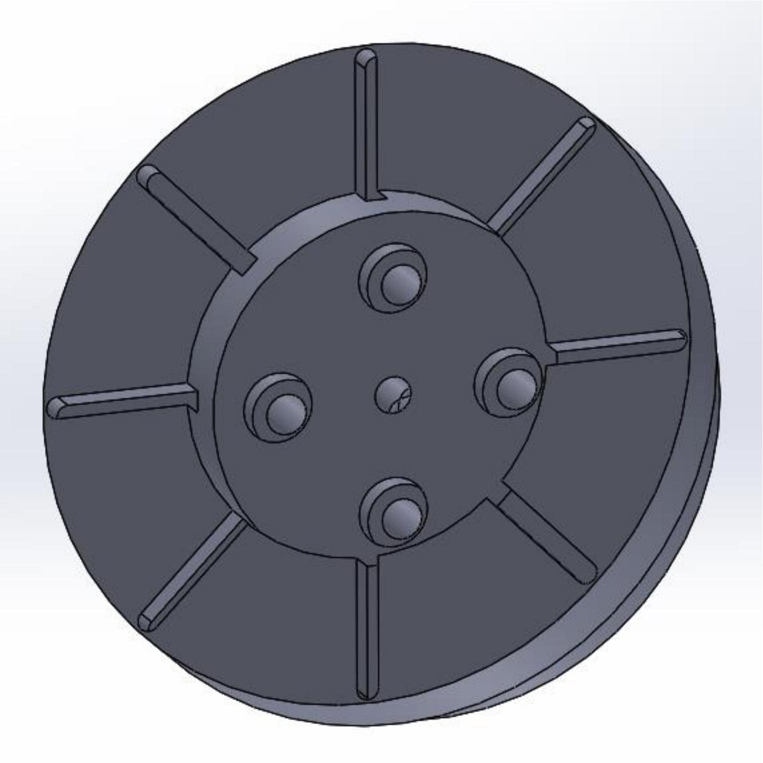

Figure 136 - Parallel Bearing in CAD program

The geometry from the CAD was then imported into a CAM software to generate the G-Code for the CNC milling machine, **Figure 137**.

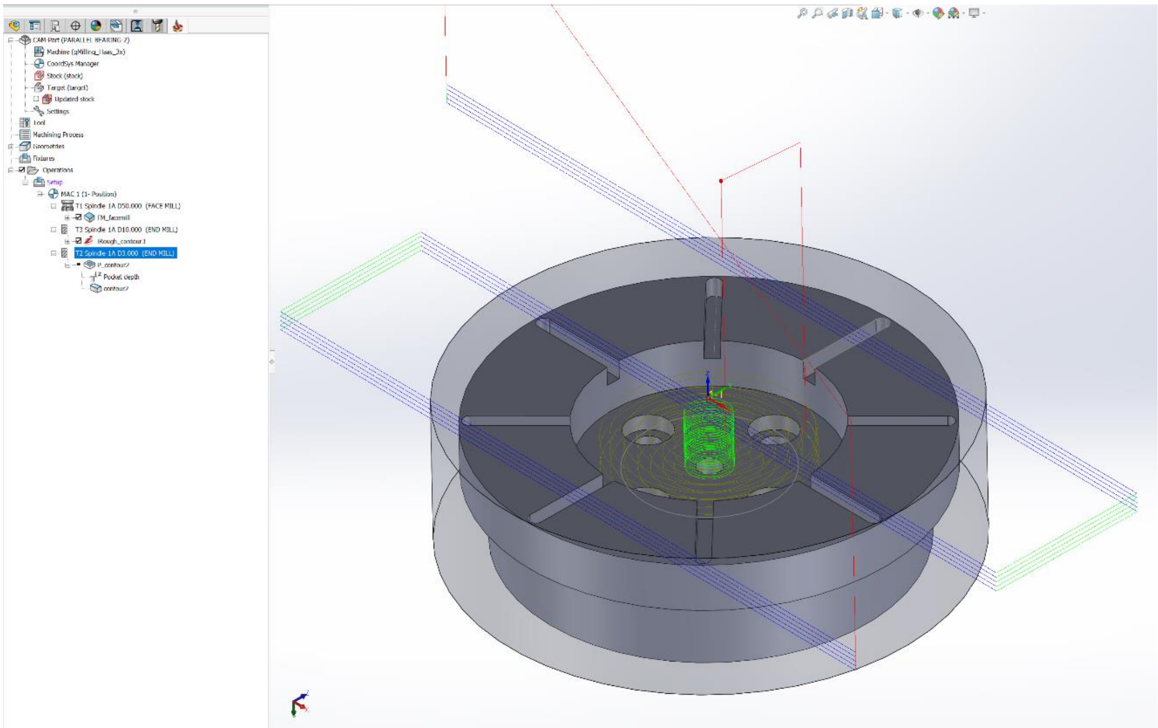

Figure 137 - CAM software for the generation of G-Code

3.1.2 Manufacturing Process

The outer diameter of the pad is 90mm. A steel cylinder with 100mm diameter was selected. With the turning process, using a conventional lathe as seen on **Figure 138**, the diameter was set at 90mm.

Figure 138 - Conventional Lathe

The steel cylinder was then placed in the CNC milling the machine. The CNC used was a HAAS TM2 with 4-axis of freedom, as shown on **Figure 139**.

Figure 139 - CNC HAAS TM2

The cylinder was placed on a choke and zeroed in all 3 axes. The first process was face milling with a 50mm face milling cutter in order to straighten the surface, as presented on **Figure 140.** The result of the face milling is shown on **Figure 141**.

Figure 140 - Face Milling of Part

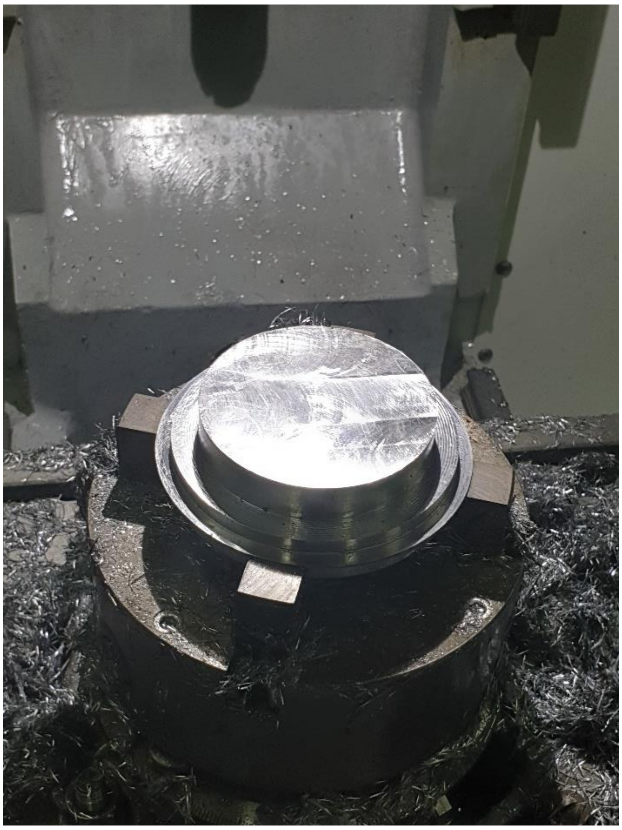

Figure 141 - Result of Face Milling

The center pocket was then cutted using a 10mm End mill Cutter as show on **Figure 142**.

Figure 142 - Center Pocket Cutting

The next part was the manufacturing of the oil inlet grooves using a 3mm End mill as presented on **Figure 143**.

Figure 143 - Oil Grooves Manufacturing

Finally the four holes were drilled and the final outer diameter was cut as seen on **Figure 144.**

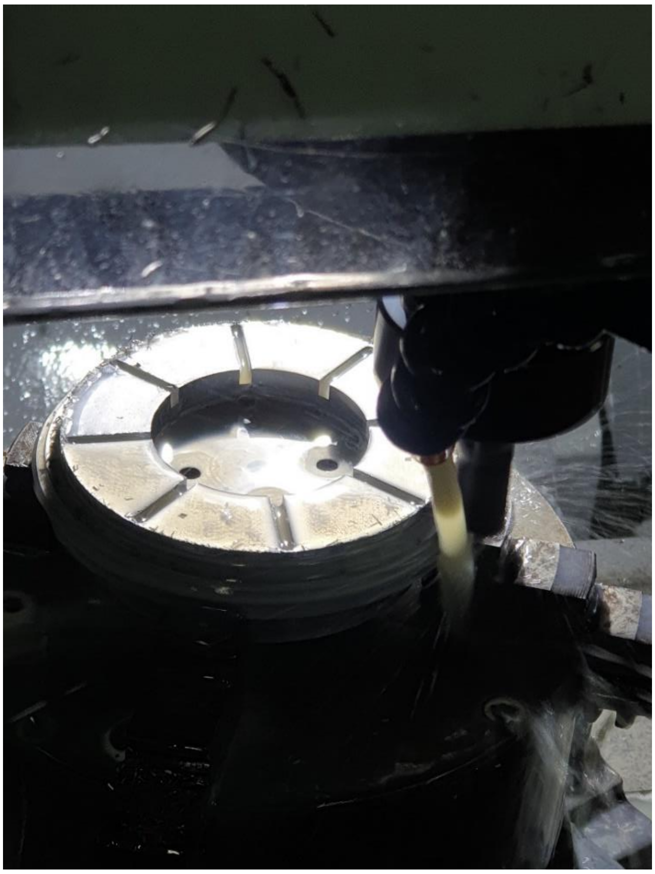

Figure 144 - Drilling and Outer Diameter cutting

The final result is presented on **Figure 145.** The part was then sent for surface finishing in order to achieve the desired roughness and parallelism of the bottom and top surfaces of the bearing.

Figure 145 - Final Result

The same process was followed for the manufacturing of a textured pocket thrust bearing. (**Figure 146**)

Figure 146 - Textured Bearing with Pocket

3.1.3 Optical Profilometer Measurements

A Bruker optical profilometer was used to assess the roughness of the pad and rotor surfaces**, Figure 147**. The results are shown on **Figure 148** and **Figure 149**. The roughness was measured at 209.54 nm and the surface spikes profile were between ±0.5 µm.

Figure 147 - Bruker Optical Profilometer

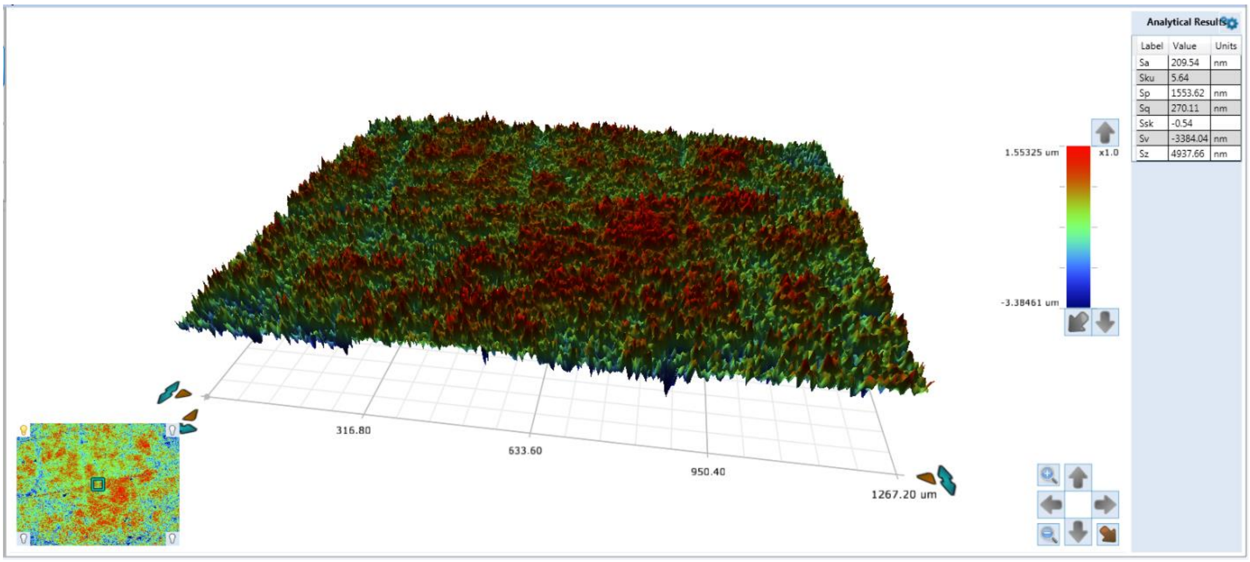

Analytical Results

Label	Value	Units
Sa	209.54	nm
Sku	5.64	
Sp	1553.62	nm
Sq	270.11	nm
Ssk	-0.54	
Sv	-3384.04	nm
Sz	4937.66	nm

Figure 148 - 3D surface on profilometer on Stator

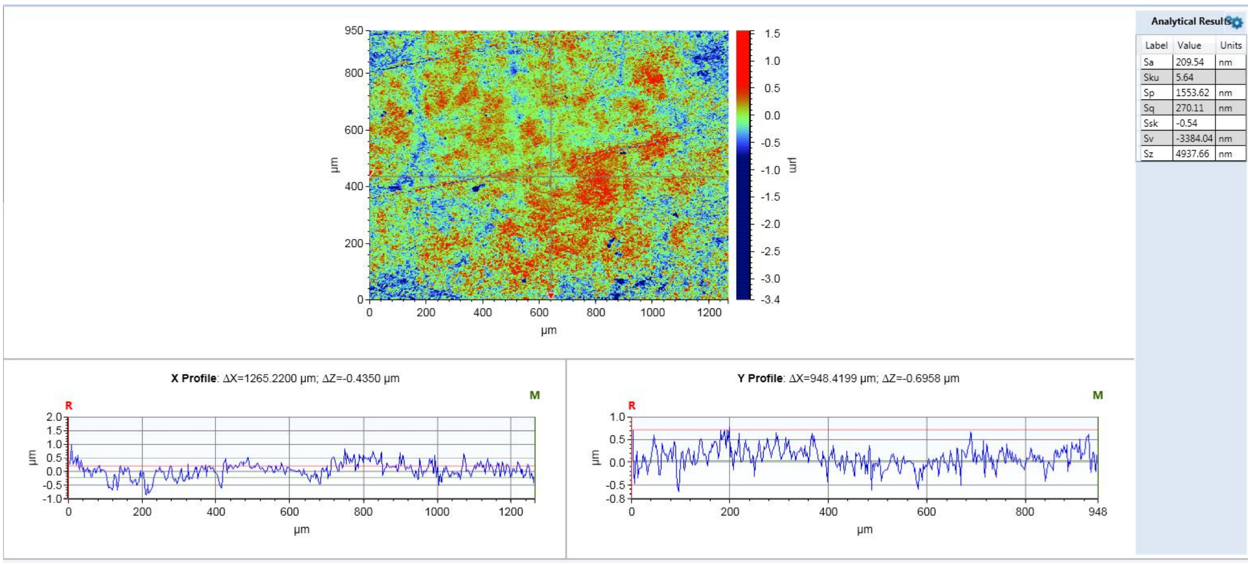

Label	Value	Units
Sa	209.54	nm
Sku	5.64	
Sp	1553.62	nm
Sq	270.11	nm
Ssk	-0.54	
Sv	-3384.04	nm
Sz	4937.66	nm

Figure 149 - X and Y Profile of the surface on Stator

The same measurements were performed for the rotor, as seen on **Figure 150** and **Figure 151**. The roughness was measured at 191.03 nm and the spikes of the surface were between ±0.5 µm.

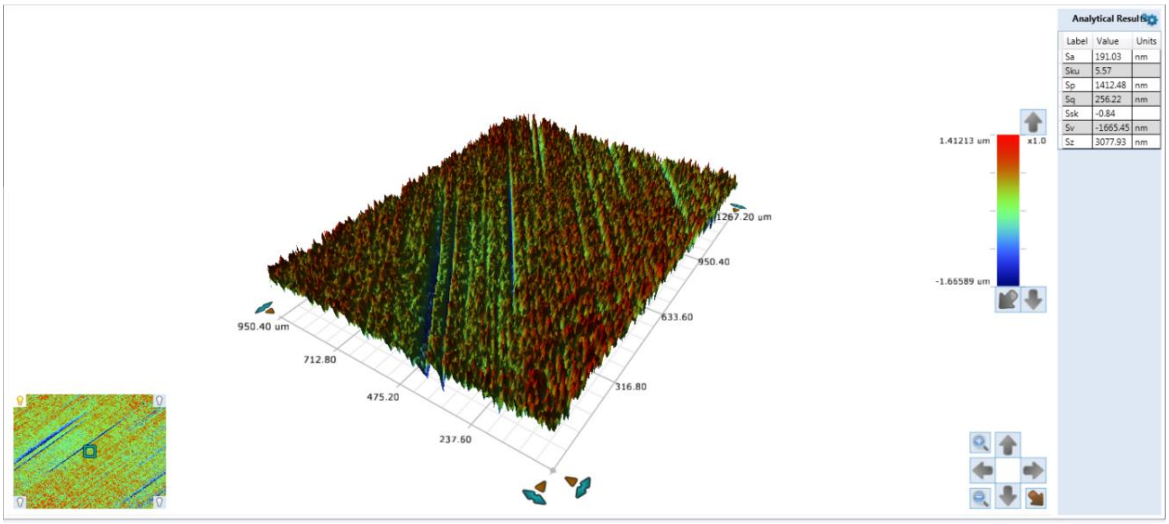

Label	Value	Units
Sa	191.03	nm
Sku	5.57	
Sp	1412.48	nm
Sq	256.22	nm
Ssk	-0.84	
Sv	-1665.45	nm
Sz	3077.93	nm

Figure 150 - 3D surface on profilometer on Rotor

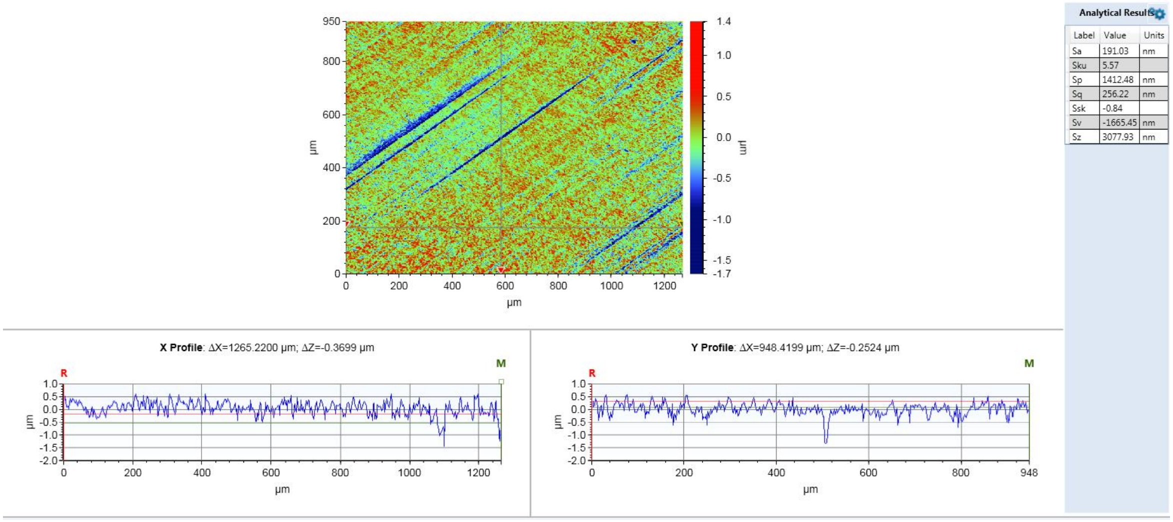

Label	Value	Units
Sa	191.03	nm
Sku	5.57	
Sp	1412.48	nm
Sq	256.22	nm
Ssk	-0.84	
Sv	-1665.45	nm
Sz	3077.93	nm

Figure 151 - X and Y Profile of the surface on Rotor

3.2 Tribometer Set-Up

A UMT Bruker Tribometer was used for the experiments, as seen on **Figure 152**. For the disc on disc experiment, this tribometer is capable of reaching axial loads of up to 1kN and rotational velocities of up to 1000rpm. All the parts must be aligned in order to work properly. Misalignments can cause on the one hand false measurements and on the other hand severe damage on the surfaces. The alignment process is shown on **Figure 153**.

Figure 152 - UMT Bruker Tribometer

Figure 153 - Alignment Process

The stator is then mounted on the torque sensor. The rotor is mounted on the bottom disc. The complete experimental setup is shown on **Figure 154**. The oil is fed from an oil tank, through a pump, in the center of the bearing. The oil from the outlet returns to the oil tank through a second pump. A pressure and temperature gauge are installed on the inlet in order to control the pressure and monitor the inlet temperature.

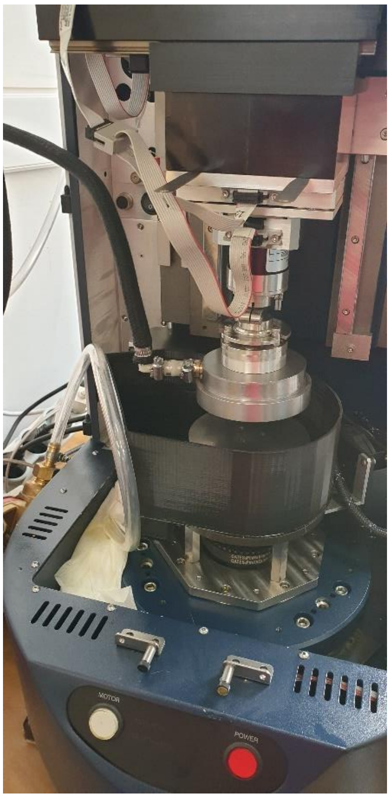

Figure 154 - Experimental Set-Up

Figure 155 - Pressure and Temperature Gauge

The experiment is initiated by the rotation of a stepper motor. Then the load is applied on the vertical axis. The programmed values of rotational velocity and axial load are sent to the tribometer from a software. The friction torque and height are measured in order to generate the final results. On **Figure 156** an undergoing experiment on a parallel bearing is show.

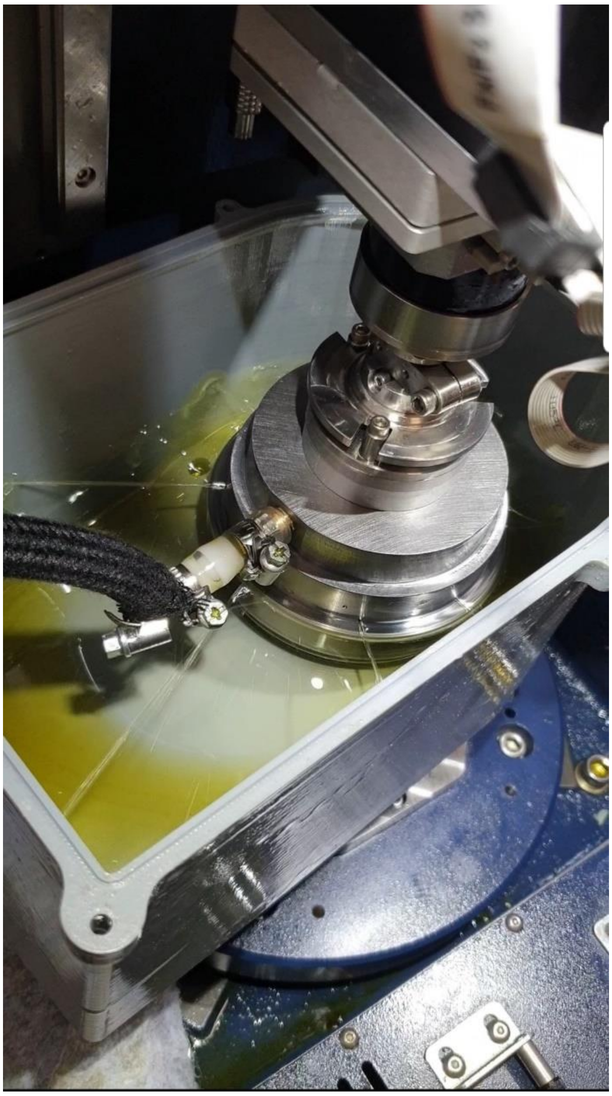

Figure 156 - Experiment on Parallel Bearing

Conclusions and Future Work

In the present work a computational analysis for hydrodynamic lubricated thrust bearings has been performed. In the beginning with a thermohydrodynamic THD modelling approach, an optimisation of the texturing for a parallel thrust bearing has been conducted, for circumferential grooves and rectangular dimples, followed by a sensitivity analysis of the optimisation parameters for the latter, near the optimal values, in order to validate the local optimality. Moreover, several values of rotational velocities and minimum film thicknesses were considered in order to assess the performance of the texturing in different cases. A new modelling approach has been introduced, which takes into consideration the thermal and mechanical deformations of the pad geometry. This new approach (TEHD modelling) utilises the 2-way FSI technique and has been used to re-evaluate the THD optimal thrust bearing configuration. A sensitivity analysis of the textured geometry parameters with the TEHD model has been performed, in order to evaluate the local optimality with the new approach. Finally, a TEHD study was performed for a tapered land and a textured open pocket thrust bearing.

For a parallel textured thrust bearing with rectangular dimples, the optimal geometry strongly depends on the operational parameters. The rotational velocity affects significantly the pressure and temperature distribution. For high rpm values, temperature increases, and cavitation effects become significant. The findings of the TEHD evaluation of the optimal geometry can be concluded to the following:

- The thermal deformation of the pad leads to a substantial alteration of the fluid geometry while generating a converging and a diverging region in the streamwise direction. The converging region extends from the leading edge (inflow) to the end of the textured surface area. This alteration supports the pressure build up on the inlet and hence decreases the cavitation probability within the dimples. Moreover, the converging geometry helps in the increase of the inflow of cold lubricant into the pad, thus lowering considerably the overall temperature in the lubricant domain. The diverging region though extends from the end of the textured surface area to the trailing edge (outflow). This leads to a substantial increase of the pressure drop in the outflow region, and therefore increases the cavitation probability at the outer radius of the trailing edge, which decreases the load carrying capacity of the bearing.
- For a given value of the minimum film thickness the TEHD studies compared to the THD models showed a reduction of the load carrying capacity by 13% and of the friction torque by 4%, and an increase of the coefficient of friction by 10%. These results point out that the deformation plays indeed a vital role on the performance of the bearing.

The tapered land geometry demonstrated higher values of thrust load, followed by lower COF for the same minimum film thickness compared to the textured with rectangular dimples. The pressure distribution is smoother, the temperature field is lower, and cavitation does not occur. The TEHD analysis compared to the THD showed a decrease of the LCC by 6.8% and Friction Torque by 3.5% followed by an increase of the COF by 3.6%. For higher values of rotational velocities, specific loads or temperatures the thermal deformation would increase, leading to the alteration of the fluid pad geometry, thus the deviation from the THD results would be more significant.

The pocket bearing exhibits by far the best performance of all the designs. The load carrying capacity is higher compared to the tapered land and the parallel textured one. The friction torque is lower; thus, the overall COF is decreased. The temperature is slightly higher compared to the tapered land. This can be attributed to the lower minimum film thickness. A direct comparison of the two cannot be done with the current study. More values of minimum film thicknesses should be calculated in order to extract a valid result. However, the fact that the pocket bearing exhibits lower values of friction torque, for higher LCC indicates its superiority.

Based on the present study, a direct optimisation of the texture geometry parameters by a TEHD approach is extremely expensive computationally. The most realistic approach is an optimisation of the parameters with a THD-based analysis and the tuning of the geometry details and the quantification of performance indices by detailed TEHD simulations. These are essential for applications which involve high rotational speeds, high thrust loads and generally high temperatures.

In the quest of a better understanding of the performance of hydrodynamic lubricated thrust bearings, the following topics for further study are presented:

- A more thorough experimental approach of the performance of thrust bearings, utilising the already existing experimental set up. Several experiments should be performed for different values of rotational velocities and loads, followed by corresponding computational models, in order to compare the theoretical and practical results and quantify the performance of the bearings. Moreover, different lubricants and operating conditions should be assessed.
- Alternative geometries of surface texturing, converging or diverging side faces, and tilting pads should be assessed by TEHD analysis.
- A complete model of a thrust bearing with all pads, including the points of support should be evaluated by TEHD analysis in order to quantify the real deformation of the thrust bearing.
- A 2-way FSI technique for both the rotor and stator should be developed, in order to take into consideration, the alteration not only of the fluid-pad interface, but also of the fluid rotor interface.

References

[1] Osborne Reynolds, (1886) , "On the Theory of Lubrication and its Application to Mr. Beauchamp Tower's Experiments, including an Experimental Determination of the Viscosity of Olive Oil", Proceedings of the Royal Society

[2] Fogg, A. (1946), "Fluid Film Lubrication of Parallel Thrust Surfaces", Proceedings of the Institution of Mechanical Engineers

[3] Cameron, A., Wood, W. L. (1958), "Parallel Surface Thrust Bearing", A S L E Transactions

[4] Currie, I. G., Brockley, C. A., & Dvorak, F. A. (1965). Thermal Wedge Lubrication of Parallel Surface Thrust Bearings. Journal of Basic Engineering

[5] Tzeng S. T., & Saibel E., (1967), "Surface Roughness Effect on Slider Bearing Lubrication", A S L E Transactions

[6] Tonder K., (1987), "Effects of skew unidirectional striated roughness on hydrodynamic lubrication", Wear

[7] Lin, Q., & Li, B. (2015). Comparison of the Influences of Surface Texture and Boundary Slip on Tribological Performances. Mathematical Problems in Engineering, 2015,

[8] C. I. Papadopoulos, L. Kaiktsis, M. Fillon, 2013, "Computational Fluid Dynamics Thermohydrodynamic Analysis of Three-Dimensional Sector-Pad Thrust Bearings With Rectangular Dimples", Journal of Tribology, Vol. 136, Issue 1, No 011702

[9] Pascovici M, Cicone T, Fillon M and Dobrica M. Analytical investigation of a partially textured parallel slider. Proceedings of the Institution of Mechanical Engineers, Part J: J. of Engineering Tribology 2009; 223(2): 151-158

[10] C. I. Papadopoulos, E. E. Efstathiou, P. G. Nikolakopoulos, L. Kaiktsis, 2011, "Geometry optimization of Textured Three-Dimensional Micro- Thrust Bearings"

[11] Cupillard S, Cervantes M and Glavatskih S. Pressure buildup mechanism in a textured inlet of a hydrodynamic contact. J. of Tribology 2008; 130(2): 21701: 1-10."

[12] Papadopoulos C, Nikolakopoulos P and Kaiktsis L. Characterization of stiffness and damping in textured sector-pad micro-thrust bearing using computational fluid dynamics. Proceedings of ASME Turbo Expo 2012: Turbine Technical Conference and Exposition, Copenhagen, Denmark, 11-15 June, paper no. GT2012-69403, pp. 1-10.

[13] Marian V, Kilian M and Scholz W. Theoretical and experimental analysis of a partially textured thrust bearing with square dimples. Proc. IMechE, J. Engineering Tribology 2007; Part J; 221: 771-778.

[14] Fouflias, D. G., Charitopoulos, A. G., Papadopoulos, C. I., Kaiktsis, L., & Fillon, M. (2014). Performance comparison between textured, pocket, and tapered-land sector-pad thrust bearings using computational fluid dynamics thermohydrodynamic analysis. Proceedings of the Institution of Mechanical Engineers, Part J: Journal of Engineering Tribology

[15] Zouzoulas, V., & Papadopoulos, C. I. (2017). 3-D thermohydrodynamic analysis of textured, grooved, pocketed and hydrophobic pivoted-pad thrust bearings. Tribology International

[16] A. Charitopoulos, D. Fouflias, C.I. Papadopoulos, L. Kaiktsis and M. Fillon,2014, "Thermohydrodynamic analysis of a textured sector-pad thrust bearing: effects on mechanical deformations"

[17] Dadouche A, Fillon M and Dmochowski W. Performance of a hydrodynamic fixed geometry thrust bearing: comparison between experimental data and numerical results. Tribology Transactions 2006; 49: 419-426.

[18] Ahmed S, Fillon M & Maspeyrot P. Influence of pad and runner mechanical deformations on the performance of a hydrodynamic fixed geometry thrust bearing. Proceedings of IMechE (2009), Vol. 224 Part J. Engineering Tribology, pp. 305-315.

[19] Brockett S, Barrett L & Allaire E. Thermoelastohydrodynamic analysis of fixed geometry thrust bearings including runner deformation. Tribology Transactions (1996), Vol. 39, pp. 555-562.

[20] Rahmani R., Shirvan A., Shirvani H., 2007, 'Optimization of partially textured parallel thrust bearings with square-shaped micro-dimples', Tribology Transactions, Vol 50(3), pp. 401-406.

[21] Fu G., Untaroiu A., 2016, 'An Optimum Design Approach for Textured Thrust Bearing With Elliptical-Shape Dimples Using CFD and DOE Including Cavitation', ASME 2016 International Mechanical Engineering Congress and Exposition, Vol. 7.

[22] Brizmer V., Kligerman Y., Etsion I., 2003, "A Laser Surface Textured Parallel Thrust Bearing", Tribology Transactions, Vol. 46(3), pp. 397-403.
[23] Gropper D., Wang L., Harvey T., 2016, "Hydrodynamic lubrication of textured surfaces: A review of modeling techniques and key findings", Tribology International, Vol. 94, pp. 509-529.
[24] Henry Y., Bouyer J., Fillon M., 2014, "An experimental analysis of the hydrodynamic contribution of textured thrust bearings during steady-state operation: A comparison with the untextured parallel surface configuration", Journal of Engineering Tribology, Vol 229, pp 362-375.
[25] E. J. Hahn and C. F. Kettleborough, 1968, "The Effects of Thermal Expansion in Infinitely Wide Slider Bearings—Free Thermal Expansion", J. of Lubrication Tech., Vol. 90, Issue 1, pp. 233-239.
[26] Cahon, S., Melab, N., and Talbi, E. G., 2004, "ParadisEO: A Framework for the Reusable Design of Parallel and Distributed Metaheuristics," J. Heuristics, 10(3), pp. 357–380.
[27] Deb, K., Pratap, A., Agrawal, S., and Meyarivan, T., 2002, "A Fast and Elitist Multiobjective Genetic Algorithm: NSGA-II," IEEE Trans. Evol. Comput., 6(2), pp. 182–197.
[28] Stachowiak, G. W., and Batchelor, A. W., 2014, Engineering Tribology, 4th ed. Butterworth and Heinemann, Burlington, MA, Chap. 4.
[29] https://www.mathworks.com/discovery/genetic-algorithm.html

NOMENCLATURE

H_{min}:	Minimum film thickness (μm)
V:	velocity vector (m/s)
p:	the static pressure (Pa)
T:	the temperature (K)
τ:	the viscous stress tensor
ρ:	the oil density (kg/m^3)
μ:	the oil dynamic viscosity (kg/(m*s))
c_p:	oil specific heat capacity (J/(kg*K))
λ_f:	oil thermal conductivity (W/(m*K))
λ_{sp}:	pad thermal conductivity (W/(m*K))
λ_{sr}:	rotor thermal conductivity (W/(m*K))
[D]:	elasticity matrix
$\{\varepsilon^{el}\}$:	elastic strain vector
$\{\varepsilon\}$:	total strain vector
$\{\varepsilon^{th}\}$:	thermal strain vector
α^{se}:	secant coefficient of thermal expansion